HARMONIA
International network for harmonization of atmospheric aerosol retrievals from ground based photometers

HARMONIA CA21119

Deliverable 1.2

Differences and harmonisation possibilities in AOD retrieval methods

WG1 leaders	Lionel Doppler[1], Akriti Masoom[2]
Contributors	(By alphabetical order) Africa Barreto Velasco[3], Victor Estellés[4], Ilias Fountoulaskis[5], Claudia Frangipani[6], Pablo González Sicilia[3], Sandra Graßl[7], Peter Hrabčák[8], Liviu Ivanescu[9], Angelos Karanikolas[2], Stelios Kazadzis[2], Dimitra Kouklaki[10,11], Natalia Kouremeti[2], Gaurav Kumar[4], Alexander Mangold[12], Roberto Román Diez[13], Paolo Russo Ganón[14], Volodya Savastiouk[15], Ralf Zuber[16]
Date	14 November 2024

[1] Meteorologisches Observatorium Lindenberg - Richard-Aßmann-Observatorium, Deutscher Wetterdienst (MOL-RAO, DWD), Lindenberg (Tauche), Germany

cost EUROPEAN COOPERATION IN SCIENCE & TECHNOLOGY

Funded by the European Union

[2] Physikalisch-Meteorologisches Observatorium Davos / World Radiation Center (PMOD/WRC), Davos, Switzerland
[3] Izaña Atmospheric Research Center, Meteorological State Agency of Spain (IARC, AEMet), Teneriffe, Spain
[4] Facultat de Física, Universitat de València (UV), Burjassot (Valencia), Spain
[5] Research Centre for Atmospheric Physics and Climatology of the Academy of Athens (RCAPC, AA), Athens, Greece
[6] Istituto di Scienze Polari, Consiglio nazionale delle ricerche (ISP, CNR), Bologna, Italy
[7] Alfred-Wegener-Institut, Helmholtz-Zentrum für Polar- und Meeresforschung (Alfred-Wegener-Institut – AWI), Potsdam, Germany
[8] Slovenský hydrometeorologický ústav, Aerologického a radiačného centra (SHMÚ, ARC), Poprad-Gánovce, Slovak Republic
[9] Centre d'applications et de recherches en télédétection (CARTEL), Université de Sherbrooke, Sherbrooke, Canada
[10] Department of Geology and Geoenvironment, National and Kapodistrian University of Athens (DGG, NKUA), Athens, Greece
[11] Institute for Astronomy, Astrophysics, Space Applications and Remote Sensing, National Observatory of Athens (IAASARS,NOA), Athens, Greece
[12] Koninklijk Meteorologisch Instituut van België - Institut Royal de Météorologie (KMI-IRM), Brussels, Belgium.
[13] Grupo de Óptica Atmosférica, Universidad de Valladolid (GOA, UVa), Spain.
[14] Laboratorio de Energía Solar (LES), Universidad de la República, Salto, Uruguay
[15] International Ozone Services Inc., Toronto, Canada
[16] Gigahertz Optik GmbH (GHO), Türkenfeld bei München, Germany

Table of Contents

1. Introduction

Climate change is globally affecting many weather and climate extremes leading to adverse impacts on the atmosphere, ocean, cryosphere and biosphere (IPCC 2023). According to the recent report by IPCC (2023), with prolonged and increasing human activities (such as unsustainable use of energy and land, land-use change, lifestyles, consumption and production across regions) especially associated with greenhouse gas emissions have led to global warming with global surface temperature approaching 1.1°C increase in 2011-2020 from 1850-1900.

Another example of source of climate extremes are increasing wildfire activity that leads to increase in atmospheric CO_2, trace gases, etc. such as the recent Canadian wildfire events of 2023 that caused elevated aerosol loading much higher than the regional climatological averages and has been recorded as one of the extreme year of heatwaves and wildfires since at least 1980 (Byrne et. al., 2024; MacCarthy et. al., 2024) impacting many regions of the Northern Hemisphere (Wang et. al., 2024) as well as causing both environmental and socio-economic havocs (Jain et. al., 2024).

Atmosphere aerosols play a vital role in the Earth's radiation budget and hydrological cycle having both direct effect such as aerosol-radiation interactions i.e., absorption and scattering of incoming solar radiation as well as indirect effect such as acting as cloud condensation nuclei and participating in formation and modification of cloud properties. Aerosol optical, microphysical and radiative properties play a major role in understanding atmospheric phenomena (such as extreme weather events, atmospheric warming/cooling effects, aerosol/cloud feedbacks), climate and weather modeling, solar energy related studies, as well as other sectors such as human health.

The high aerosol loading in the atmosphere associated with both environmental extremes and anthropogenic activities are measured by a key parameter such as Aerosol Optical Depth (AOD) which is a columnar product of sun photometers direct sun measurements. Sun photometers are passive remote sensing instruments used for measuring AOD using the Beer-Bouguer-Lambert law by taking into account the contribution from Rayleigh scattering by atmospheric molecules and absorption by atmospheric constituents other than aerosols such as ozone, nitrogen dioxide, and

water vapour. Another important parameter is the Ångström Exponent (AE) characterizing the spectral variation of AOD on a given spectral interval. AE is the negative slope of the logarithmic regression of AOD as a function of wavelength following Ångström power law (Ångström 1970).

There are varied instrumentations and networks for AOD measurement and other aerosol properties retrievals including global networks like AERONET (using Cimel sun photometer), SKYNET (using Prede POM), GAW-PFR (using Precision Filter Radiometer: PFR) as well as standalone instruments such as Microtops, Calitoo, etc. The objective of COST-Action HARMONIA Working Group 1 is the homogenization of established techniques and existing tools, and this deliverable is aimed at reporting on the differences and uncertainties related to standard products provided from already existing analysis algorithms. Hence, with this objective, section 2 describes the cloud screening methodologies used by different AOD measurement techniques followed by section 3 dealing with comparison between instrumentations and finally section 4 presenting high spectral resolved AOD by different types of instruments.

Note: From this point, everywhere in the document, the acronym "AOD" and "AE" will be used to mention the Aerosol Optical Depth and Ångström Exponent, respectively.

2. Cloud screening methods applied to AOD measurement with photometers

Sun photometers AOD retrievals from direct solar irradiance observations are performed when the sun disk is not obscured by clouds due to which identification of cloud-contaminated pixels becomes crucial for maintaining high-quality AOD retrieval. Cloud flagging algorithms play an instrumental role in this process, as failure to accurately determine cloudy pixels can significantly impact AOD retrieval as well as related applications such as air quality monitoring, atmospheric transport models, numerical weather prediction, and data synergism (Masoom et al., 2024a). Therefore, in this section we discuss the cloud flagging algorithms followed by different photometric networks and instrumentations as well as associated unconventional (new) approaches and synergism of instrumentations.

2.1 Cloud screening/flagging methods used in photometer networks (solar)

2.1.1 AERONET cloud screening method

Contributor: Roberto Román Diez

The AERONET Version 3 processing algorithm is described in detail in Giles et al. (2019). Regarding cloud-screening, it is formed by different sequential steps which are well summarized by González et al. (2020), who implemented the same cloud-screening method in the CAELIS software tool (Fuertes et al., 2018). First, a photometer signals higher than 100 counts in the infrared channels (870 and 1020 nm) must be achieved to guarantee the correct pointing to the Sun. If any raw signal is lower than the extraterrestrial signal (calibration factor) divided by 1500, which means an extreme total optical depth, the corresponding channel is rejected. Moreover, if the variability of the triplet signal (calculated as the root mean square over the mean) is larger than 16% in any channel, then the full observation is rejected.

The cloud-free observations are considered as cloudy if the triplet variability (maximum – minimum AOD) is larger than 0.01 (or 0.015×AOD, whichever is greater) for 675, 870 and 1020 nm channels simultaneously. The AOD is removed if the optical air mass is larger than 7 or if AE is without -1 to 3. If the temporal variation of AOD at 500 nm is bigger than 0.01 per minute, the highest measurement is considered cloud contaminated and removed. A novel criterion, based on aureole sky radiance measurements, is applied after, which checks the curvature of the aureole radiance regarding the scattering angle to detect the presence of high ice clouds like cirrus. In addition, the “stand-alone” criterion removes any observation if it is distant by more than 1 h from any other cloud-free measurement.

In the case that the standard deviation of AOD at 500 nm of the cloud-free remaining points in the day is larger than 0.015, then the observations that exceed ±3 times the standard deviation in AOD or AE are assumed to be cloud contaminated. If AOD at 870 nm is larger than 0.5 and AE (675–1020 nm) is larger than 1.2, then the measurement is assumed as cloud-free even if other criteria classified it as cloudy. Finally, every time that one full day of observations has less than 3 cloud-free

observations (or 10% of the total of observations), then any data of the day is considered as cloud-contaminated. AERONET also applies other criteria for quality controls, differing from cloud-screening but also mandatory to obtain the category of level 1.5 data. These criteria are focused on detecting time shifts, cleaning issues or malfunctions in instruments, among others.

2.1.2 SKYNET cloud screening method

Contributor/Source: Victor Estellés, Nakajima et al., 2020

The method used for the cloud screening of direct sun data consists in the adaptation of the Smirnov et al. (2000) method to Prede measurements. The main criteria used in the method is the triplet criteria as in the case of AERONET, consisting on evaluating the short term variability within 1-2 minutes, but it cannot be applied directly, as Prede does not measure in triplets (three consecutive measurements separated 20-30 seconds) but measures once per minute; therefore, adapted triplets are created during the formatting of data using the minute measurements. In order to remove data affected by high homogeneous cloud data, extra filters were added, consisting of the inspection of the data continuity, and identification of standalone data points. However, these criteria showed to be very restrictive on occasions (Kazadzis et al., 2018b).

The standard measurement protocols of SKYNET follow 1 min direct solar irradiance measurement and almucantar scan diffuse sky radiance measurement at scattering angles below 780 and forward almucantar scan below 300. In contrast to AERONET's two-side sun scans for a symmetry check and spatial averaging of sky radiances to minimize the inhomogeneous effects, SKYNET only makes one-side almucantar scan of the sun to save on observation time (however, two-sided almucantar scans are made at some sites and separate retrievals are made for each side to evaluate inhomogeneous aerosol distribution in space and time. After determining the radiometric constants, the direct solar irradiance F and relative sky radiance R are used for the level 2 analysis, i.e., retrievals of the geophysical parameters of aerosol, cloud, water vapor, and ozone (Nakajima et al., 2020).

Cloud screening is performed differently by different sub-network groups. For example, European SKYNET Radiometers network performs a cloud screening for a direct solar measurement at 1 min frequency using a procedure based on the

methodology developed by Smirnov et al. (2000), Estellés et al. (2012) and Song et al. (2014). SR-Center for Environmental Remote Sensing (SR-CEReS) of Chiba University conducts the cloud screening with the method of Khatri and Takamura (2009) but without using global irradiance data from a pyranometer (Irie et al., 2019). It corresponds to the combination of a spectral variability test (Kaufman et al., 2006) and statistical analysis test of Smirnov et al. (2000) including checking the number of data, the diurnal stability check, smoothness criteria, and three standard deviation criteria but without a triplet stability criteria test.

2.1.3 GAW-PFR cloud screening method

Contributor/Source: Natalia Kouremeti, Stelios Kazadzis (Kazadzis et al., 2018a)

The cloud detection algorithm used by Global Atmospheric Watch - Precision filter radiometers (GAW-PFR) employ different criteria (Wehrli, 2008) for flagging clouds by PFR such as:

- instrument signal derivative with respect to air mass is always negative (Harrison and Michalsky, 1994). For cases of air masses < 2 where a cloud influence on the noon side of a perturbation cannot be easily detected, a comparison of the derivative with the estimate of the clear Rayleigh atmosphere is performed and data are flagged as cloudy if the rate of change is twice as much (objective method)
- test for optically “thick” clouds with AOD > 2 is performed
- Smirnov et al. (2000) triplet measurement is used by calculating AOD and looking at signal variability for three consecutive minutes (triplet method).
- The variability of the irradiance

An example of the use of the above mentioned three criteria can be seen in Fig. 2.1, where a day with variable cloudiness at Davos is presented. For this particular day, all three criteria are applied. In the early morning and evening, the thick-cloud criteria are applied. Then both the triplet and the objective method are applied due to variable cloudiness in front of the Sun. However, there are times during the day when only the objective method is applied (thin clouds in front of the Sun as seen in the first picture that is superimposed in Fig. 2.1a). During the last part of the day

(second picture), clouds completely disappear, and cloud flagging is set to zero, which means that all three criteria are passed. It has to be noted that cloud flagging is always kept as a constant number describing which one of the three criteria or combination of criteria is valid at a certain minute.

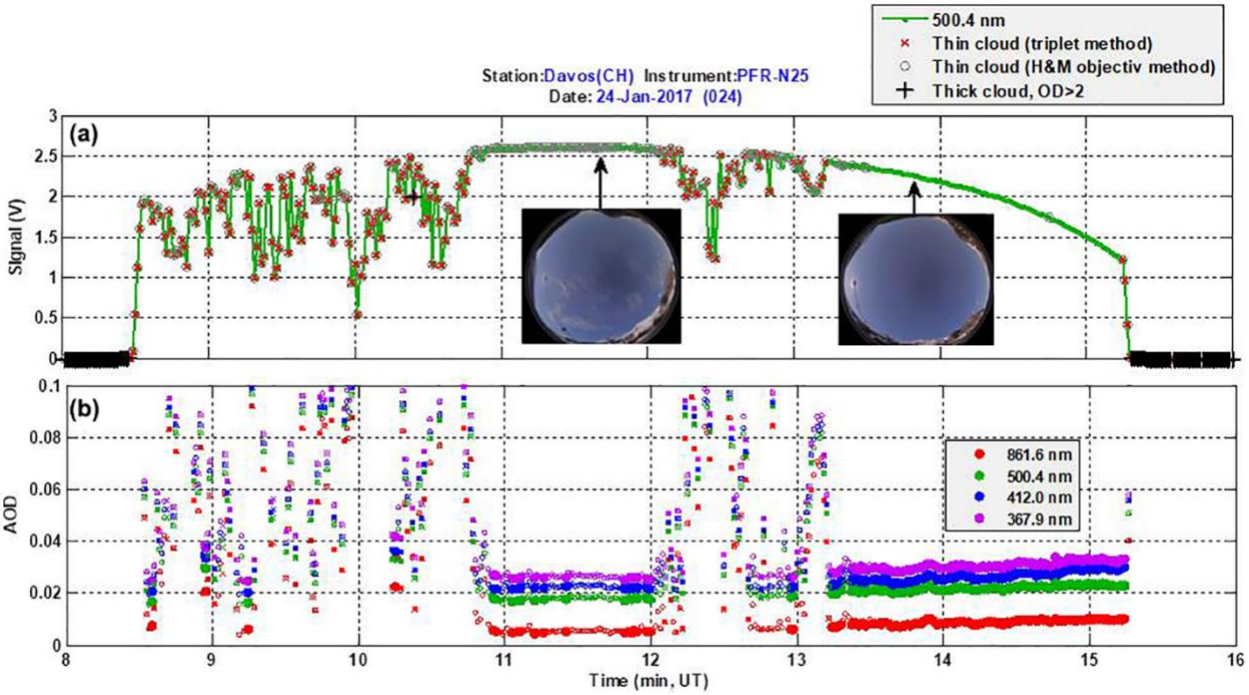

Figure 2.1: Example of a day with variable cloudiness, (a) instrument signal at 500 nm and minute-by-minute application of the three cloud-flagging methods. The two inset pictures show a 360^0 view of the sky using a cloud camera. (b) Calculation of AOD at four wavelengths. (Figure credit: Kazadzis et al., 2018a).

Figure 2.1b shows the calculation of AOD for the whole day, with obvious deviations due to cloud occurrence for the parts of the day when both criteria are fulfilled. It is interesting to see the 10:50 to 12:00 period which is a difficult period when defining the presence of clouds only with direct Sun measurements. For this particular period, even if the AOD is low, the objective method shows the presence of thin clouds in front of the Sun. It has to be noted that final AOD data include all available measurements that have passed the quality control procedures, except the cloud-flagging ones. So, all reported AODs are available, accompanied by a flag showing which cloud-flagging criteria have been assigned to the particular 1 min measurement. An upgraded method using in addition the variability of the AE has been developed and is applied since 2020. When available, sky-camera photos are used in addition.

2.2 Machine learning based cloud screening method (solar)

Sources: Schenzinger and Kreuter (2021) and Schenzinger et al., 2023

Schenzinger and Kreuter (2021) proposed a new cloud screening method for sun photometry that was designed to effectively filter thin clouds. This method was based on a k-nearest-neighbor algorithm using 10 years of data from a PFR in Innsbruck which was compared to the then employed screening technique whose results are presented in Fig. 2.2. Both algorithms agreed well on the classification of a data point as clear or cloudy in a majority of the cases, while the new routine was found to be more effective in flagging thin clouds. Hence, this method can serve as a valid alternative for automated cloud detection.

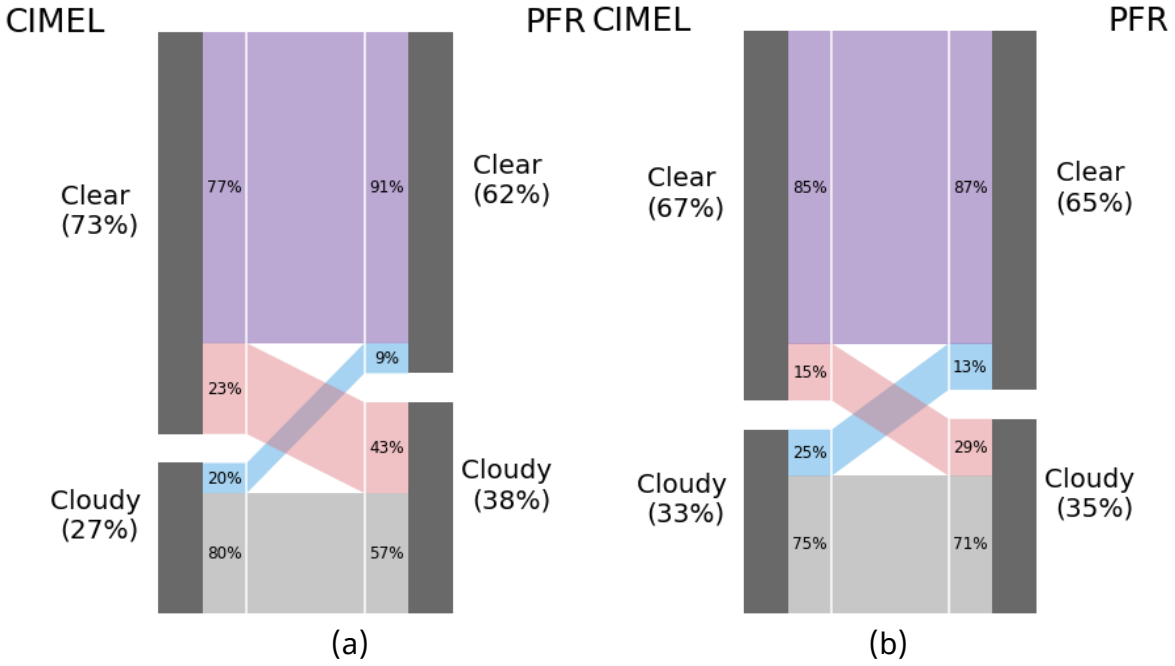

Figure 2.2: (a, b) Comparison of the amount of data points which get flagged by the original and clustering algorithm (dark grey bars). The height of the bars is proportional to the number of points in the category. The grey area signifies where both algorithms agree on the point being cloudy, and the purple where both agree on the points being clear. Red and blue show differences in flagging, with the percentages referring to the partition of the cloudy/clear points of the respective algorithm. (Figure credit: Schenzinger and Kreuter (2021))

Due to the nature of the Clustering routine, it needs at least k measurements to serve as possible nearest neighbors. In Schenzinger and Kreuter (2021) method,

k=20 was chosen, in case of less data points availability, dynamic adaptations were made. However, it is ideal for post-processing to have a higher number of data points as the accuracy of the algorithm increases with a higher number of data points. Nonetheless, dynamic adaptations can be useful for real-time analysis as well, given that erroneously cloudy points can be corrected to clear when more data become available but not the other way round (i.e., points identified as clear once will be labeled as clear regardless of additional measurements). This method was initially tested for Innsbruck where it performed well in different cloud and aerosol conditions (refer to Fig. 4 in Schenzinger and Kreuter 2021) and was able to alleviate AOD bias in the presence of thin clouds.

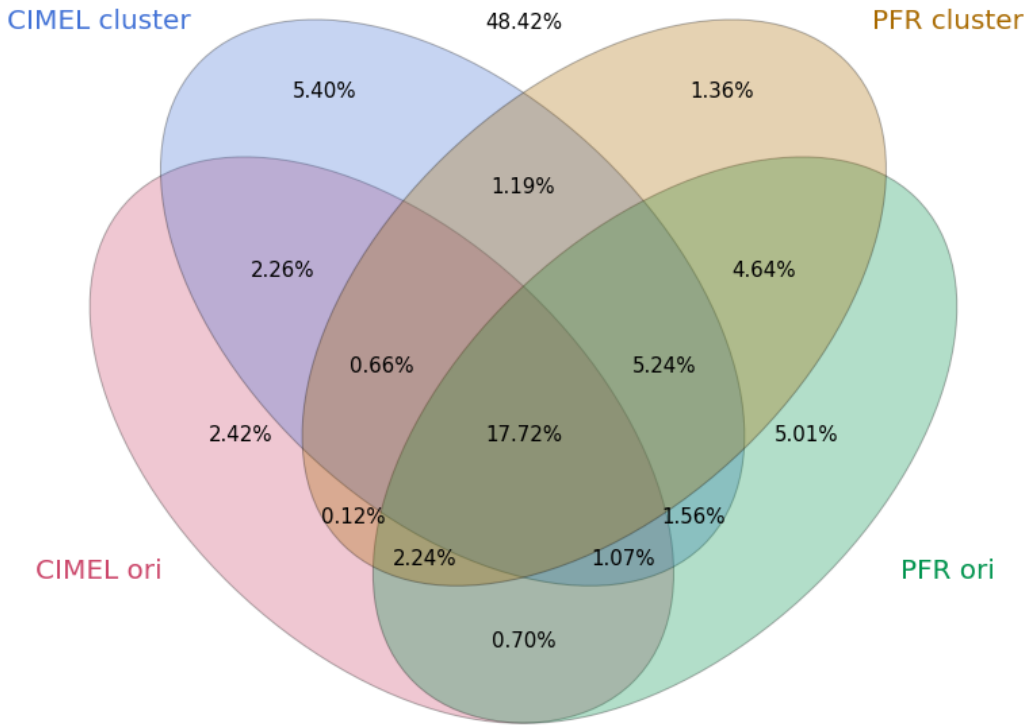

Figure 2.3: Percentage of points which get flagged by the original algorithm and the clustering algorithm for the Cimel and the PFR instruments. The proportion of cloud free points, which both algorithms and instruments agree on, is indicated on top outside the ellipses. (Figure credit: Schenzinger et al., 2023)

A detailed comparison with the already existing cloud screening algorithm of sun photometers (Smirnov et al. 2000, Kazadzis et al., 2018a) showed that both methods agree in their classification for the vast majority of cases as also presented in Fig. 2.3 (refer to Fig. 5 in Schenzinger and Kreuter 2021). Still, Clustering reduces mean AOD for most of the days in our testing period (refer to Fig. 6 in Schenzinger and Kreuter

2021). The daily mean AOD at 501 nm averaged over the last 10 years was lowered by 0.0029, which is comparable to instrument precision (Wuttke et al., 2012). However, on single days Clustering reduces daily mean by more than 0.02 (up to 0.08), which is the same magnitude as reported as bias of the Multiplet routine by Chew et al. (2011) and exceeds the error of the instrument and trace gas optical depth. Together with specific example days (refer to Fig. 4 and Fig. A1 in Schenzinger and Kreuter 2021), this supported the notion that Clustering corrects some cloudy points of the Multiplet routine to clear while flagging some of its erroneously clear points as cloudy. The small difference in the long-term mean is partly due to the specific cloud conditions in Innsbruck and could therefore be much larger in regions with higher prevalence of thin clouds.

Schenzinger and Kreuter (2021) suggested an alternative algorithm to identify clouds in high frequency (1 minute) PFR measurements based on a nearest-neighbor clustering method. This approach takes into account the AOD at 500 nm, its temporal variation, as well as the AE exponents α and γ (similar to δα used in Gobbi et al. (2007)). As their algorithm seemed promising for cloud flagging PFR data in general, this short-term scientific mission expanded their analysis to the stations in Davos and Izaña which have different aerosol conditions than Innsbruck, where it was originally tested.

Schenzinger et al., 2023 showed that overall, the clustering cloud screening algorithm performed well, in different environments (Davos and Izaña) than originally tested in Innsbruck in Schenzinger and Kreuter (2021). While Davos arguably still has similar aerosol conditions to Innsbruck, albeit with lower AOD overall, Izaña with frequent dust events was challenging. In the overall distribution of AOD values, little difference between the original and the new algorithm can be identified, which is positive given that the PFR data does get automatically and manually checked, whereas clustering is a purely automated algorithm. In low AOD conditions, thin clouds do not reliably get identified, giving hints towards potential improvements (refer to Fig. 10 of Schenzinger et al., 2023). The clustering algorithm was found to flag more points than the original algorithm, which is unproblematic for PFR instruments as their high measurement frequency means that false positives (i.e., clear sky that gets mistaken as cloudy) do not influence the data quality as negatively as false negatives (unflagged clouds) would. However, for less

frequent measurements (such as that of CIMEL instruments as shown in Fig. 3 of Schenzinger et al., 2023), especially at high altitude sites with low solar elevation, a more careful assessment as well as adaptation might be necessary.

2.3 Synergism of camera and broadband measurements for cloud flagging (solar)

Contributor: Claudia Frangipani

In this section, the comparison of cloud flags from camera and broadband radiation measurements algorithms with those of different sun-photometers is presented. This analysis was focused on data from July 2023 and, then the analysis was extended to March 2022 collected at the Meteorological Observatory Lindenberg (DWD) from Lindenberg (Tauche, Germany; 52.2° N, 14.1° E, 120 m asl) where measurements and products from different instruments are simultaneously available. Broadband radiation data, both shortwave (global, diffuse and direct normal components – respectively SWD, DIF and DNI) and downward longwave, are collected within the Baseline Surface Radiation Network framework.

Spectral sun irradiance for AOD retrieval is measured by different instruments: Cimel, whose data are processed by both AERONET and CAELIS (GOA, University of Valladolid) algorithms, and PFR. The algorithm versions for AERONET and PFR products are version 3 and version 2.25, respectively. The OMEA-3C all-sky camera data are yielded by three different algorithms developed by GOA (University of Valladolid): one that predicts cloud fraction (CF), one that determines whether the sun is clear (unobstructed) or not, one that computes CF from the image taken; only the last two were used in this study.

Cloud flags from broadband radiation data were obtained using RADFLUX (Riihimaki et al. 2019) and BrightSun (Bright et al. 2020) codes. RADFLUX is able to process both SWD and DIF components for a more accurate cloud detection/identification of clear-sky conditions (CS), it computes clear sky shortwave component estimates and yields cloud fraction (CF). BrightSun comprises different models that are able to flag measurements as clear-sky or clear-sun, but only the latter is relevant for the comparison. Cloud flags from the following models were considered: BrightSunCSDs, Gueymard, Larraneta, RuizArias, and Zhao. They process different

shortwave components, but all require the respective CS estimate that was obtained from RADFLUX.

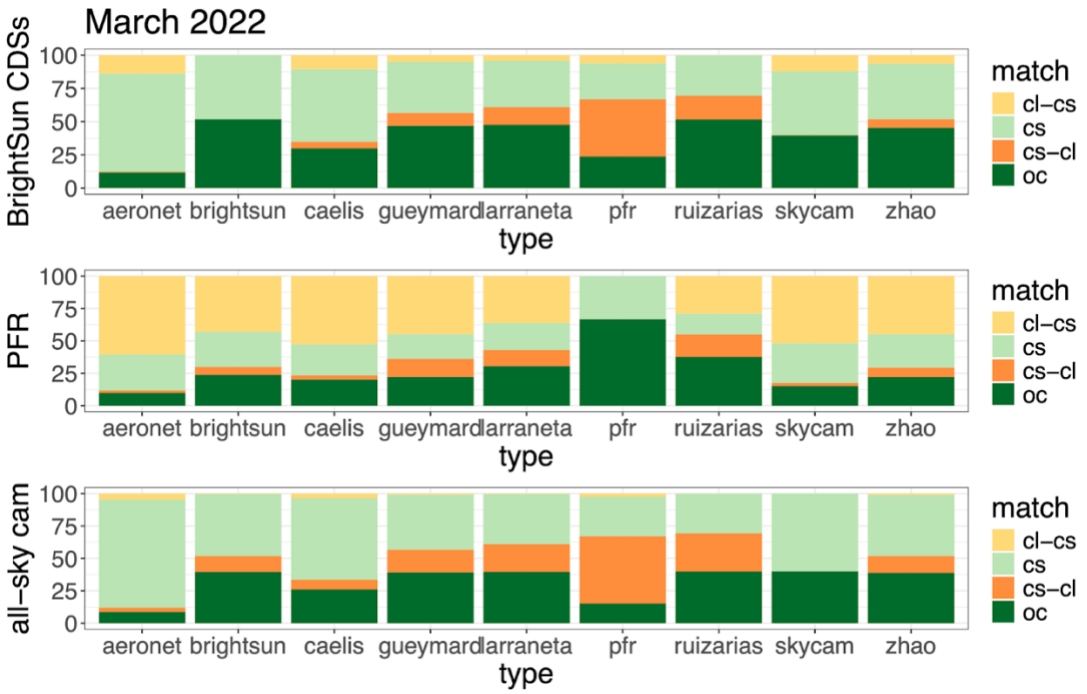

Figure 2.4: Match and mismatch of cloud flags for March 2022. cs stands for clear-sky, cl stands for cloudy, cl-cs stands for cloudy (y axis) – clear (x axis), cs -cl for the opposite.

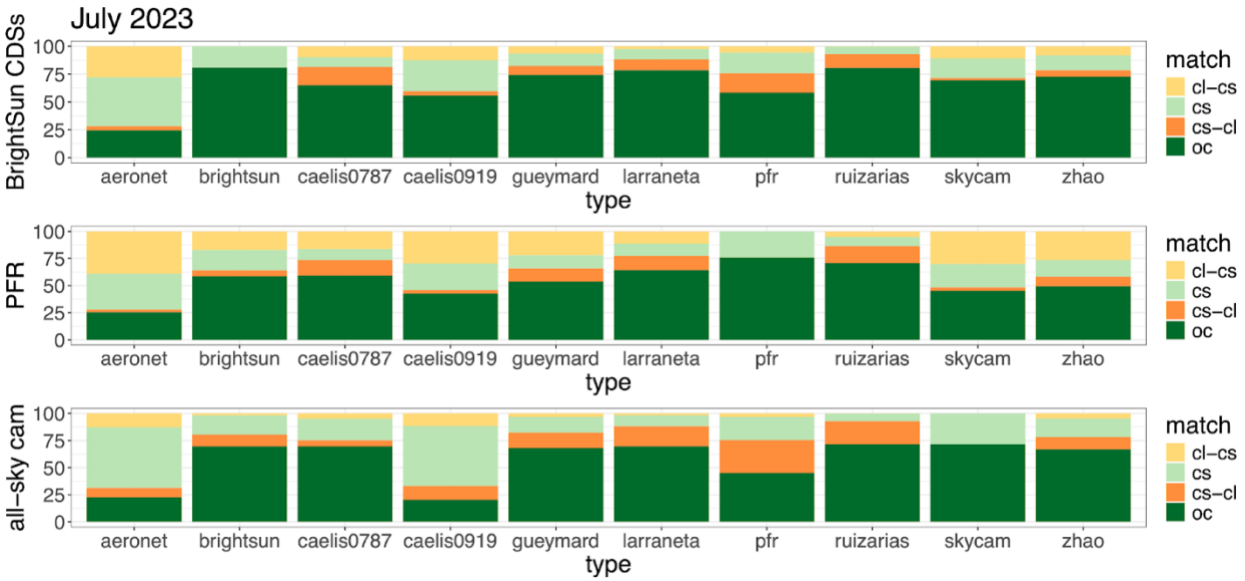

Figure 2.5: Match and mismatch of cloud flags for July 2023. Two CIMEL instruments were available (0787, 0919) and CAELIS processed data from both. cs stands for clear-sky, cl stands for cloudy, cl-cs stands for cloudy (y axis) – clear (x axis), cs -cl for the opposite.

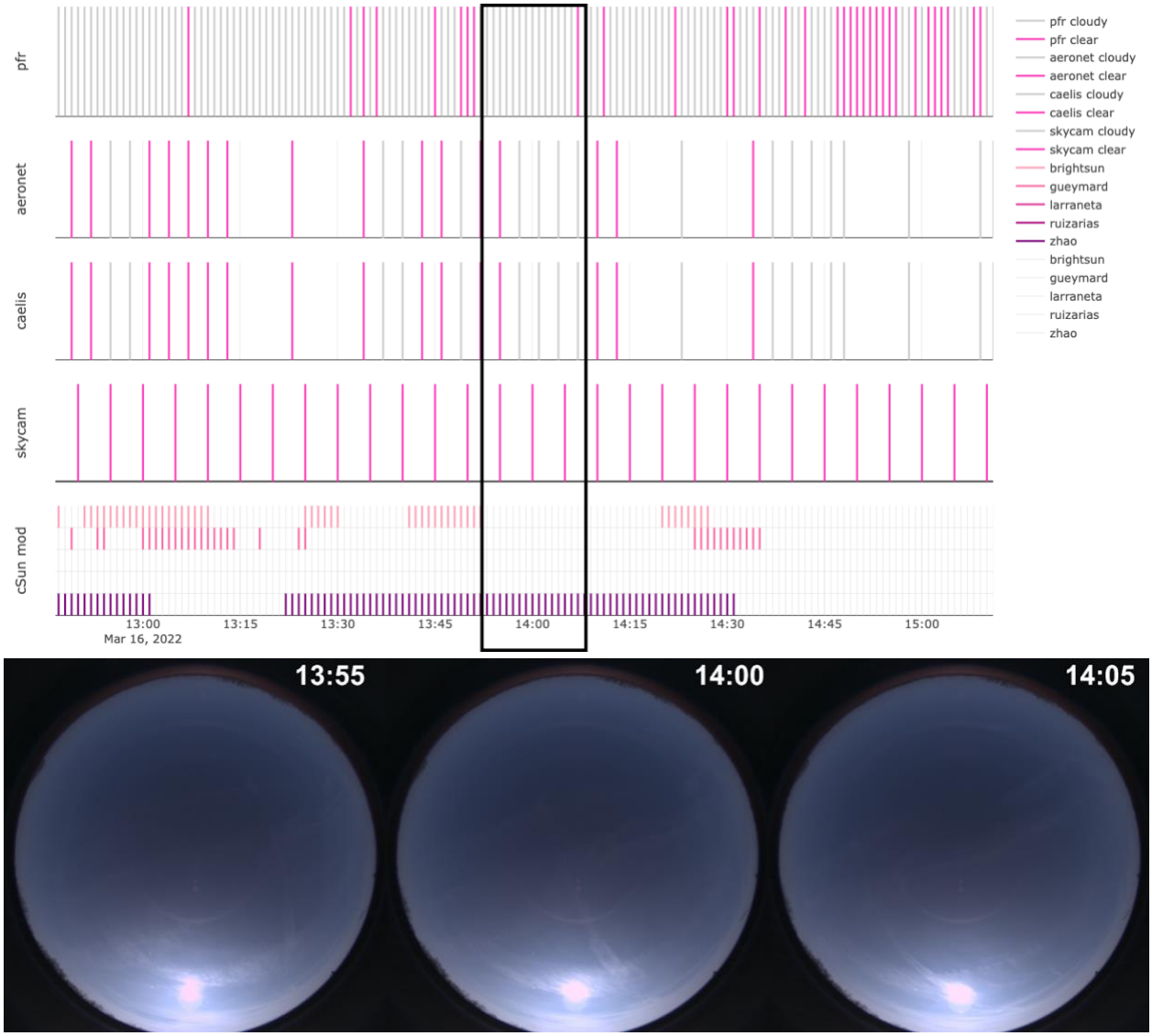

Figure 2.6: example of thin cirrus clouds escaping detection by the all-sky camera sun flagging algorithm and Zhao model, 16 March 2022. Grey lines stand for a cloud flagged measurement, any other color for clear-sky. Last panel shows results for clear sun models (from top to bottom): BrightSun, Gueymard, Larraneta, Ruiz Arias, Zhao.

An issue of the intercomparison is the time homogenisation of the measurements: Cimel measurements (both AERONET and CAELIS) are not made (or at least, saved) at HH:MM:00, unlike PFR, broadband radiometer and all-sky camera data. Therefore, AERONET and CAELIS data within 30 seconds of each other were deemed simultaneous and rounded to the closest minute. Despite the timestamp manipulation to homogenize the data set, comparison of Cimel data to others is difficult: too few data match, especially with the all-sky camera. For March 2022 only

615 or 812 common flags can be found for CIMEL-AERONET and CIMEL-CAELIS, respectively.

The agreement between clear-sun models and the all-sky camera is higher than for clear-sun models and photometers or photometer–photometer. PFR has the lowest agreement with the other instruments/methods (see Fig. 2.4 and 2.5), seemingly because it performs the strictest screening.

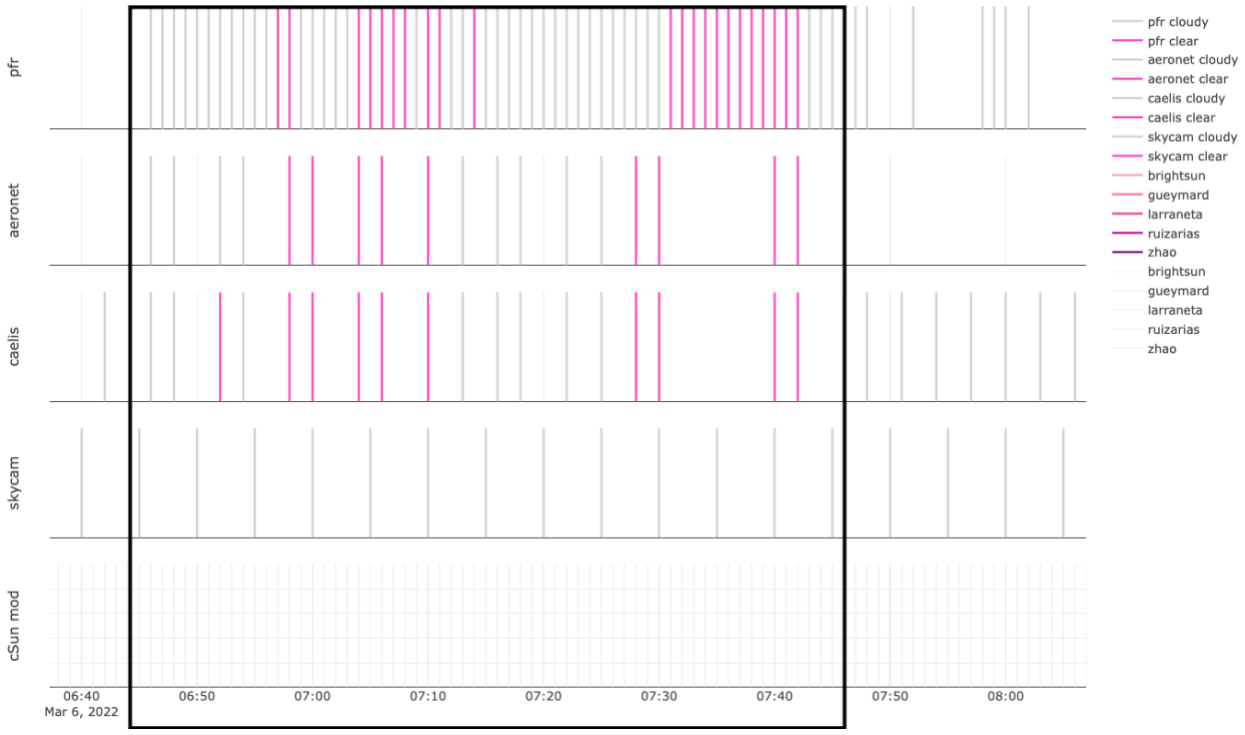

Figure 2.7: example of how the narrower field of view of sun photometers is able to correctly detect the clear sun, 6 March 2022. No images from the OMEA-3C all-sky camera are available, but from visual inspection of a video from another all-sky camera, the sky was very cloudy, with the sun just peeking through clouds between 06:45 and 07:45 UTC. Grey lines stand for a cloud flagged measurement, any other color for clear sky. Last panel shows results for clear sun models (from top to bottom): BrightSun, Gueymard, Larraneta, Ruiz Arias, Zhao.

Different cloudy sky conditions can cause mismatches: thin cirrus clouds, small passing clouds or very cloudy sky but with sun still visible. Thin cirrus clouds in particular can be missed by the all-sky camera algorithm and some broadband radiation-based methods (see Fig. 2.6 for an example). Mismatches can also arise from the different instrument field of views and different measuring techniques (all-sky camera estimates are instantaneous, PFR measurements come from a few

seconds of exposure, whereas Cimel takes measurement in triplet and pyranometer/pyrheliometer measurements are 1-minute averages). Fig. 2.7 gives an example of how the clear sun can only be detected by sun-photometers, but the all-sky camera and also (some) models can fail in flagging it correctly.

No relationship between PFR clear/cloud flags and cloud fraction, either estimated by RADFLUX or all-sky camera algorithm, can be extrapolated, except for when CF is 0 or 1 (totally cloud free sky or totally overcast sky). CF can be any value in between 0 and 1 and the sun can be unobstructed, or a cloud could be in front of the sun even if the sky is mostly cloud-free.

More detail, for July 2023, can be found in the report of the STSM "Application of cloud cover algorithms based on broadband radiation measurements to cloud screening in AOD photometry".

Possible future developments are: analysis of an extended data set, including Prede instruments, focusing on mismatches occurring at very low or very high values of Ångström coefficient; analysis with a higher temporal resolution for all-sky camera products (especially cloud flagging) going to every minute or lower.

2.4 Synergy of sun photometer and spectroradiometer for cloud flagging algorithms assessment (solar)

Contributors: Akriti Masoom, Stelios Kazadzis, Natalia Kouremeti

Masoom et al. (2024a) synergistically leveraged ground-based instruments to analyze the performance of already existing stand-alone algorithms in different scenarios, including periods of high-variability due to clouds, and extreme weather events like wildfires, dust storms, etc. To this direction, we used a co-located Pandonia Global Network Pandora spectroradiometer and Global Atmosphere Watch Precision filter radiometer (PFR) network instrument and analyzed the performance of existing algorithms over the course of 2023 at Izaña station.

PFR and Pandora measurements were synchronized with a time window of 1 min. For this analysis, PFR flags comprise two scenarios for clear-sun and flagged data, while Pandora has nine double-digit quality flags (QF) representing a combination of uncertainty (high: 0, medium: 1, low: 2) and data quality assurance (assured: 0,

not assured:1, unusable data: 2). The analysis revealed good agreement between Pandora QF10 and PFR clear-sun flag (96.45%) followed by QF11 and QF12 (2.29% and 1.26%, respectively) as presented in Fig. 2.8. Conversely, for PFR flagged data, corresponding percentages for Pandora QF10, QF11 and QF12 were 57.83%, 12.58% and 29.6%, respectively.

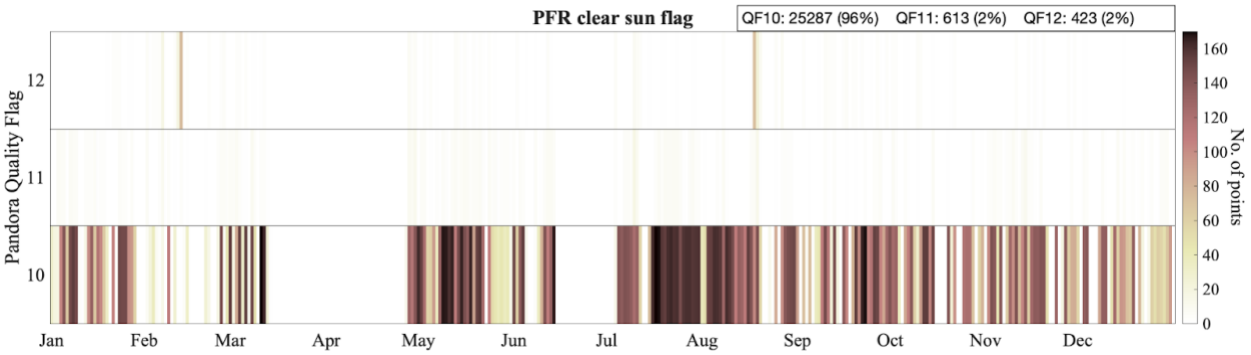

Figure 2.8: Daily variation of Pandora quality flags-based measurement points (QF10, QF11 and QF12) corresponding to PFR clear sun flag for Izaña during 2023.

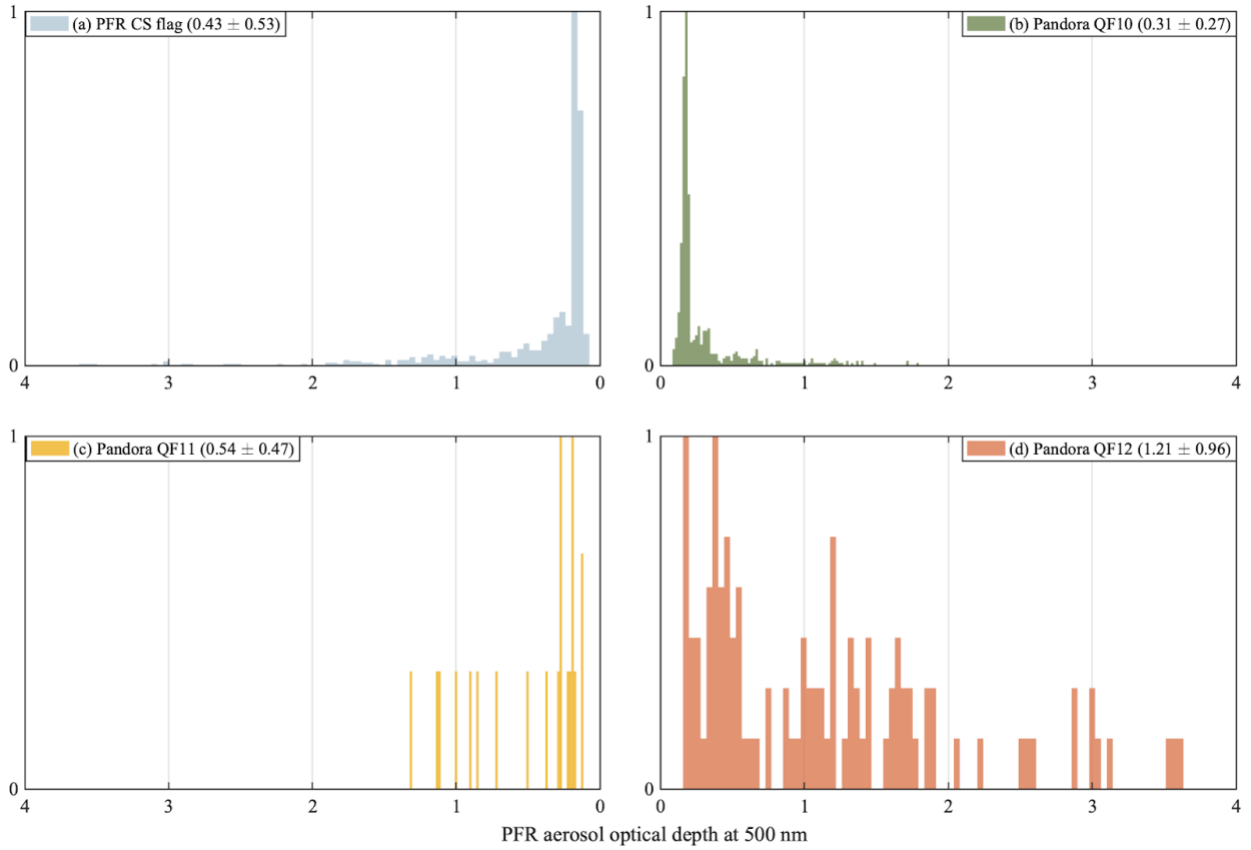

Figure 2.9: Normalised frequency distribution of PFR AOD at 500 nm using (a) PFR clear sun flag and (b-d) Pandora quality flags for smoke cases.

Daily variation of Pandora QFs for 1-year indicated 34 days with Saharan dust episodes (concluded from HYSPLIT 24-h backward trajectories at levels from 500 to 6000 m above ground level originating from the Saharan region) on which for PFR clear sun flag, QF10 flag was more than 90% of daily number of comparison points indicating that dust events did not deteriorate much the flagging agreement between the two instruments. On the contrary, there were 20 dust free days with QF10 below 90% (most days had a number of daily comparison points below 40, indicating high variability due to clouds). PFR clear-sun flag based and Pandora QF10 based AOD distribution showed respective geometric mean ranging from 0.02 to 0.04 and respective standard deviation ranging from 3.24 to 2.35 at 862 nm to 367 nm, respectively. This attempt of synergistic use of different measuring instruments can be useful for enhancing cloud flagging algorithms, thereby contributing to higher quality retrieval products.

The analysis was categorised into three cases as presented below:

Case 1 (Dust): 28 days had Saharan dust events as per HYSPLIT 24-h backward trajectories originating from Sahara and showed good agreement (QF10 > 90%) with the PFR CS flag. Not much difference was observed for PFR CS and Pandora QF10 flag based AOD distributions, while slight difference was observed for Pandora QF11 based AOD distribution that in this (Dust) case seems to be associated with low AOD data points

Case 2 (Smoke): 6 Days with smoke event during August when several fires were burning in Izaña revealed that QF10 (High quality) agreement dropped with more data marked as QF12 (medium quality) and some as QF11 (low quality) (Fig. 2.9). High variation was observed in AOD distributions between PFR CS and Pandora QF with mean of AOD distribution observed to be minimum with QF10 that almost doubles for QF11 and is very high for QF12. This requires further investigation to see if the QFs are correlated with AOD values (i.e., high aerosol content in the atmosphere).

Case 3 (Cloudy): We found 56 days with a number of points < 1/4th of maximum daily points in 2023, 5 of these also had dust and 1 with smoke episodes. More cloudy days were present in the beginning of the year and days had less than 45 daily points. These days there are more % of medium and low-quality data. However, not

much difference was observed for PFR clear sun and Pandora QF10 flag based AOD distributions and slight difference was observed for Pandora QF11 based AOD distribution.

This analysis highlights the importance of specific assessment of smoke events which are tricky for cloud flagging algorithms due to high atmospheric variability especially if the station is located near the fire source. Therefore, synergistic use of instrumentations can provide additional information for cloud flagging specially in the scenario of increasing wildfire smoke events due to ongoing climate change.

2.5 Lunar / stellar photometry: An insight into cloud screening and retrieval techniques

2.5.1 Cloud screening for lunar photometers

Contributors: África Barreto Velasco, Natalia Kouremeti

Cimel photometer in lunar mode: AERONET method

The AERONET product of AOD from Cimel CE318-T lunar measurements was labeled as “Provisional” until 6th August 2024, when this product was reprocessed. AERONET processes the AOD by applying a correction to the ROLO model (Kieffer & Stone 2005) to estimate the extraterrestrial lunar irradiance. However, nowadays there is not any public documentation about how AERONET performs cloud-screening in the night-time lunar data.

The AOD from lunar CE318-T measurements is similarly calculated in CAELIS, but using RIMO (Barreto et al., 2019) instead of ROLO, and applying the so-called RIMO correction factors (RCFs) to correct the RIMO extraterrestrial irradiance values (Román et al., 2020). The night-time AOD cloud-screening in CAELIS is similar to the described for daytime. However, the CE318-T does not perform measurements of lunar aureole sky radiances at night-time; then, the screening of high-altitude clouds cannot be done, in contrast to during daytime. The extraterrestrial lunar irradiance significantly varies during the Moon cycle, therefore, the cloud-screening criteria based on extraterrestrial irradiance are adapted in CAELIS to take this into account.

Lunar PFR

The cloud screening of the lunar irradiance measured with the lunar PFR is similar to the PMOD/WRC PFR cloud screening excluding the Smirnov et al. (2000) and Harrison and Michalsky (1994) methods, explained in Section 2.1.3.

2.5.2 Star photometers retrieval technique (stellar)

Contributors: Sandra Graßl, Roberto Román Diez, Liviu Ivanescu

Cloud-screening for star photometers in Ny-Ålesund (Alfred-Wegener-Institute - AWI)

To remove cloud-contaminated data from the data sets, cloud screening is applied according to AERONET standards (Smirnov et. al., 2000) with some modification due to slight differences between the instruments used at AERONET and AWIPEV. Only measurement points, which fulfill all these criteria are considered as cloud-free and used for further analysis:

- If AOD < -0.01, the measurement point is rejected for this wavelength
- A measurement triplet consists of three measurement points for a single wavelength. A triplet has a duration of 15 min due to its coarser time resolution. The variability between maximum and minimum of the triplet shall be smaller than 0.02
- If the standard deviation of daily averaged AOD < 0.015 or if AE is smaller than three times standard deviation around the daily mean AE, the cloud-screening process is stopped
- The smoothness criterion of the time series is based on limiting the root mean square of the AOD second derivative with time. The second derivative is very sensitive to local oscillations of the cloud optical depth and the threshold of D<16 between two adjacent measurement points is applied closely following Smirnov et.al (2000). The value for the threshold at D=16 is determined analytically and based on measurement data

- We also defined measurements with AOD > 1 as clouds. This criterion might eliminate some aerosol measurements but due to the remoteness of the measurement site, these cases are rare
- With the last criterion we want to have a representative measurement time of the day. If the remaining time is less than 20 min, we discard the entire day

Cloud-screening for EXCALIBUR star photometer (Universidad de Granada)

Another cloud-screening methodology is applied to the data of EXCALIBUR (Pérez-Ramírez et al., 2008), the star photometer installed in Granada (Spain). This cloud-screening procedure follows the next steps (Pérez-Ramírez et al., 2012):

- The star photometer measurements are limited to optical air masses below 3, and all AOD values below their absolute uncertainty are rejected.
- If any pair of consecutive AOD data (obtained always in less than 5–6 min) presents an absolute difference between 0.03, the largest value of the pair is eliminated.
- An AOD value is rejected if its difference from the AOD obtained at the same time, calculated as a moving average of the other measurements at the same wavelength, exceeds three times the standard deviation of the moving average. This process is iterative and continues until no more AOD values are removed. It is applied first with a time window of all-night and after that with a time window of 1 hour.
- If the data eliminated by the previous criteria is more than one third of the original, all the data of that night are removed for a data quality assurance.
- In addition, only the nights that have at least 2 hours of measurements are considered.

Cloud screening for star photometer in the Canadian High-Arctic (Université de Sherbrooke)

In the High-Arctic, the coarse mode aerosols contribute <10% to the total AOD (τa) (O'Neill et al. 2016). Since the coarse mode is predominantly due to cloud particles, one obtains <10% AOD uncertainty simply by screening out the samples with significant coarse mode optical depth (τ_c). Such "spectral" cloud screening can be achieved using the AERONET SDA spectral algorithm (O'Neill et al. 2003). Starphotometers, unlike sunphotometers (Sinyuk et al. 2012; Smirnov et al. 2018), do not suffer from forward scattering errors (Ivănescu et al. 2021); this distinct advantage is attributable to their much smaller field of view. Starphotometers can, accordingly, provide measurements even in the presence of cloud contamination.

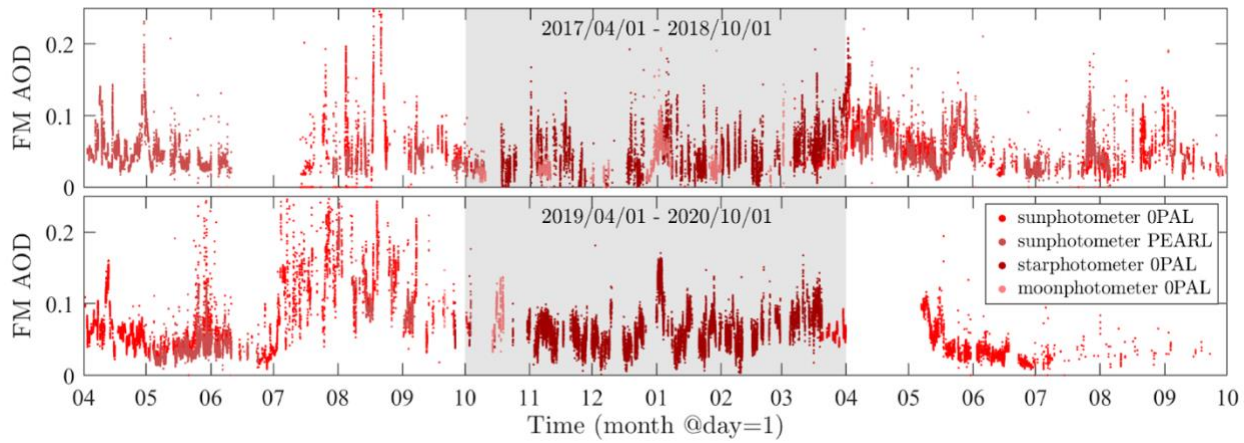

Figure 2.10 Temporal plot of fine mode AOD (FM AOD) at 500 nm, provided by AERONET/AEROCAN Polar-summer retrievals at OPAL and PEARL (Eureka) with starphotometer and AERONET/AEROCAN (OPAL) moonphotometer retrievals, bridging the Polar-winter gap (the lunar-phase dependent moonphotometer retrievals being restricted to about one week per month). Cloud screening is provided by the (spectral) cloud screening capability of the SDA (Spectral Deconvolution Algorithm): however, to reduce the impact of large optical depth clouds on retrieval accuracy we restrict the FM AOD retrievals to those with the coarse mode (CM) AOD < 0.35. The FM and CM AOD are a product of the SDA.

The SDA can, in principle, be employed to extract the fine mode AOD component (τ_f) without discarding any cloud contribution. The SDA may, however, be sensitive to spectral anomalies in raw AOD data which accordingly lead to errors in τ_f. To obtain more credible results, Baibakov et al. (2015) rejected obvious cloud samples

(τ_a<0.35), while O'Neill et al. (2016) proposed an upper limit on the fine mode fraction (τ_f/τ_a > 0.3) to ensure a more reliable comparison with the τf simulations from the GEOS-Chem model. One should also consider a lower OD boundary to ensure the accuracy of the results in the presence of measurement noise (predominantly star scintillation). For telescope diameters > 6 inches the lower limit condition of τ_f > 0.01 is sufficient, while also rejecting unrealistic negative retrievals that can result from the TSM (two-star method) procedure.

Table 2.1 Description of additional cloud screening criterion used in High-Arctics (in addition to Smirnov et al. 2000)

Filter name	Condition	Description
Range	$0 < \tau_a < 0.35$	AOD values should lie within a climatologically defined range. All the points outside the range are removed.
Moving slope	$a < 0.001$ min^{-1}	The time of each measurement is taken as the middle of a 1 h interval. The point is eliminated if the slope of the linear fit (y = at + b) for all τ_a measurements contained in the 1 h interval exceeds an empirically chosen threshold.
Outliers	$\tau_a - \langle\tau_a\rangle < 2.5\sigma$	A point is eliminated, if its difference relative to the average (<>) value for the whole night exceeds 2.5 standard deviations (σ). The procedure is repeated until all the differences are within 2.5σ.

In Eureka, the starphotometer provides data during the six month Polar-winter gap in the sunphotometer measurements (the gray area in Fig. 2.10). The moonphotometer also fills this gap, but only for about one week per month.

Alternative temporal cloud screening approaches similar to those presented in Smirnov et al. (2000) and Pérez-Ramírez et al. (2012) were also investigated in the High-Arctic (Eureka, Canada) (O'Neill et al. 2016). In addition to the τa upper limit from above, two sequential temporal filters were employed by Baibakov et al. (2015): see Table 2.1 below for the protocol. Temporal cloud screening cannot however eliminate homogeneous clouds and cannot avoid eliminating highly variable aerosol events such as the incursion of a strong (fine mode) smoke plume (O'Neill et al.,

2003). Statistically, both methods (temporal and spectral) give similar results for large and diverse ensembles of data.

3. Sun photometers AOD measurements: Inter-comparison and impact of atmospheric parameters

In this section we consider the three instruments (Prede, Cimel, PFR) of the three reference networks (AERONET, GAW-PFR, SKYNET).

Table 3.1: Description of the three main photometer instruments (Cimel, PFR, Prede)

Short name	Manufacturer	Instrument name	Network
Cimel	Cimel Electronique	CE 318 T	AERONET
PFR	PMOD/WRC	Precision Filter Radiometer	GAW-PFR
Prede	Prede Co., Ltd.	POM-O2	SKYNET

Table 3.2: Description of the three reference networks (AERONET, GAW-PFR, SKYNET)

Short name	Full name, support	Website	Instrument
AERONET	AERosol RObotic NETwork, NASA	https://aeronet.gsfc.nasa.gov/	Cimel
GAW-PFR	Global Atmosphere Watch - Precision Filter Radiometer, WMO/GAW	https://gawpfr.pmodwrc.ch/	PFR
SKYNET	International SKYNET DataCenter	https://www.skynet-isdc.org/	Prede

All instruments are photometers using spectral filters and retrieving the AOD using the photometry method (Beer-Bouguer-Lambert equation). More details and descriptions are given in Table 3.1 for the instruments and in Table 3.2 for the networks. The aim of this section is to analyze some comparison experiments (long term observations or campaigns) involving all three instruments (Cimel, PFR and Prede) and the products of the respective networks to which instrument belongs: AERONET for Cimel, SKYNET for Prede and for PFR: A DWD Product based on a retrieval using GAW-PFR algorithm version 2009.

3.1 Cimel-PFR-Prede intercomparisons on Lindenberg - Dataset (2013-2024)

3.1.1 Lindenberg-Dataset a long-term (2013-2024) Cimel-PFR-Prede AOD dataset

In Lindenberg (Tauche, Brandenburg, Germany) at the Meteorological Observatory Lindenberg (Meteorologisches Observatorium Lindenberg - Richard-Aßmann-Observatorium: MOL-RAO) of the German Meteorological Service (Deutscher Wetterdienst: DWD), there are parallel solar photometry measurements of the AOD for the three instruments (Cimel, PFR, Prede) with the three retrieval methods of the reference networks (AERONET, GAW-PFR, SKYNET) since 2013.

We name “Lindenberg-Dataset” these 11 years (2013-2024) Cimel-PFR-Prede AOD dataset of Lindenberg (DWD/MOL-RAO) to make a comparison of the three instruments and retrieval methods. DWD/MOL-RAO at Lindenberg is the only site worldwide having permanent measurements of AOD from all three instruments Cimel, PFR and Prede. Information about the Lindenberg-Dataset is listed below:

- Time resolution: PFR measures every minute. Prede also has a time schedule with a measurement every minute, which is not necessarily an AOD measurement (Prede also measures the sky radiance), while Cimel has a non-fixed time schedule (alternatively AOD measurements and sky radiance measurements) resulting in a temporal resolution for AOD measurements of around 5 minutes.

- Channels: We consider the two spectral channels that are common to all three instruments: 500 nm and 865 nm (varying from 862 to 870 nm depending on the instrument).
- Data availability: PFR and Cimel measure in parallel with the same retrieval method since 2013. Therefore, this comparison includes the years 2013-2023, for which AERONET level 2.0 data are available. Even if there are continuous Prede AOD measurements in Lindenberg since 2013, we only consider the Prede measurements since 2016, which is the beginning of the data availability on the website of International SKYNET DataCenter.
- Product: Table 3.3 summarizes the products used for the comparison Cimel-PFR-Prede on the Lindenberg Dataset.

Table 3.3: Product description for each instrument and network of the Lindenberg-Dataset

Instrument	Network	Product	Availability	Source
Cimel	AERONET	Aeronet AOD (day) Level 2.0	2013-2023	https://aeronet.gsfc.nasa.gov/
PFR	GAW-PFR	AOD GAW Level 3, DWD computation with GAW-PFR algorithm version 2009	2013-2024	DWD, MOL-RAO
Prede	SKYNET	ESR Sunrad V09, Level 2 (until 2021) Level 2A (from 2021)	2016-2024	https://www.skynet-isdc.org/

3.1.2 Comparison studies PFR-Cimel, Prede-PFR and Cimel-Prede of Lindenberg-Dataset

Contributors: Angelos Karanikolas (Study k), Pablo González Sicilia (Study G)

In this section we present a work initiated during the exercises session of HARMONIA Training School “Sky over Berlin” (8-10 April 2024). We categorize two studies here based on the way of synchronization as “Study K” and “Study G”

Table 3.4: Product description for each instrument and network of the Lindenberg-Dataset. Δ refers to difference

Criteria	Study K	Study G
Time Range	PFR vs Cimel: 2013-2023 Prede vs PFR: 2016-2023	PFR vs Cimel vs Prede: 2016 - 2023
Synchronisation	Time interval between each measurement of the pair <= 30 s	30 s tolerance on each plain one-minute timestamps
AOD Filtering (500 nm / 865 nm)	PFR-Cimel: 0.001 < AOD < 3 and ΔAOD < 0.04/0.025, daily mean ΔAOD < 0.012/0.008 80-20_perc ΔAOD < 0.02/0.017 Prede-PFR: ΔAOD < 0.06/0.05	AOD thresholds based on AE range: AE [0 to 0.5]: AOD below 0.5 AE [0.5 to 1]: AOD below 0.35 AE [≥ 1]: AOD below 0.2 AOD inside ±2σ to annual mean (within 1.5 times interquartile range) Linearity: Excluded points with high residuals in AOD linear regression and ΔAOD < 0.08 Removed annual outliers on ΔAOD to minimise discrepancies
AE Filtering	For all: AE < 3.5 PFR-Cimel: AE > 0.01, Prede-PFR: ΔAE < 1, AE > 0.4 Prede, AE > 0.6 for PFR	ΔAE < 0.5
Cloud Screening	Cimel: AERONET, Giles et al. 2019 PFR: GAW-PFR, Kazadzis et al. 2018a Prede: Adapted on compared instrument	Same as study K
Remaining points	For 2016-2023 PFR vs Cimel: 39829 points (70,42 % of 56556 comparison points) PFR vs Prede: 30002 points (33,35% of 89940 comparison points)	For 2016-2023 PFR vs Cimel: 34621 points (80.9% of 42795 comparison points) PFR vs Prede: 22781 points (58.66% of 38834 comparison points) Cimel vs Prede: 20470 points (68.07% of 30071 comparison points)

(because of the different time schedules of each instrument type, the measurement of the two instruments that are compared does not occur at exactly at the same time, we need to define a "synchronization threshold" = a time interval between the two measurements below which we consider that the data are synchronized enough for a comparison) have been done for the comparisons and the quality filter criteria (we reduce the dataset by throwing out some outliers following threshold in e.g., AOD, AE, etc.). Table 3.4 summarizes the synchronizations and filters used in each study. We notice that the filters of the study G are stricter than the ones of the study K for the Prede-PFR comparison (only study on the same interval), since study G has a dataset of 22781 comparison points and study K 30002 comparison points.

3.1.2.1 PFR vs Cimel comparison

Statistical analysis on the complete dataset:

For the Cimel-PFR comparison, study K considers the whole 2013-2023 dataset and study G considers only the 2016 - 2023 time interval. Figure 3.1 shows for the study G the AOD differences PFR-Cimel in dependency of time (a) and (b) and of air mass (c) an (d) for channels 500 nm (a) and (c) and 865 nm (b) and (d). These graphics can

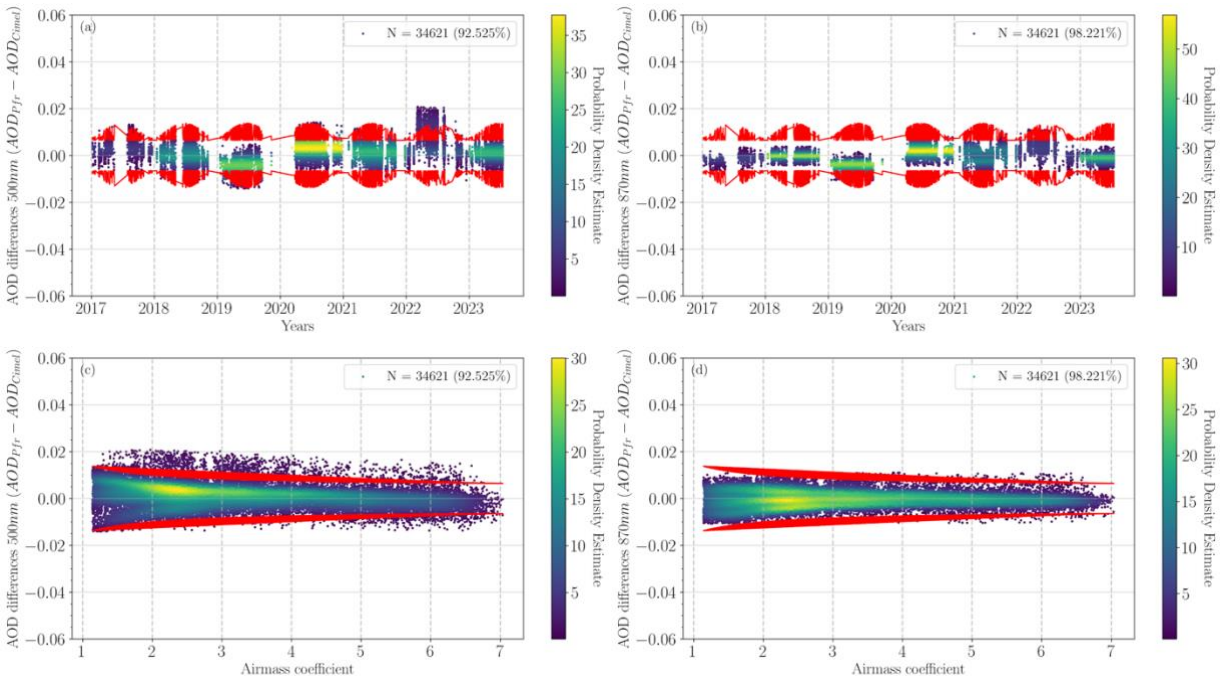

Figure 3.1 AOD differences (PFR-Cimel) (a, b) time series and (c, d) as a function of airmass coefficient. Percentages given in brackets corresponds to the comparison points lying within the WMO limits.

be confronted with the study K, Fig. AP-3.1 (a) and (b) (in dependency of time) and Fig. AP-3.2 (a) and (b) (in dependency of air mass), both in Appendix. Study G has a reduced dataset to 2016-2023 instead of 2013-2023 for study K (Fig. AP-3.1 and AP-3.2). Therefore, the relative weight of bad year 2022 (see following year analysis of study G) should be higher in this study, nevertheless, study G has 0.5% more points in the WMO criteria: 92.5%/98.2% vs 91.7%/97.9% for study K (500/865 nm). Despite these differences of methods and a different time interval, both studies show a good agreement between PFR and Cimel, since more than 90 % (channel 500 nm) and more than 95% (channel 865 nm) of the comparison points are inside the WMO coincidence criteria for both studies.

Statistical year to year (study G only):

Study G shows the statistics of the AOD difference PFR-Cimel for each year separately. Linear fits (Figures 3.2 for 500 nm and AP-3.3 in Appendix for 865 nm) indicate strong agreement for both channels, with low root mean square error (RMSE) values ranging from 0.002 to 0.006 for the 500 nm channel and from 0.003 to 0.004 for the 865 nm channel, along with high correlation coefficients ($R^2 > 0.9$ each year for both channels). The year 2022 showed the largest discrepancies, with

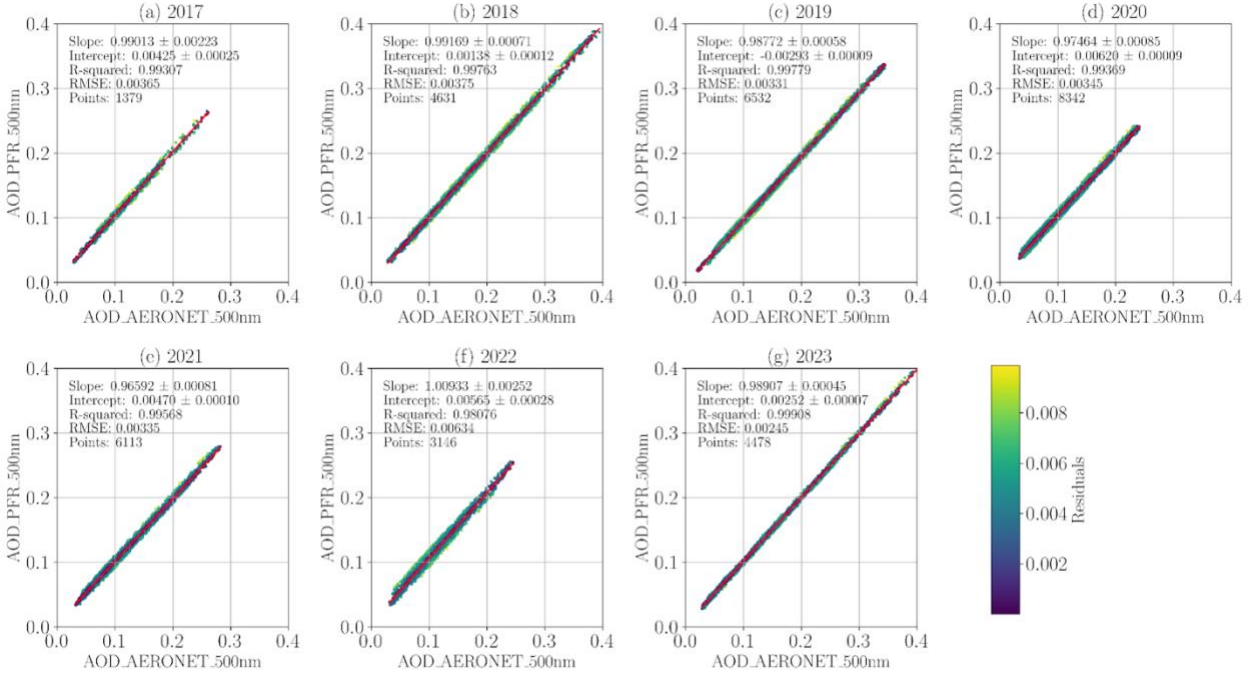

Figure 3.2 (a-g) Yearly linear fit of PFR AOD vs AERONET Cimel AOD at 500 nm from 2017-2023.

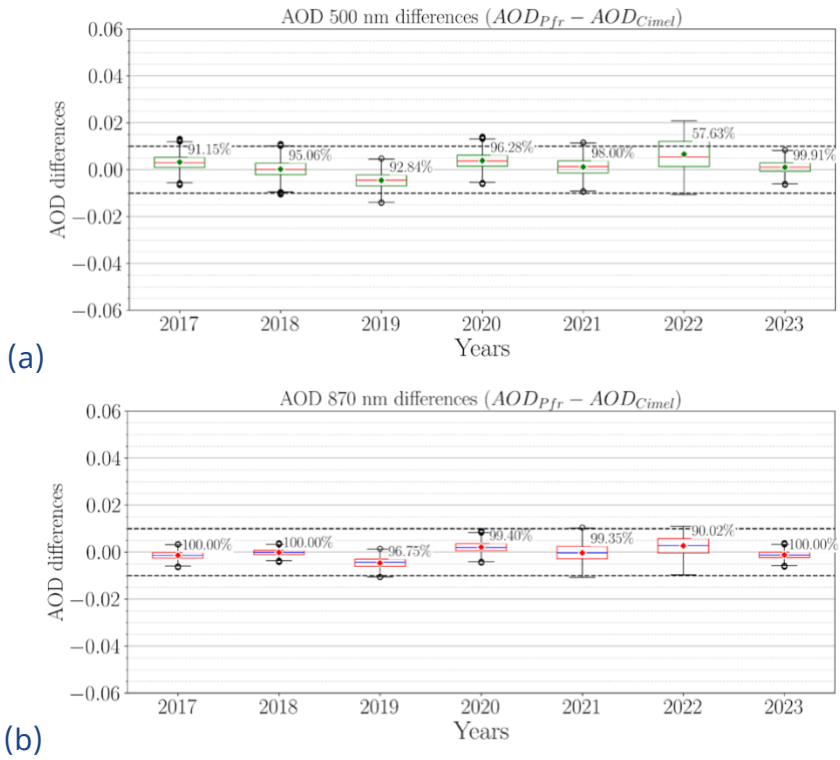

Figure 3.3 AOD differences (boxplot-yearly) as (AOD_PFR - AOD_Cimel) at (a) 500 nm and (b) 865 nm. The rhombus represents the mean difference, and the line within each box indicates the median difference. The percentage shows the proportion of values within WMO limits, while black circles denote outliers. The black dashed lines represent the ±0.01 limits.

RMSE values peaking at 0.006 for the 500 nm and 0.004 for the 870 nm channels. The statistical information (number of points: N and RMSE) are reported in Table 3.5 (for channel 500 nm) and in Table 3.6 (for channel 865 nm).

Figure 3.3 shows yearly comparisons between the instruments and reveal that the WMO traceability criteria (95% of differences inside WMO limits, defined as ±(0.005 + 0.01/m), where 'm' denotes the optical air mass) were met for the 500 nm channel in 2018, 2020, 2021, and 2023. For the 865 nm channel, the criteria were met consistently each year except in 2022, which showed the weakest agreement across both channels, as seen from the linear fits (Figures 3.2 and AP-3.3). In particular, the Cimel underestimated the AOD compared to the PFR, especially for the 500 nm channel, with only 57.63% and 90.02% of the points falling within WMO limits for the 500 nm and 870 nm channels, respectively. Overall, agreement was stronger in the 865 nm channel, with reduced variation in the differences. Despite variations, the median and mean differences for both channels remained below ±0.01 for all years.

Analysis on the different Cimel units: Cimel #787 and Cimel #919 - study G

An analysis of the specific Cimel photometers used at Lindenberg (Fig. 3.4) highlighted that unit #787 had the lowest agreement with the PFR, especially in the 500 nm channel, with only 88.01% of measurements meeting WMO limits. This unit was the primary instrument in 2022, providing 82.55% of AERONET AOD data in the Lindenberg-Dataset, likely contributing to the poor agreement observed that year. Additionally, unit #919 showed a slight AOD overestimation relative to the PFR, while unit #787 consistently underestimated it. Nonetheless, both units maintained a strong overall alignment with the PFR, with mean and median differences remaining below ±0.01 over the study period. Overall agreement for both units was quite good, with mean and median differences remaining below ±0.01 throughout the comparison period.

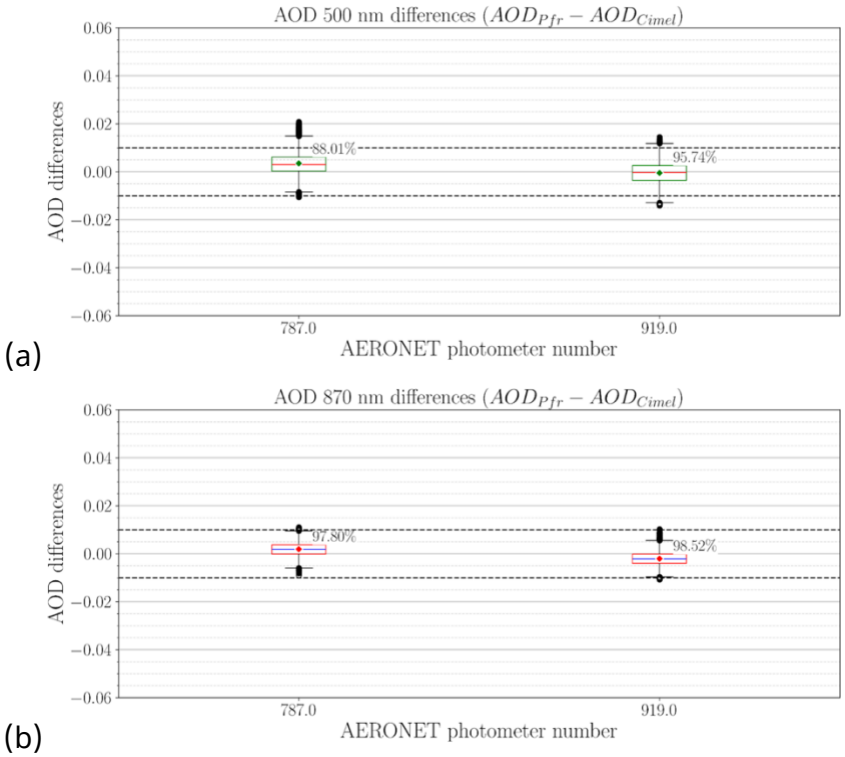

Figure 3.4 AOD differences (boxplot-instrument wise) as (AOD_PFR - AOD_Cimel) at (a) 500 nm and (b) 870 nm. The rhombus represents the mean difference, and the line within each box indicates the median difference. The percentage shows the proportion of values within WMO limits, while black circles denote outliers. The black dashed lines represent the ±0.01 limits.

The difference of behavior between Cimel #787 and Cimel #919 reveals an instrumental issue at DWD site in Lindenberg, pointing out probable weaknesses of the Cimel #787. The answer is therefore probably not in the interpretation of the retrieval process (GAW-PFR vs AERONET) but in the station logbook of Lindenberg (specific station issue).

3.1.2.2 Prede vs PFR comparison

Statistical analysis on the complete dataset (study G only):

For the Prede-PFR comparison, studies K and G consider the same 2016-2023 time interval.

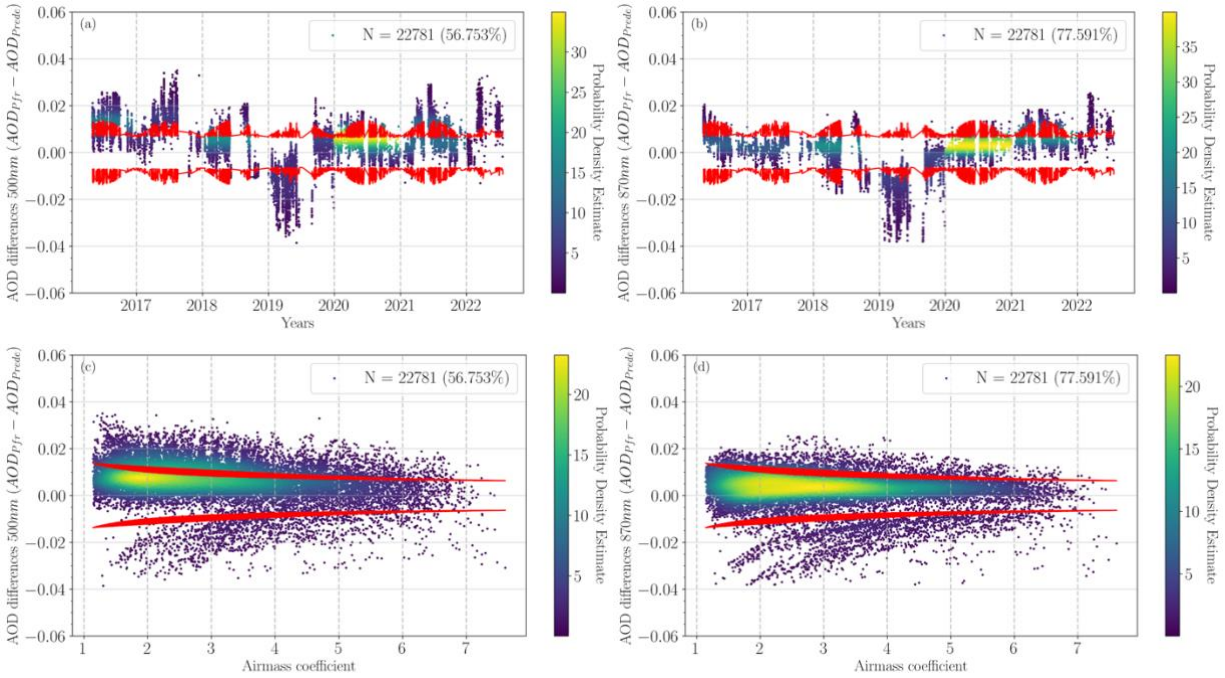

Figure 3.5: AOD differences (PFR-Prede) (a, b) time series and (c, d) as a function of airmass coefficient. Percentages given in brackets corresponds to the comparison points lying within the WMO limits.

Figure 3.5 shows for study G the AOD differences PFR-Cimel in dependency of time (a) and (b) and of air mass (c) an (d) for channels 500 nm (a) and (c) and 865 nm (b) and (d). These graphics can be confronted with the study K, Fig. AP-3.1 (c) and (d) (in dependency of time) and Fig. AP-3.2 (c) and (d) (in dependency of air mass). The only difference between the two studies is the filtering, resulting in a third less points of comparison in study G (Fig. 3.5): 22781 points vs study K (Fig. AP-3.1 and AP-3.2 (c) and (d)): 30002 points. Study G criteria seem to be stricter and seem to

have less outliers than study K. We see it in the statistics: Study G statistics have more percentage of points in the WMO criteria (500/865 nm: study G 56.8%/77.6% vs 53.1%/62.7% for study K). Both studies show a poor agreement of PFR vs Prede considering the WMO criteria of coincidence, especially for the 500 nm channel (around 55 % inside the WMO limits for both studies).

Statistical year to year (study G):

Study G shows the statistics of the AOD difference PFR-Prede for each year separately. Linear fits (Fig. 3.6 for channel 500 nm and Fig. AP-3.4 in Appendix for channel 865 nm) provide further insight, revealing higher RMSE and residual values compared to the PFR-Cimel comparison (Fig. 3.2 and AP-3.3). Specifically, RMSE values ranged from 0.005 to 0.01 for the 500 nm channel and from 0.005 to 0.007 for the 865 nm channel, highlighting a lower agreement between these instruments. Despite the increased RMSE and residuals, a strong correlation remains evident, with R^2 values exceeding 0.9 for all years. The statistical information (number of points: N and RMSE) are reported in Table 3.5 (for channel 500 nm) and in Table 3.6 (for channel 865 nm).

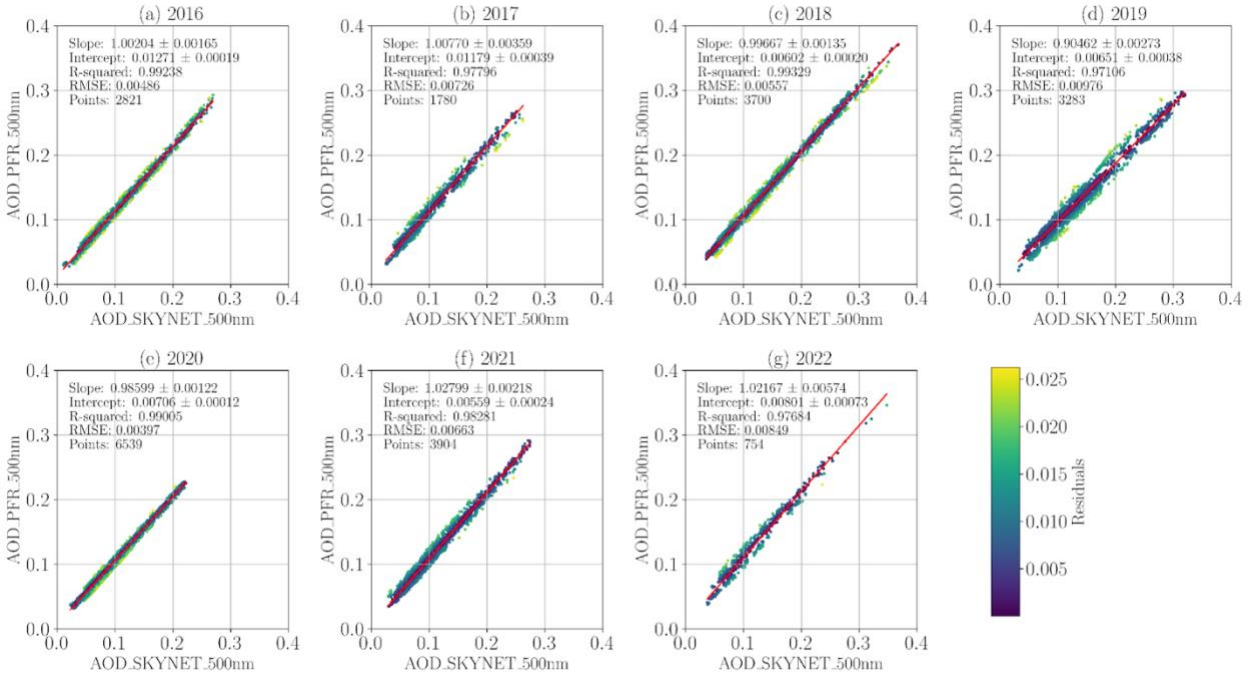

Figure 3.6 (a-g) Yearly linear fit of PFR AOD vs SKYNET Prede AOD at 500 nm from 2016-2022.

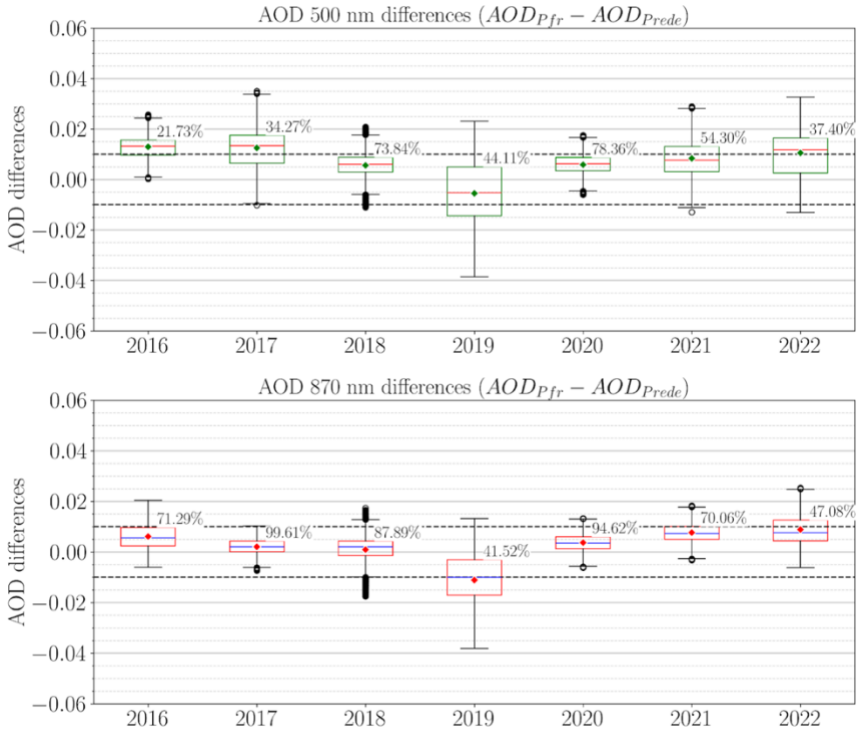

Figure 3.7 AOD differences (boxplot-yearly) as (AOD_PFR - AOD_Prede) at (a) 500 nm and (b) 870 nm. The rhombus represents the mean difference, and the line within each box indicates the median difference. The percentage shows the proportion of values within WMO limits, while black circles denote outliers. The black dashed lines represent the ±0.01 limits.

This trend is also reflected in the annual difference comparison (Figure 3.7). For the 500 nm channel, median differences stayed below ±0.01 only in 2018, 2019, 2020, and 2021, while the 865 nm channel maintained this range for all years except 2019. The larger interquartile ranges, shown by the box sizes, indicate greater dispersion in differences, aligning with the observed standard deviation values. Regarding the WMO limits and meeting of the WMO traceability criteria (95% of differences inside WMO limits, defined as ±(0.005 + 0.01/m), where 'm' denotes the optical air mass), there's no year meeting this condition for 500 nm channels, while for the 865 nm the criteria is met only for 2017 with 99.61% of points inside them. Finally, a marked inconsistency between channels is clearly visible, for example, in the 500 nm channel, only 21.73% and 34.27% of the points were within WMO limits in 2016 and 2017, whereas for 865 nm, the numbers were significantly higher at 71.29% and 99.61% for the same years.

3.1.2.3 Prede vs Cimel comparison

Statistical analysis on the complete dataset (study G only):

Figure 3.8 clearly highlights the substantial discrepancies during the first three years, with broad interquartile ranges that show the high deviation values, as evident from the size of the boxes. The lowest instrument agreement occurs in 2019, where only 8.36% and 5.66% of data points fall within WMO limits for the 500 nm and 865 nm channels, respectively. In contrast, the highest agreement is observed in 2020 for the 500 nm channel, with 89.38% of points meeting WMO limits, and in 2020 and 2022 for the 865 nm channel, with 99.50% and 99.69% of points within WMO

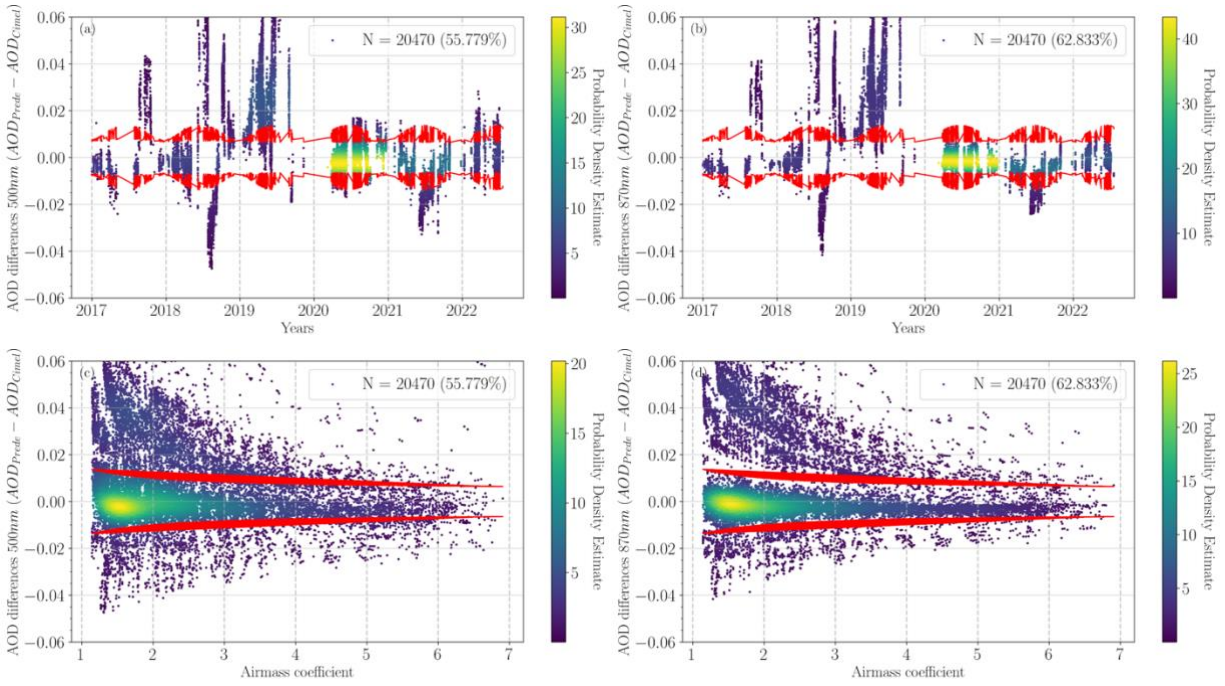

Figure 3.8: AOD differences (Prede-Cimel) (a, b) time series and (c, d) as a function of air mass coefficient. Percentages given in brackets corresponds to the comparison points lying within the WMO limits.

limits, respectively. The lack of large deviations in the other comparisons (PFR-Cimel and PFR-Prede) suggests that unfiltered, cloud-contaminated data points may be a key factor in the substantial AOD discrepancies observed between Cimel and Prede. Furthermore, the increase in AOD measurements by Prede in 2019 (evident in both Prede comparisons: PFR-Prede and this one) points to potential calibration or technical issues, as discrepancies of this magnitude are unlikely to result solely from retrieval methods.

Statistical year to year (study G only):

Linear fits (Fig. 3.9 for 500 nm and AP-3.5 in Appendix for 865 nm) indicate that the early years (2017, 2018, and 2019) exhibit larger discrepancies in AOD values between the channels, with RMSE values of 0.01–0.02 from study G. In contrast, the later years (2020, 2021, and 2022) show improved agreement, with RMSE values reduced to 0.005–0.008 for the 500 nm channel and 0.002–0.003 for the 865 nm channel.

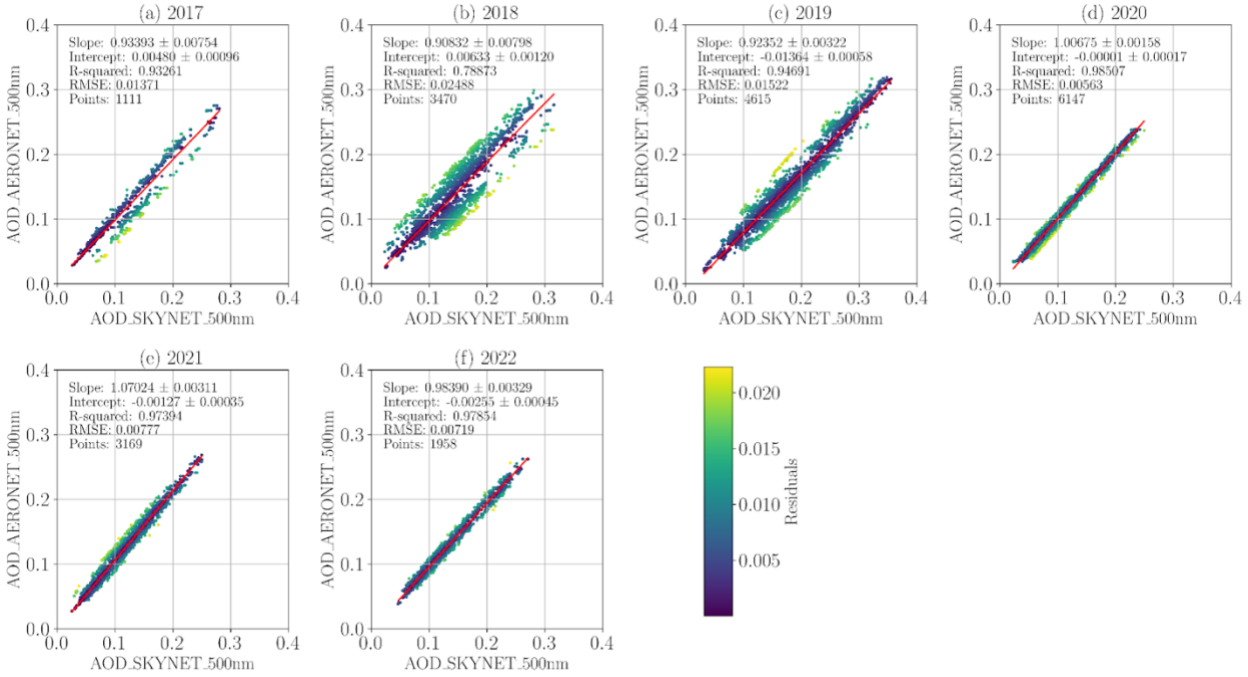

Figure 3.9 (a-f) Yearly linear fit of AERONET Cimel AOD vs SKYNET Prede AOD at 500 nm from 2017-2022.

This trend is also reflected in the correlation coefficients. For the 500 nm channel, the R^2 value in 2018 is approximately 0.79, whereas for the 865 nm channel, correlation is even lower, with an R^2 of around 0.35 in 2018 and 0.78 and 0.74 in 2017 and 2019, respectively while for the later years this coefficient is over 0.9. Considering the differing measurement intervals (around 5 minutes for the Cimel, 1 minute for PFR and around 3 minutes for Prede) a significant portion of the observed discrepancies may stem from unaccounted cloud contamination on the Prede side. These contamination issues are not fully addressed when aligning measurements with AERONET data, likely contributing to the inconsistencies observed between instruments (discrepancies that are notably less pronounced in the PFR-Prede

comparison). The statistical information (number of points: N and RMSE) are reported in Table 3.5 (for channel 500 nm) and in Table 3.6 (for channel 865 nm).

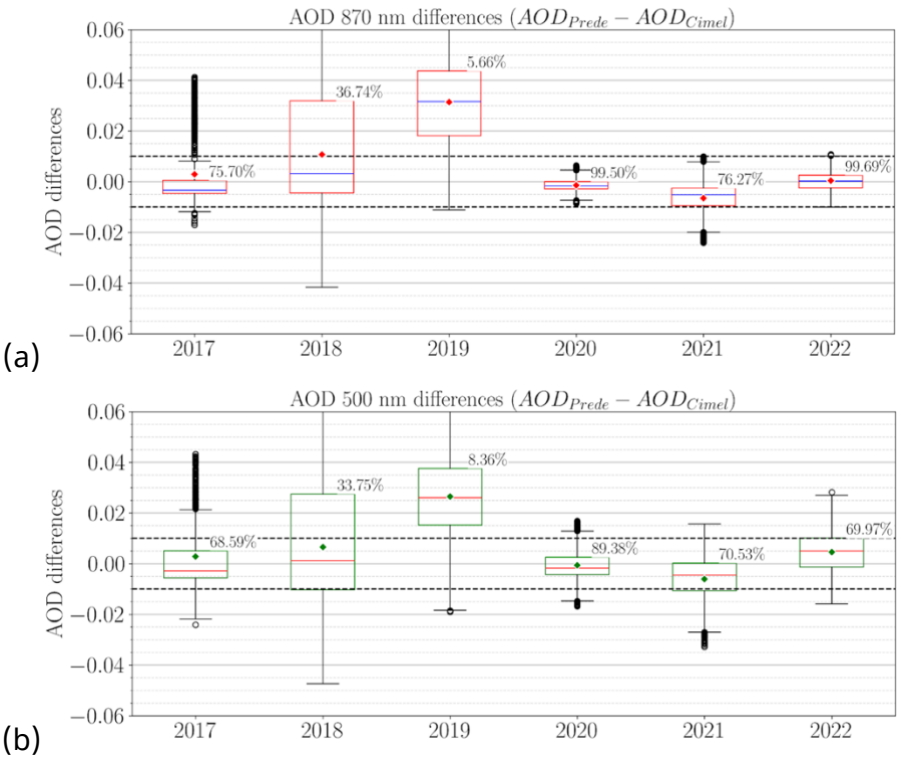

Figure 3.10 AOD differences (boxplot-yearly) as (AOD_Prede - AOD_Cimel) at (a) 500 nm and (b) 865 nm. The rhombus represents the mean difference, and the line within each box indicates the median difference. The percentage shows the proportion of values within WMO limits, while black circles denote outliers. The black dashed lines represent the ±0.01 limits.

Figure 3.10 clearly highlights the substantial discrepancies during the first three years, with broad interquartile ranges that show the high deviation values, as evident from the size of the boxes. The lowest instrument agreement occurs in 2019, where only 8.36% and 5.66% of data points fall within WMO limits for the 500 nm and 865 nm channels, respectively. In contrast, the highest agreement is observed in 2020 for the 500 nm channel, with 89.38% of points meeting WMO limits, and in 2020 and 2022 for the 865 nm channel, with 99.50% and 99.69% of points within WMO limits, respectively. The lack of large deviations in the other comparisons (PFR-Cimel and PFR-Prede) suggests that unfiltered, cloud-contaminated data points may be a key factor in the substantial AOD discrepancies observed between Cimel and Prede. Furthermore, the increase in AOD measurements by Prede in 2019 (evident in both Prede comparisons: PFR-Prede and this one) points to potential calibration or

technical issues, as discrepancies of this magnitude are unlikely to result solely from retrieval methods.

Analysis on the different Cimel units: Cimel #787 and Cimel #919 (study G only):

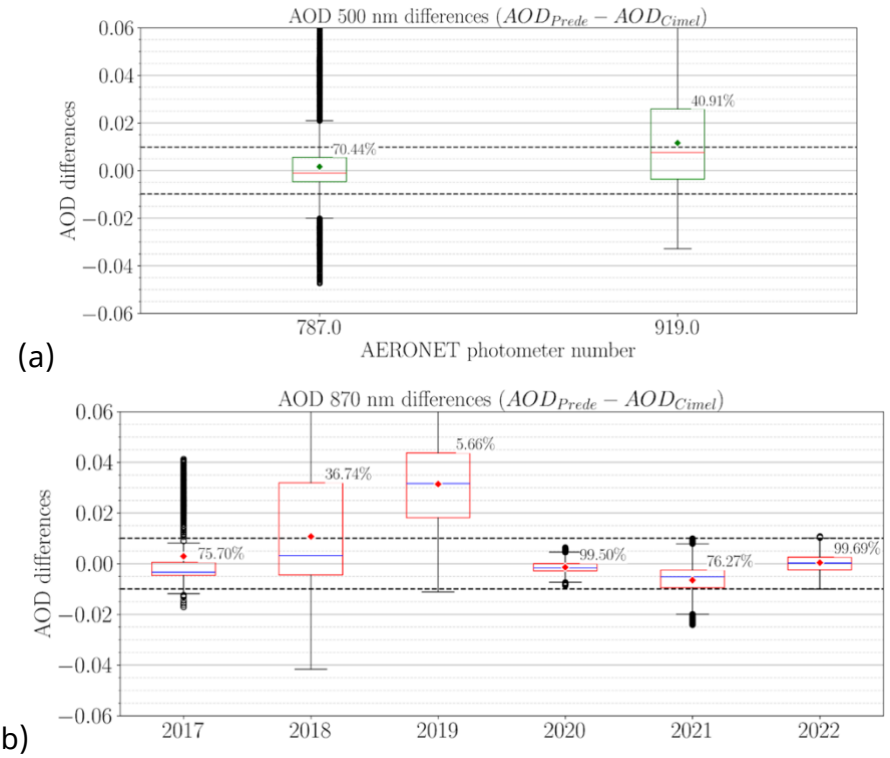

Figure 3.11 AOD differences (boxplot-instrument wise) as (AOD_PFR - AOD_Cimel) at (a) 500 nm and (b) 865 nm. The rhombus represents the mean difference, and the line within each box indicates the median difference. The percentage shows the proportion of values within WMO limits, while black circles denote outliers. The black dashed lines represent the ±0.01 limits.

As with the PFR-Cimel comparison, an analysis of the Cimel photometers used at Lindenberg (Figure 3.11) was performed. Unit #787 exhibited the best agreement with Prede across both channels, showing low median differences and less dispersion, though it had a higher number of outliers compared to unit #919, which displayed greater overall variability. This finding contrasts with the PFR-CIMEL comparison, where unit #919 showed the strongest agreement with PFR, while unit #787 consistently underestimated AOD. Although neither unit fully met the WMO traceability criteria for both channels, median differences for both remained within ±0.01.

3.1.2.4 Results analysis and summary

Table 3.5 (channel 500 nm) and Table 3.6 (channel 865 nm) summarize for each year the statistical elements of the comparison (number of comparison points, RMSE) for study G.

Table 3.5: Points of comparison (N) and statistical difference (RMSE) over the years (2016-2023) for Cimel-PFR and PFR-Prede and Prede-PFR using the Lindenberg-Dataset (500 nm channel); bold: RMSE > 0.006; No RMSE shown ("excl.") if not enough comparison points (N).

Year	PFR-Cimel		PFR-Prede		Cimel-Prede	
	N	RMSE	N	RMSE	N	RMSE
2016	55	excl.	2821	0.00486	31	excl.
2017	1379	0.00365	1780	**0.00726**	1111	**0.01371**
2018	4631	0.00375	3700	0.00557	3470	**0.01522**
2019	6532	0.00331	3283	**0.00976**	4615	**0.01522**
2020	8342	0.00345	6539	0.00397	6147	0.00563
2021	6113	0.00335	3904	**0.00663**	3169	**0.00777**
2022	3146	**0.00634**	754	**0.00849**	1958	**0.00719**
2023	4478	0.00245	8	excl.	114	excl.

This statistical overview of all years and the analysis of the graphics above (years and instruments) lead to following conclusions for each pair of comparison:

Cimel vs. PFR:

- Yearly analysis (Figure 3.3) shows a good agreement between PFR and Cimel, with most years (2018, 2019, 2020, 2021, and 2023) meeting WMO criteria. Also Figure 3.2 (study G) and Figures AP-3.1 and AP-3.2 (study K) show that the WMO criteria are well respected in both studies (> 90 % for 500 nm and > 95 % for 865 nm)

- Instrument wise analysis (Figure 3.4) show that Cimel #787 underestimates the AOD compared to PFR, while Cimel #919 shows better agreement (for 500 nm). At 865 nm: Both Cimel instruments (#787 and #919) meet WMO criteria, with Cimel #787 showing slightly better agreement.

Table 3.6: Points of comparison (N) and statistical difference (RMSE) over the period of analysis from 2016-2023 for Cimel-PFR and PFR-Prede and Prede-PFR using the Lindenberg-Dataset (865 nm channel); bold: RMSE > 0.006; No RMSE shown ("excl.") if not enough comparison points (N)

Year	PFR-Cimel		PFR-Prede		Cimel-Prede	
	N	RMSE	N	RMSE	N	RMSE
2016	55	excl.	2821	0.00461	31	excl.
2017	1379	0.00180	1780	0.00300	1111	**0.01145**
2018	4631	0.00152	3700	0.00546	3465	**0.01996**
2019	6532	0.00216	3283	**0.00690**	4614	**0.01298**
2020	8342	0.00243	6539	0.00321	6147	0.00260
2021	6113	0.00329	3904	0.00395	3168	**0.00610**
2022	3146	0.00397	754	0.00578	1958	0.00356
2023	4478	0.00180	8	excl.	114	excl.

Prede vs. PFR

- Figure 3.5 (study G) shows a poor agreement to WMO criteria especially for channel 500 nm (56.753%) a bit better for channel 865 nm (77.591%). Similar observations for study K in Figures AP-3.1 and AP-3.2, even worse (53.1% and 62.7 %)
- Yearly analysis (Figure 3.7) shows that at channel 500 nm, Prede tends to underestimate AOD compared to PFR, especially in 2016. Regarding the WMO traceability criteria, there's no year meeting it for this channel.

Cimel vs. Prede:

- Figure 3.8 (study G) shows a very poor agreement to WMO criteria: 55.779% (channel 500 nm) and 62.833% (channel 865 nm).
- Yearly analysis graphics (Figure 3.10) show that for channel 500 nm, we have a poor agreement with no year meeting WMO criteria. Worst performance was in the year 2019, best one in 2017.
- Instrument wise analysis (Figure 3.11) shows that for 500 nm, Cimel #787 agrees better with Prede than Cimel #919 does, but neither fully meets the criteria. For 865 nm, Cimel #787 meets the WMO traceability criteria, and Cimel #919 improves the agreement with Prede, but still doesn't meet the criteria.

Summary:

1. Best agreement is between PFR and Cimel (Table 3.5 and 3.6 and Boxplot-Yearly figures). The Prede instrument is an outlier having an RMSE between 0.002 and 0.003 higher than for the comparison PFR vs Cimel.
2. Worst years for Prede is 2019 followed by 2022 and 2017 (reference: PFR-Prede comparison at 500 nm, Table 2.3)
3. Worst year for PFR vs Cimel comparison is 2022 and the difference regarding the instrument type (#787 or #919) is a confirmation that the problem is by the Cimel instrument.
4. The increase in difference values in 2018, 2019, and 2023 indicates that Cimel generally measured lower AOD than Prede during these intervals.
5. The good results in 2016 is an artifact due to the low number of coincident points (only 75), while the poor results in 2023 may also be due to the low number of points measured only by Cimel #919 (only 583). It may be worth considering discarding these years.
6. The best years were 2020, and 2022, as seen from the linear fits and Boxplots-Years graphics.

3.1.3 Summary of the studies on Lindenberg-Dataset

Results of both studies (K and G) show that:

- PFR and Cimel AOD datasets are close enough to consider the impact of retrieval method (GAW-PFR and AERONET network respectively): Over 90% of coincidence to WMO criteria.
- Prede AOD coincidence to other instruments is too far away to look at these considerations. The difference may be due to the very different calibration method used by Prede (see HARMONIA Working Group 2, Deliverable D2.2).
- Worst year for PFR vs Cimel comparison is 2022 and the difference regarding the instrument type (#787 or #919) is a confirmation that the problem is by the Cimel instrument. This points out the necessity of considering the logbooks of the stations (dates of calibration, robotic troubles, spiders in the collimator tubes, etc.) and make a filter on the data.
- We observe some differences in the statistics depending on the way the data synchronisation and data filtering is done: For instance for Prede vs PFR comparison, study K (Fig. AP3.1 and AP3.2) and study G (Fig. 3.8 c and d) consider the same time interval of Lindenberg-Dataset but have considered 30002 points of comparison (study K) vs 22781 (study G), resulting in a difference in percentage of points respecting the WMO criteria: (500/865 nm: 53.1%/62.7% for study K and 56.8%/77.6% for study G).

From this analysis we can conclude that:

1. The first source of difference is the calibration method (Cimel and PFR have the same kind of calibration, Prede uses its own onsite calibration method).
2. The second source of difference are calibration status of the instrument or small technical issues of the instruments (revealed with the Cimel #787 vs Cimel #919 comparison to PFR). This encourages us for further studies to have a look at qualitative information of the station's logbook to filter the dataset.
3. The retrieval method (defined by the network) seems to be the last source of difference but should be quantified and harmonized.

3.2 Campaign SCILLA (solar and lunar) at Lindenberg in 2020

In Lindenberg at DWD/MOL-RAO observatory, there is not only a 11 year dataset of parallel AOD measurements with sun photometers Cimel, PFR and Prede during the day (Lindenberg-Dataset presented in Section 3.1), but also some permanent lunar AOD measurements with the Cimel CE 318-T instruments and some permanent stellar AOD measurement (2013-2022)

To compare the AOD lunar and stellar of different instruments (lunar and stellar photometers: lunar PFR, hybrid Prede POM-02 in lunar modus, hybrid Cimel CE318-T in lunar modus, stellar photometer Schulz & Partner SPST), we organised in August and September 2020 the campaign SCILLA (Summer Campaign for Intercomparison of Lunar measurements of Lindenberg's Aerosol).

SCILLA took place during the moon cycle of August & September 2020 at the meteorological observatory MOL-RAO (Meteorological Observatory Lindenberg - Richard Aßmann Observatory) of DWD (Deutscher Wetterdienst: German meteorological service) in Lindenberg (Tauche) in the North-Eastern region of Germany: Brandenburg.

SCILLA deployed a wide instrumentation of photometers during days (sunphotometers) and nights (lunar photometers, stellar photometers). Regarding aerosol remote sensing, the photometer measurements have been completed by permanent instrumentation of MOL-RAO: Raman, spectral and polarised lidar RAMSES, ceilometers and COBALD (Compact Optical Backscatter AerosoL Detector: Brabec et al. 2012) aerosol radiosounding carried by balloons (provided by MOL-RAO and Meteoswiss). An OMEA-3C red-green-blue fish-eye all-sky camera was also deployed, provided and managed by GOA (Grupo de Óptica Atmosférica) from UVa (University of Valladolid).

The instrumental suite of MOL-RAO which is a supersite for atmospheric measurements provided all ancillary and complementary parameters (eg TOD: Total Ozone Column).

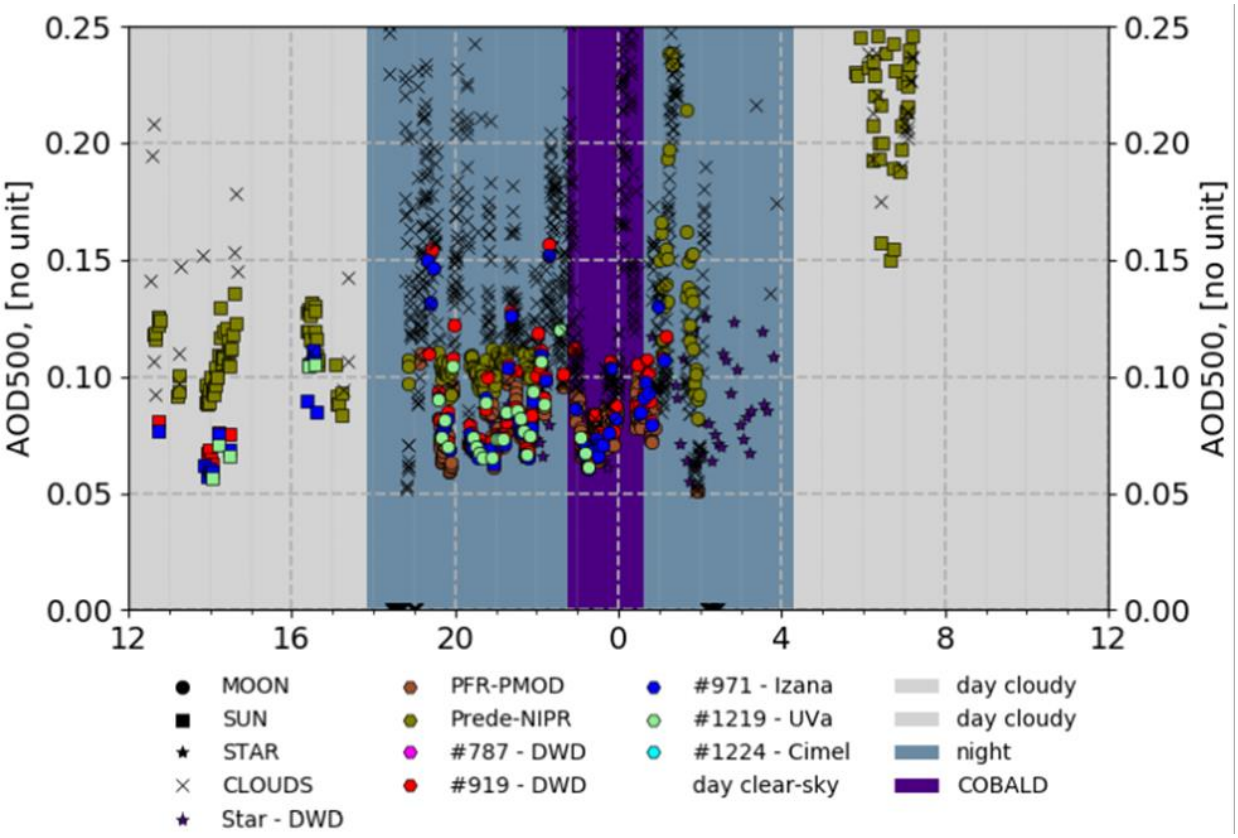

Figure 3.12 Intercomparison of AOD measurement during SCILLA for 5 Cimel (Lunar/Solar) photometers, one Lunar PFR, one Prede (Lunar/Solar) and one stellar photometer for night measurements of 31 August to 01 September 2020.

Lunar photometers of all existing types have been deployed: 5 from type Cimel, allowing an "intern-cimel comparison", 1 from type PFR and one from type Prede-POM. Cimel lunar photometers data have been processed with two different lunar reluctance models (ESA/LIME and RIMO). Two starphotometers have been runned, and during the days, 8 sun photometers were measuring the AOD: 5 Cimels, 2 Prede-POM and 1 PFR. See Figure 3.12 for an example of intercomparison of all photometer measurements during the night of 31 August to 01 September 2020.

Therefore, SCILLA was the first measurement campaign comparing the three systems Cimel, PFR and Prede in lunar modus.

Thanks to all side data of supersite Lindenberg (Pressure, total ozone column), and asking the instrument PIs for raw data (total ozone column), it was possible to retrieve the AOD in a common harmonized way regarding air masses, Rayleigh optical Depth, Ozone and NO_2 optical depth. Therefore, the AOD differences are only

due to instrumental issues (calibration, pointing) or to the lunar reflectance model used.

During SCILLA, only the Lunar PFR and the Lunar+Solar hybrid Cimel photometers were already in an operational mode regarding lunar reflectance model. The lunar reflectance mode and calibration for the moon of the Prede in lunar modus has been transferred from one Cimel to the Prede instrument, excluding an analysis of the error due to calibration and lunar reflectance model for this instrument.

SCILLA was also the opportunity to test several lunar reflectance models for the Cimel instruments (LIME and RIMO models).

In the two last years of HARMONIA, we plan to look at the campaign dataset in detail using the grant opportunities of the COST action (Virtual Mobilities, Short Term Scientific Mission). As well for the purely photometry part, as for the synergy columnar (photometers, AOD) and profiling (balloon carried radiosonde COBALD, Lidar, Photometers).

3.3 Impact of air mass, Rayleigh scattering and trace gas absorption on AOD and aerosol properties retrievals in sun photometry

Sources/Contributors: Assessment of NO_2 contribution to aerosol optical depth measurements: Akriti Masoom, Theano Drosoglou, Stelios Kazadzis (Masoom et al. 2024b, Drosoglou et al. 2023), Lionel Doppler

AOD is calculated from direct-sun measurements by sun photometers (Cimel sun photometers in the case of AERONET), using the Beer-Bouguer-Lambert law (Eq. 3.1) that presents the atmospheric attenuation of radiation as

$$I(\lambda) = I_0(\lambda).\, e^{-(m_{Ray}\tau_{Ray}+m_{aer}\tau_{aer}+m_{O_3}\tau_{O_3}+m_{NO_2}\tau_{NO_2}+m_{CO_2}\tau_{CO_2}+m_{CH_4}\tau_{CH_4}+m_{H_2O}\tau_{H_2O})} \quad 3.1$$

where $I(\lambda)$ and $I_0(\lambda)$ represent the radiation intensity at the surface and top of the atmosphere (ToA), respectively, at a specific wavelength. is the total optical depth, and m is the total optical air mass. Total optical depth is the aggregation of the optical-depth contributions from Rayleigh scattering by molecules (Ray), gaseous absorption by ozone (O_3), nitrogen dioxide (NO_2), carbon dioxide (CO_2), methane

(CH_4), and precipitable water vapour (H_2O). m_{Ray}, m_{O_3}, m_{NO_2}, m_{CO_2}, m_{CH_4}, and m_{H_2O} represent their respective optical air masses, and maer is the aerosol optical air mass. The optical air masses are a function of sun elevation. AOD (aer) is calculated from total optical depth ($\boldsymbol{\tau}$) by subtracting the optical-depth contributions from Rayleigh scattering by molecules, gaseous absorption, and/or precipitable water vapour, depending on the wavelength.

Masoom et al. 2024b assessed the impact of NO_2 on AOD. The contribution of NO_2 absorption to AOD and the NO_2 optical-depth estimations (Eq. 3.2) (Cuevas et al., 2019), calculated as

$$\tau_{NO_2}(\lambda) = \frac{\sigma_{NO_2}(\lambda)}{1000} . \frac{m_{NO_2}}{m_a} . NO_2 \qquad 3.2$$

where NO_2 is the NO_2 absorption coefficient at wavelength (λ) obtained from Gueymard (1995), and the expression for m_{NO_2} is obtained from Gueymard (1995), while ma is the optical air mass, and NO_2 VCD is in Dobson units. The NO_2 absorption contribution to the NO_2 optical depth is directly proportional to the NO_2 VCD at a specific wavelength and sun elevation. The bias in AOD (refer to Eq. 5 in Masoom et al. 2024b) affecting the AERONET AOD calculation at a specific wavelength is produced by the simplified assumption of OMIc NO_2, and the associated optical depth (which is linear to the NO_2 concentration for an instrument at a specific wavelength and solar elevation; Eq. 3.2) was evaluated after exploiting the “real” value of columnar NO_2 from the co-located PGN instrumentation (refer to Eq. 4 in Masoom et al. 2024b).

From the findings of Masoom et al. 2024b, it was found that AOD bias was the most affected at 380 nm by NO_2 differences, followed by 440, 340, and 500 nm, respectively. AERONET AOD was found to be overestimated in half of the cases, while also underestimated in other cases as an impact of the NO_2 difference from “real” (PGN NO_2) values (Fig. 3.13). Overestimations or underestimations are relatively low. About one-third of these stations showed a mean difference in NO_2 and AOD (at 380 and 440 nm) above 0.5×10^{-4} mol m^{-2} and 0.002, respectively, which can be considered a systematic contribution to the uncertainties in the AOD measurements that are reported to be of the order of 0.01. However, under extreme NO_2 loading scenarios (i.e., 10 % highest differences) at highly urbanized/industrialized locations, even higher AOD differences were observed that were at the limit of or higher than

the reported 0.01 uncertainty in the AOD measurement. PGN NO_2-based sensitivity analysis of AOD difference suggested that for PGN NO_2 varying between 2×10^{-4} and 8×10^{-4} mol m^{-2}, the median AOD differences were found to rise above 0.01 (even above 0.02) with the increase in NO_2 threshold (i.e., the lower limit from 2×10^{-4} to 8×10^{-4} mol m^{-2}). The AOD-derivative product, AE, was also affected by the NO_2 correction (discrepancies between the AERONET OMI climatological representation of NO_2 values and the real PGN NO_2 measurements) on the spectral AOD.

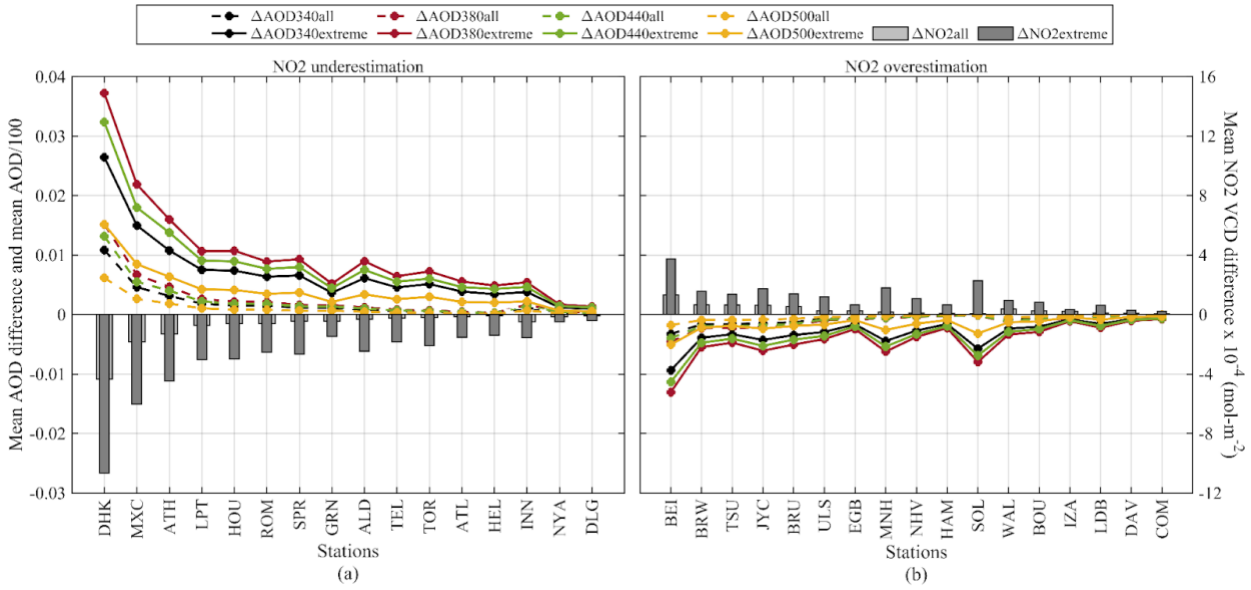

Figure 3.13: NO_2 vertical column density (VCD) in mol m^{-2} and AOD differences at 340, 380, 440, and 500 nm for all stations with NO_2 (a) underestimation and (b) overestimation. The NO_2 differences are calculated as OMIc–PGN, and the corresponding AOD differences are calculated as original AERONET AOD minus PGN-corrected AOD. X-axis contains the station name codes whose details are provided in Annex Table T2. (Figure credit: Masoom et al., 2024b)

Another study by Drosoglou et al., 2023 evaluated the NO_2 absorption effect in aerosol columnar properties, namely AOD, AE, and single scattering albedo (SSA), derived from sun–sky radiometers in addition to the possible retrieval algorithm improvements by using more accurate characterization of NO_2 optical depth from co-located or satellite-based real-time measurements. A multiannual (2017–2022) records of AOD, AE, and SSA collected by sun photometers at an urban and a suburban site in the Rome area (Italy) in the framework of both the Aerosol Robotic Network (AERONET) and SKYNET networks was used. The uncertainties introduced in the aerosol retrievals by the NO_2 absorption are investigated using high-

frequency observations of total NO_2 derived from co-located Pandora spectroradiometer systems in addition to spaceborne NO_2 products from the Tropospheric Monitoring Instrument (TROPOMI). For both AERONET and SKYNET, the standard network products were found to systematically overestimate AOD and AE. The average AOD bias found for Rome is relatively low for AERONET (~0.002 at 440 nm and ~0.003 at 380 nm) compared to the retrieval uncertainties but quite a bit higher for SKYNET (~0.007) (Fig. 3.14).

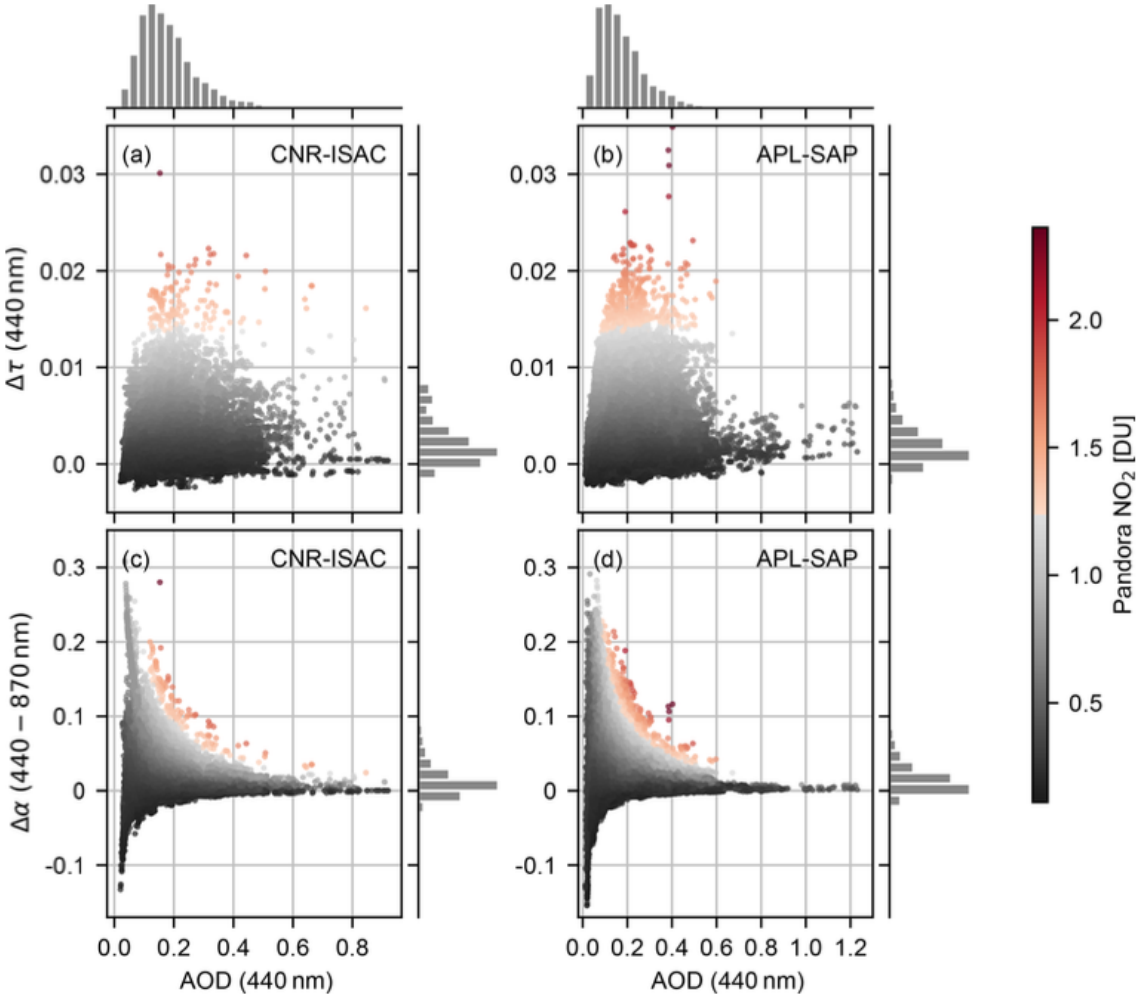

Figure 3.14: Differences in the modified AERONET AOD at 440 nm (a, b) and AE at 440–870 nm (c, d) over two stations (CNR-ISAC and APL-SAP) of Rome, Italy from the standard products illustrated with respect to the standard AERONET AOD measurements at 440 nm and the actual NO_2 observed by Pandora (color scale). (Figure credit: Drosoglou et al., 2023)

An average AE bias was estimated to be ~0.02 and~0.05 for AERONET and SKYNET, respectively. In general, the correction seems to be low for areas with low columnar

NO_2 concentrations, but it is still useful for low AODs (<0.3), where the majority of observations are found, especially under high NO_2 pollution events. For the cases of relatively high NO_2 levels (>0.7 DU), the mean AOD bias was found within the range 0.009–0.012 for AERONET, depending on wavelength and location, and about 0.018 for SKYNET. In addition, the comparisons of the NO_2-modified ground-based AOD data with satellite retrievals from the Deep Blue (DB) algorithm of the NASA Moderate Resolution Imaging Spectroradiometer (MODIS) resulted in a slight improvement in the agreement of about 0.003 and 0.006 for AERONET and SKYNET, respectively. Finally, the uncertainty in assumptions on NO_2 seems to have a non-negligible impact on the retrieved values of SSA at 440 nm leading to an average positive bias of about 0.02 (2 %) in both locations for high NO_2 loadings (>0.7 DU).

Table 3.7: Summary of the influence of absolute mean NO_2 differences on the absolute mean range of aerosol properties retrieval

Impact on aerosol properties	Low NO_2 difference (< 0.5 x10^{-4} mol m^{-2})	Medium NO_2 difference (0.5 to 1 x10^{-4} mol m^{-2})	High NO_2 difference (> 1 x10^{-4} mol m^{-2})
From analysis of 33 worldwide stations (Masoom et al. 2024b)			
AOD 340 nm	0.000-0.001	0.001-0.002	0.003-0.011
AOD 380 nm	0.000-0.002	0.002-0.003	0.005-0.015
AOD 440 nm	0.000-0.001	0.002-0.002	0.004-0.013
AOD 500 nm	0.000-0.001	0.001-0.001	0.002-0.006
AE 440-870 nm	0.02-0.38	0.06-0.15	0.04-0.23
AE 340-440 nm	0.01-0.14	0.05-0.12	0.03-0.21

Table 3.7 summarizes the order of magnitude obtained in the different studies presented in this section about the impact of NO_2 absorption of radiation on the optical depth at different wavelengths and therefore on the AOD and AE retrievals. We notice, that in the statistical analysis of PFR versus Cimel on the Lindenberg-Dataset (Section 3.1.2.1, “Interception” parameter of Figures 3.2 and AP-3.3), the statistical biases of AOD_PFR - AOD-Cimel is shifted between +0.002 and +0.004

depending on the year from the 500 nm channel (impacted by NO_2) compared to the bias of the channel 865 nm (not impacted by NO_2). That means that for 500 nm (impacted by NO_2), PFR overestimates more the AOD in comparison to Cimel from +0.002 to +0.004 than for 865 nm (no NO_2 impact). The explanation can be that the GAW-PFR algorithm used in the Lindenberg-Dataset does not consider any NO_2 correction. Table 3.7 indicates that depending on the NO_2 amount, we can have 0.001 to 0.004 (medium to high NO_2 amount) overestimation of the AOD at 500 nm if we do not consider the NO_2 gas absorption. Therefore, this could be an explanation of the very low positive bias between AOD_PFR and AOD_Cimel in Lindenberg. Further studies could focus on low and high NO_2 events in order to investigate if this hypothesis is valid.

4. AOD in the Ultraviolet (UV) - High spectral resolved AOD retrievals

4.1 AOD in the Ultraviolet: Brewer and BTS instruments

The retrieval of AOD is a challenging issue in the ultraviolet (UV) part of the electromagnetic spectrum because of the low direct sun radiation passing through the stratosphere in this spectral band (low signal/noise ratio of the radiation measurements), and also because of the contamination of the optical depth by the ozone absorption of radiation: The ozone absorption spectrum in UV especially in UVB leads to a high and spectral variable ozone optical depth. Therefore, the retrieval of aerosol optical depth using a filter radiometer measurement (as the photometers do) requires in this spectral range filters with a very narrow spectral response function, which reduces again the signal/noise ratio. For these reasons, in the UVB (280 - 315 nm) in which the ozone optical depth spectrum is high and variable, photometers are not appropriate instruments to retrieve the AOD. The difficulties of operating and calibrating a UV Photometer are well documented in Carlund et al., 2017 who report about the UV-PFR (UV Precision Filter Radiometer), a PMOD/WRC PFR, a stable and robust instrument for AOD retrievals at four UV wavelength: 305, 311, 318 and 332 nm.

Because of these difficulties, for the operational networks, the lowest photometer wavelength to retrieve AOD is 340 nm for day measurements (sunphotometers) and over 360 nm for night measurements (lunar photometer). AOD retrieval in the UVB requests instruments that are specially developed for radiation measurements in this spectral band: UV spectrometers (monochromators) or UV spectroradiometers (array spectrometers). Two main instruments are currently operational in the international community: The UV spectrometer (monochromator) Brewer and the spectroradiometer (Array Spectrometer) UV-BTS as discussed below. Both instruments are originally designed for UV spectral measurements and for Total Ozone Column (TOC) retrievals.

Brewer UV spectrometer

The Brewer UV spectrometer was designed in the sixties and started to be operational in the seventies. Brewers have been manufactured by IOS (International Ozone Service Inc., Toronto, Canada) until the 2010ies then by Kipp & Zonen (Delft, The Netherlands).

The original idea was to have an automatic instrument that supplies the manual operated Dobson instruments for TOC measurements, but in addition to it, operates UV spectra monitoring in UVB. Therefore, the instrument was designed with a UV Spectrometer (monochromator), in the range 285 to 325 nm, with a high spectral resolution of 0.5 nm. The instrument has two optical entrances: The first entrance is a dome for the “global” modus, allowing UV spectral measurements of the GHI (Global Horizontal Irradiance). From these measurements, we can compute the UVB and UV-Index reaching the ground. The second optical entrance is a periscope that is orientable in zenith in order to catch the direction of the sun. The periscope is put behind a quartz “direct sun window”. The whole instrument is set on an azimuth tracker; therefore, the periscope is always pointing the sun direction when the instrument is in “direct sun” modus. The aim of the direct sun modus is the monitoring of Total Ozone Column (TOC). For this purpose, the brewer has six slits positioned at the output of the monochromator in order to select six spectral channels in the UVB with very narrow triangular spectral response functions. These six spectral channels are at 303.2, 306.3, 310.1, 313.5, 316.8 and 320.14 nm. Some of these bands are positioned at high ozone absorption some others at narrow ozone

absorption. Some wavelengths are affected by SO2 absorption and some not. A good combination of the measurements at these six wavelengths ("Brewer equation") allows the retrieval of Dobson Unit values of Total Ozone Column (TOC) and Total SO2 Column. The sensitivity of the Brewer, and the precise knowledge of the gas absorption at these wavelengths allow to use the Brewer measurements at these slits for the retrieval of the AOD at the five channels 306.3, 310.1, 313.5, 316.8, and 320.14 nm. The exact methods of AOD retrieval at these wavelengths out of the Brewer TOC measurements is explained in detail in Section 4.1.1.

UV-BTS (BTS2048-UV-s)

The UV-BTS is the Ultraviolet version of the BTS BiTec Sensor Spektralradiometer, an array spectroradiometer manufactured by the German company Gigahertz-Optik (GHO). It is based on the Czerny–Turner spectrometer design. The spectrometer uses a back-thinned Hamamatsu CCD detector with 2048 pixels and an electronic shutter integrated in a compact optical bench with 16 bits analogue–digital converter (ADC) resolution. Integration times from 2 µs up to 60 s provide a high dynamic range of the instrument in the spectral range from 200 to 430 nm. The detector unit is complemented with a silicon carbide (SiC) photodiode to enable fast time-resolved radiometric measurements (Zuber et al. 2018). Each 2048 spectral channel has an almost gaussian spectral response, with a bandwidth (Full Width at Half Maximum) of 0.6 nm for channels below 360 nm. The instrument was designed with UV spectral measurements in the UV. If mounted on a sun tracker, and equipped with 3 degrees open collimator, the instrument can be used for spectral DNI (Direct Normal Incident) measurements in the UV, and for Total Ozone Column (TOC) and AOD measurements (Zuber et al. 2021). The method of how the BTS (UV-BTS and VIS, NIR BTS) realized the AOD inversion is detailed in Section 4.2.1., and the applications of AOD with the BTS are listed in Section 4.1.2.

4.1.1 The Brewer AOD retrieval method

The main approach is the one developed in the European network EUBREWNET (European Brewer Network, Rimmer et al. 2018) in the COST Action ES1207, "EuBrewNet – A European Brewer Network", that was awarded to allow the harmonisation and coordination of Brewer ozone spectrophotometer measurements of TOC (Total Ozone Column), spectral UV and AOD in the Ultraviolet

(UV). The Brewer AOD retrieval method of EUBREWNET is explained in detail in Lopez-Solano et al. 2018. The EUBREWNET method is based on the inversion of Beer-Bouguer-Lambert equation and therefore the AOD Brewer calibration proposed by EUBREWNET method and explained in Lopez-Solano et al. 2018 is the Langley Plot method. The Brewer EUBREWNET Brewer-AOD method has been validated theoretically with an uncertainty analysis, intercomparison Brewer-Brewer and comparisons to the UV-PFR (UV Precision Filter Radiometer: Carlund et al. 2017). In Section 4.1.1.1 we explain the genesis of the AOD retrieval in UV, and the first methods experimented. In Section 4.1.1.2, we present an alternative even if very similar method to EUBREWNET one: The IOS (International Ozone Service) method.

Brewer AOD retrieval in the UV is operational in most of the sites equipped by brewers worldwide, using mostly the EUBREWENT method or the IOS method. Most of the Brewer stations worldwide, especially the European stations are networked by EUBREWNET (European Brewer Network): https://eubrewnet.aemet.es/. There, it is possible to download the AOD products of most of the registered Brewer stations. We detail the application of Brewer AOD retrieval for two stations: PopPoprad-Gánovce (SHMÚ, Slovakia), with the COST-HARMONIA ITC grant report of Peter Hrabčák in Section 4.1.1.3 and and in Uccle in Belgium in Section 4.1.14.

4.1.1.1 First approaches on AOD measurements in the UVB region

Contributor: Stelios Kazadzis, Ilias Fountoulakis.

In the UVB region there are very few instruments that have provided aerosol parameter (AOD or Single Scattering Albedo) measurements, primarily the Brewer spectrophotometer. Measurements in the late 90s dealt with two different approaches:

The calibration method

For this part there were different approaches e.g., Savastiouk (1995), Bais et al. (1997), Meleti et al. (2000) and Kazadzis et al. (2005) which have used absolute direct sun measurements in the 290-365 nm range and satellite based extraterrestrial spectra in order to calculate the AOD from the Beer-Bouguer-Lambert equation. The absolute measurements for direct sun have been retrieved through the transfer of calibration of the global (diffuser) measurement to the direct through simultaneous

global, direct, diffuse measurements using a shading disk in a low aerosol (e.g., Izaña, Spain) environment. Gröbner et al. (2002) analyzed 11 years (1991-2002) of measurements calibrating the instrument with two methods: The classic Langley calibration method where absolute solar irradiance values are not needed, and the calibration factor is defined by the zero air mass extrapolation of the Brewer signal. Additionally, Kazadzis et al. (2005) used a lamp as a calibration source to calibrate the direct sun measurements of the instrument. Gröbner et al. (2001) and (2017) have calculated and improved extraterrestrial solar spectrum to be used for AOD calculations both for UV and visible wavelengths.

Wavelength range set up

All the above publications have been using the Brewer instrument with two different setups. Either measuring a full spectrum (290-365 nm for the double Brewer monochromator), or using the standard ozone measuring procedure of the Brewer spectrophotometer that records raw photon counts of the photomultiplier at the five nominal wavelengths 306.3, 310.1, 313.5, 316.8, and 320.0 nm using a blocking slit mask, which opens successively one of five exit slits (Gröbner et al., 2002, 2004; Marenco et al., 2002; Meleti and Cappellani, 2000; Cheymol and De Backer, 2003). The first one having the advantage of the extended range but the disadvantage of the measurement duration (7 minutes) and vice versa. A number of early studies have derived UV AOD aerosol time series (Gröbner et al., 2002, Kazadzis et al., 2007 and others). A second instrument measuring AOD at the UV range was the multi-filter rotating shadow-band radiometer (UVMFR) measuring at 368 and 332 nm (Kazadzis et al., 2016). The method here was also the Langley calibration. Various studies including Bais et al. (2005), Kazadzis et al. (2016), Fountoulakis et al. (2019), Meleti., (2009) have investigated other factors that can be retrieved (e.g. SSA) and are affecting solar UV radiation.

4.1.1.2 The IOS (International Ozone Services Inc.) Brewer-AOD method

Contributor: Volodya Savastiouk

Savastiouk, (1995) introduced new data products for the Brewer, among them an algorithm for calculating the AOD using the direct-sun Brewer data. Later, it was refined and eventually incorporated into the Brewer operating software for real-time calculations (Savastiouk 2004; Savastiouk and McElroy 2004 (a,b), 2005;

Savastiouk 2006). The algorithm is based on the Beer-Bouguer-Lambert Law taking into account ozone, sulfur dioxide and Rayleigh extinction in the 300-320 nm region and includes determination of the neutral density filters' attenuation using either the internal halogen lamp or a special variation of Langley analysis where the linear fit is done with a constant slope, but multiple intercepts, one for each filter in use (Fig. 4.1).

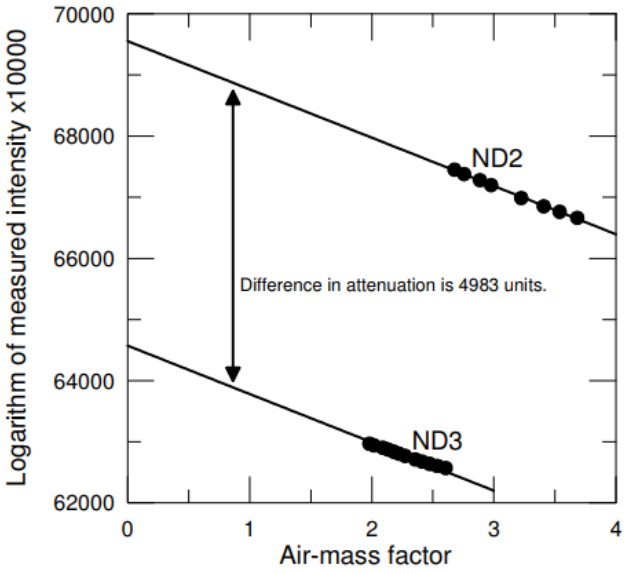

Figure 4.1: Langley Plot calibration for two Brewers Channels (Brewer AOD retrieval following IOS Method)

The daily statistics for AOD is based on the minimum, rather than the average, AOD value, which is more representative of the AOD load. This algorithm has no cloud screening and considers clouds, being droplets of water, a type of aerosol. The algorithm has been implemented in popular Brewer data processing software O3Brewer (M.Stanek, www.o3soft.eu) and BFilePro (V. Savastiouk, software.drvolodya.ca). International Ozone Services Inc. (Toronto, Canada) has been providing AOD transfer calibration using a traveling standard as part of Brewer calibration services for more than 150 instruments since 1996.

4.1.1.3 AOD measurements with Brewers at Poprad-Gánovce (SHMÚ, Slovakia)

Contributor/Source: Peter Hrabčák, COST-HARMONIA ITC (Inclusive Target Countries) Conference grant to attend QOS (Quadrennial Ozone Symposium) 2024 conference in Boulder (CO, USA) on AOD retrievals with Brewers, WEBLINK to the Poster.

A 30-year series of measurements of total atmospheric ozone in Slovakia beginning from August 1993 till 2023 at the Poprad-Gánovce station with the Brewer ozone spectrophotometer are discussed in this section with the aim to present the calculated values of total atmospheric ozone and AOD from Brewer measurements. Also presented are trends of two key parameters that affect the amount of solar UV radiation reaching the Earth's surface. The obtained results fit quite well into the well-known mosaic of recent years atmospheric development in the wider regional space of Eastern Europe. The total ozone trend in this region is determined by both atmospheric dynamic and ozone-depleting substances (ODSs) related effects. An acceleration of the Brewer-Dobson circulation and other atmospheric changes due to increasing amounts of greenhouse gases are probably beginning to manifest itself, but differently in individual months of the year. Social and industrial changes in the region have caused a significant decrease in anthropogenic air pollution. As a result, there has been a gradual decline in AOD in recent decades.

The Brewer located in Aerological and Solar Radiation Center Poprad-Gánovce of the Slovak Hydrometeorological Institute, has coordinates as 49.03°N, 20.32°E and an altitude of 709 m above sea level. The site is located in the Podtatranská basin, which is part of a larger geomorphological unit called the Carpathians. There are mountain units of different heights around. Gerlachovský štít (2654 m above sea level), the highest peak of the Carpathians, is located only 20 km from the station. Among the more important local aerosol sources are the products of burning solid fuel, mainly wood in the surrounding villages and agriculture. In the presence of a larger pressure gradient, the location is relatively windy. The prevailing wind directions are west, north and south-east. The proximity of the city of Poprad (approx. 1.5 km) with approximately 50 000 inhabitants and various industrial activities also plays a role. In spite of the proximity of the mentioned city, the area can generally be deemed rural with respect to the anthropogenic impact.

The Brewer ozone spectrophotometer #97, model MKIV (single monochromator) has been working at the Poprad-Gánovce station since August 18, 1993. It focuses mainly on the measurement of total atmospheric ozone and the spectrum of global solar UV radiation. Measurements of direct sunlight for wavelengths of 306.3, 310, 313.5, 316.8 and 320 nm were also used to determine AOD. Since the beginning of measurements, the device has undergone regular 2-year calibration and daily tests

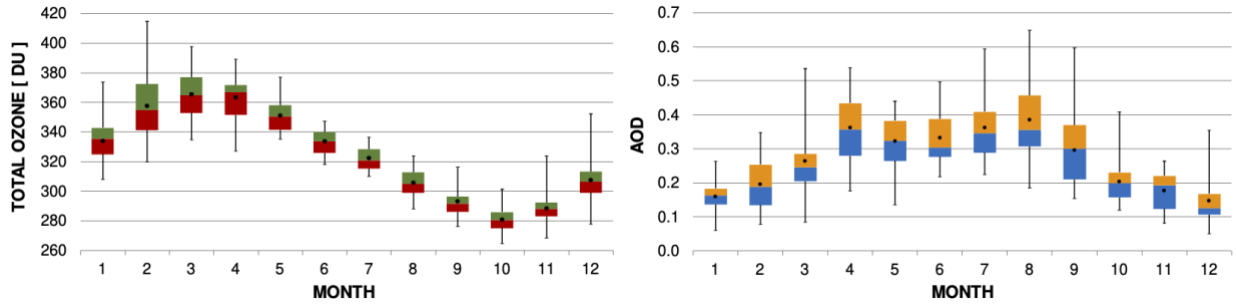

(a) (b)

Figure 4.2 Long-term monthly mean of total ozone and AOD at 320 nm for Poprad-Gánovce obtained over the 30-year period (1994 - 2023).

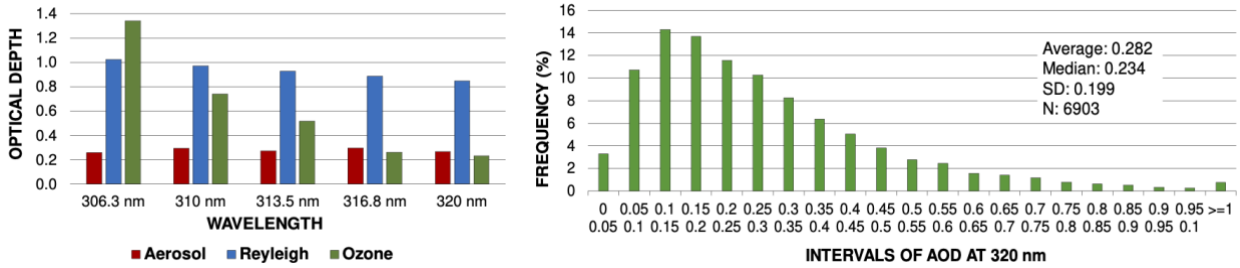

(a) (b)

Figure 4.3: 30-year (1994-2023) average of optical depth values at five wavelengths for aerosol, Rayleigh scattering and total ozone.

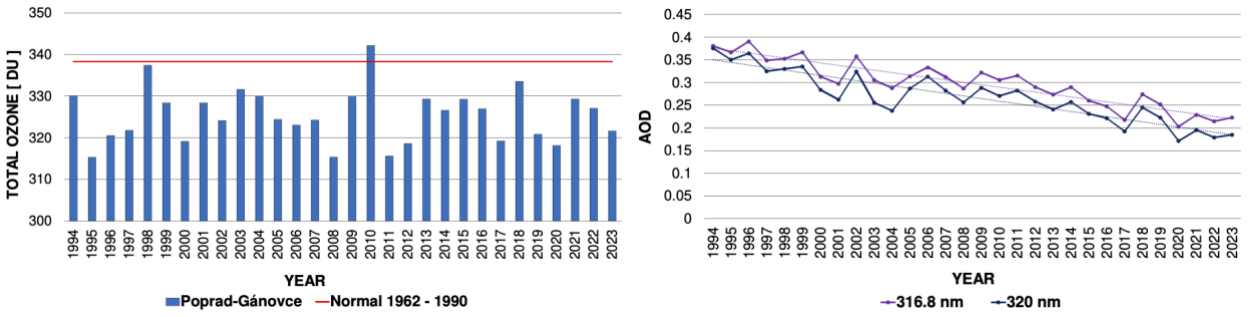

(a) (b)

Figure 4.4: Long-term annual averages of total ozone for Poprad-Gánovce obtained over the 30-year period (1994 - 2023) compared with the normal (1962-1990) measured at the nearby Hradec-Králové station.

using internal lamps. The instrument is calibrated by International Ozone Services Inc. according to the global reference group (Brewer Triad), maintained at Environment Canada, through a travel reference instrument. Measurements can be considered as homogeneous from a technical point of view. Only Direct Sun (DS) measurements were used for total ozone analysis. AOD was determined by using extraterrestrial constants (changed after each calibration) obtained by the Langley

plot method. The calculation takes into account the corrections for diffuse radiation, the stray-light effect and polarization. The methodology follows the work of Hrabčák (2018), but it is improved.

Figure 4.2 illustrate the long-term monthly characteristics of total ozone and AOD at 320 nm for Poprad-Gánovce obtained over the 30-year period (1994 - 2023). Solid points represent mean values, the border between the boxes represents the median, the lower and upper limits of the boxes portray the first (25%) and the third (75%) quartiles respectively and the lower and upper whiskers account for minimum and maximum respectively. Figure 4.3 shows the 30-year averages (1994 - 2023) of AOD values at five wavelengths for aerosol, Rayleigh scattering and total ozone and the relative occurrence of daily averages of AOD at 320 nm for Poprad-Gánovce in the 30-year period (1994 - 2023). Figure 4.4 shows the annual averages of total ozone for Poprad-Gánovce for the 30-year period (1994 - 2023) as compared with the normal (1962 - 1990) measured at the nearby Hradec-Králové station and the comparison of annual averages of AOD at the two longest wavelengths and their linear trend for Poprad-Gánovce for the 30-year period (1994 - 2023).

The long-term 30-year average (1994 - 2023) of total ozone reached the value of 325.4 DU, which is 3.8% less than the normal value of 338.3 DU measured at the nearby Hradec-Králové station. The lowest annual average was measured in 1995 at 315.3 DU (-6.8% compared to normal). The highest annual average was measured in 2010 at 342.2 DU (+1.1% compared to normal). The linear trend for the period 1994 - 2023 is statistically insignificant and reached the value of -0.4 ± 4 (SD) DU. In the case of months, the most interesting trends were observed in January (13.3 ± 9.8 DU) and August (-10.3 ± 5.3 DU). The historically lowest daily average was measured on 01 January 1998 at 202.6 DU and the highest on February 24, 1999 at 509 DU. The long-term 30-year average of AOD acquired the following values: 0.257 at 306.3 nm, 0.293 at 310 nm, 0.273 at 313.5 nm, 0.298 at 316.8 nm and 0.267 at 320 nm. AE takes on a negative value for some pairs of wavelengths. The relative occurrence of daily averages of AOD at 320 nm showed a left-side skewed distribution and the most frequent occurrence of values in the range from 0.1 to 0.15. The linear trend for the period from 1994 to 2023 is statistically significant for all wavelengths and reached the following values: -0.17 ± 0.1 at 306.3 nm, -0.15 ± 0.1 at 310 nm, -0.17 ± 0.1 at 313.5 nm, -0.16 ± 0.1 at 316.8 nm and -0.17 ± 0.1 at 320 nm. Decreasing trends in AOD were

observed for all wavelengths and months of the year. It is noteworthy that the lowest annual average of AOD for all 5 wavelengths was measured in 2020, during the first year of COVID-19 pandemic.

4.1.1.4 AOD measurements with Brewers at Uccle, Belgium

Contributor: Alexander Mangold

Uccle is a residential municipality in the South of the Brussels Region, around 100 km from the North Sea shore. The Royal Meteorological Institute (RMI) of Belgium operates two Brewer ozone spectrophotometers (#016 since 1984 and #178 since 2002) at its site (50.8° N, 4.3° E, 100 m a.s.l.). Brewer#016 is a single monochromator Mark II model (spectral range 290 nm to 325 nm) and Brewer#178 is a double monochromator Mark III (spectral range 287.5 nm to 363 nm). The instruments are integrated in the European network EUBREWNET, in the World Ozone and Ultraviolet Radiation Data Centre (WOUDC) and in the Network for the Detection of Atmospheric Composition Change (NDACC, Brewer016). The instruments are calibrated against a reference instrument each second year.

For the retrieval of AOD from Brewer observations, the Langley-Plot method is applied. The method and algorithms used are described in Cheymol and De Backer (2003), De Bock et al. (2010) and De Bock et al (2014). Using the direct sun observations, the AOD is derived for 306.3, 310.1, 313.5, 316.8 and 320.1 nm, for both Brewers #016 and #178. In addition to the standard observation routines, an additional routine was developed in 2006 in order to be able to determine the AOD at 340 nm with the double monochromator Brewer #178. More precisely, the sun scan routine was adapted to perform scans between 335 nm and 345 nm. The measuring wavelength step of this sun scan routine is 0.5 nm, and one scan has a duration of 21 s per step. The obtained spectral data are convoluted with the band pass function of the Cimel sunphotometer filter (FullWidth at Half Maximum of the filter is 4.756 nm) in order to enable the comparison with the Aeronet 340 nm AOD product.

The cloud-screening algorithm used (for both direct sun and sun scan observations, described in De Bock et al., 2010, 2014), makes use of sunshine duration data from four pyrheliometers at Uccle and is also based on the assumption that the variability of the AOD in the course of one day is either lower than 10% or lower than 0.08 AOD

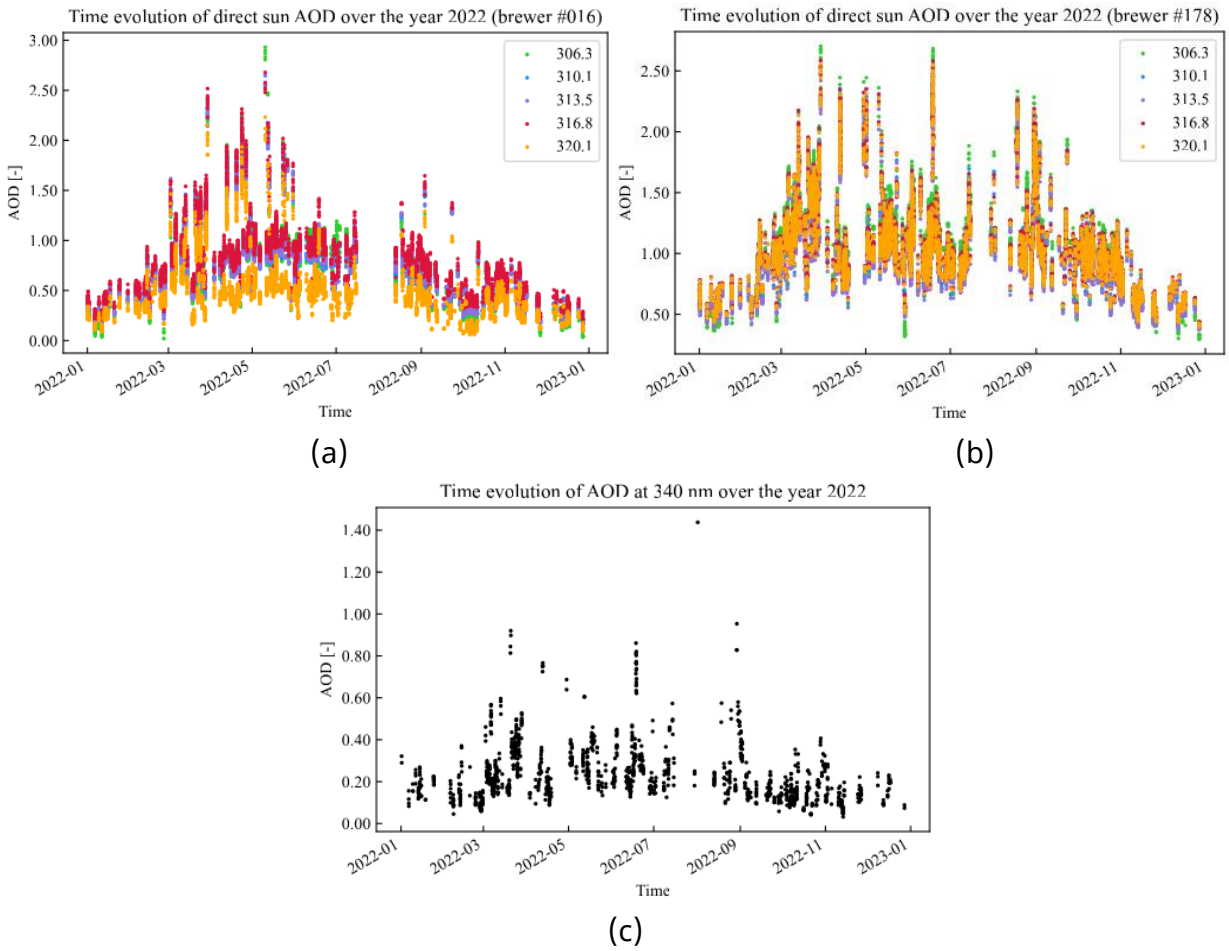

Figure 4.5: AOD derived from direct sun observations of (a) Brewer #016 and (b) Brewer #178 for the year 2022 and (c) AOD derived from sun scan observations of Brewer #178 for year 2022

units, which is the maximum uncertainty of the AOD retrieval algorithm. First, it is determined whether the individual AOD measurements were taken within a 10 min interval of continuous sunshine. The measurements for which this is not the case are removed, after which more than two individual measurements per day must remain in order to continue. For each day, the maximum deviation to the median value is then determined. If this value is less than 0.08, we accept all measurements for that day. However, if the maximum deviation exceeds 0.08, the relative standard deviation for that day is calculated. In case this value is less than 10 %, which would guarantee a given stability within the diurnal pattern of AOD, all the AOD values for that day are accepted. In the other case, the AOD measurement with the largest contribution to the standard deviation is removed, as this measurement is most likely influenced by clouds. The median value will then be recomputed, and the

previous steps are repeated. Days with two or less individual AOD measurements are excluded from the results.

The cloud-screened AOD from both direct sun and sun scan Brewer measurements, were compared to quasi-simultaneous and colocated Cimel level 2.0 quality-assured values, with a maximum time difference of 3 min (De Bock et al., 2014). The Cimel sun photometer, which belongs to the Belgium Institute of Space Aeronomy, is located approximately 100 m from the Brewer instruments. For the period of comparison (2006–2013), the cloud-screened Brewer AOD values agreed very well, with correlation coefficients of 0.97 (Brewer #016 for 320.1 nm), 0.98 (Brewer #178, 340 nm) and 0.99 (Brewer #178, 320.1 nm), and slopes of 1.004, 0.993, 1.007, respectively, and intercepts of -0.067, 0.073 and 0.017, respectively.

Figure 4.5 shows the AOD for the year 2022, from direct sun observations (Brewer #016 and Brewer #178) and from sun scan observations for Brewer #178. A detailed comparison between the Brewers and with the collocated Aeronet Cimel is in work. A recent update on the Uccle time series of Brewer ozone and UV radiation can be found in Lorenz et al., 2024.

4.1.2 Method to retrieve AOD with UV-BTS

Contributor: Ralf Zuber

AOD retrieval technique is the same in the UV spectral region as in other wavelength ranges and is explained in Section 4.2.1. Of course, in the UV especially the correction of ozone absorption is very important and a significant contribution to the measurement uncertainty.

The stations operating at least a UV-BTS (some full spectral range to IR) are (list may not complete):

- Meteorological Observatory Hohenpeißenberg, Deutscher Wetterdienst (MOH, DWD), Hohenpeißenberg, Germany (UV-BTS only)
- Meteorological Observatory Lindenberg -Richard-Aßmann-Observatory, Deutscher Wetterdienst (MOL-RAO, DWD), Lindenberg (Tauche), Germany (UV-BTS only)

- PMOD/WRC, Davos, Switzerland: Many instruments covering full spectrum from UV to IR, until other the UV-BTS
- School of Earth and Environmental Sciences, University of Manchester, Manchester, UK (UV-BTS only)
- IARC, AEMET (Izaña), Teneriffe, Spain (UV-BTS only)
- Centre for Energy, Environmental and Technological Research (CIEMAT), Madrid, Spain: many instruments covering full spectrum from UV to IR, until other the UV-BTS
- Institute of Biomedical Physics, Medical University Innsbruck, Innsbruck, Austria (UV-BTS only)
- Bundesamt für Strahlenschutz (BfS), Neuherberg by Munich, Germany (UV-BTS only)
- Bundesanstalt für Arbeitsschutz und Arbeitsmedizin (BAuA), Dortmund, Germany (UV-BTS only)
- Melpitz Research Station, Leibniz-Institut für Troposphärenforschung (TROPOS), Melpitz, Germany (UV-BTS only)
- Environmental research station, Schneefernerhaus, Zugspitze, Germany (UV-BTS only, operated by Bundesamt für Strahlenschutz).

4.2 High spectral AOD: Review of existing methods and instruments

With the development of the spectroradiometer from type array spectrometer in the AOD photometer bands (UVA, VIS, NIR), in the former decade (2010ies), we have instruments that provide the direct sun spectral irradiance at a high spectral resolution (< 1 nm), for many channels (1024 or 2048) in the 300-1000 nm spectral band, with high precision, low uncertainties and traceability to the SI (Système international d'unités).

This offers the opportunity to apply these measured values in the Beer-Bouguer-Lambert equation and use the tabulated values of solar spectral irradiance at the

entrance of the atmosphere as "I_0" of the Beer-Bouguer-Lambert equation. Therefore, it is theoretically possible to extract the total optical depth for every channel of the array spectrometer and depending on the knowledge of gas columnar amount (Ozone, NO_2, O_2, water vapour), to retrieve the AOD at high spectral resolution in the whole 300-1000 nm band. We present the techniques as they are operated in many HARMONIA stations for the spectroradiometers BTS (manufactured by Gigahertz-Optik) in Section 4.2.1, EKO MS-711 (manufactured by EKO) in Section 4.2.2 and PSR (manufactured by PMOD-WRC) in Section 4.2.3.

Table 4.1. Stations of HARMONIA community operating AOD retrieval at high spectral resolution using Array spectroradiometer in the 300-1000 nm spectral band.

Station place	Operated by	Instrument(s)
Actinometric Station of National Observatory of Athens (ASNOA), Athens, Greece	NOA (National Observatory of Athens)	PSR
Institut für Meteorologie, Freie Universität Berlin (Ifm, FUB), Berlin, Germany	MOL-RAO, DWD	PSR
Physikalisch-Meteorologisches Observatorium Davos and World Radiation Center (PMOD/WRC), Davos, Switzerland	PMOD/WRC	PSR, BTS
Izaña Atmospheric Research Center, Agencia Estatal de Meteorología (IARC, AEMET), Izaña, Tenerife, Spain	MOL-RAO, DWD	EKO
Meteorologisches Observatorium Lindenberg, Deutscher Wetterdienst (MOL-RAO, DWD), Lindenberg (Tauche), Germany	MOL-RAO, DWD	PSR
Centre for Energy, Environmental and Technological Research (CIEMAT), Madrid, Spain	CIEMAT	BTS
Laboratorio de Energía Solar (LES), Universidad de la República, Montevideo, Uruguay	LES	EKO

These instruments are already operational in many stations around the world and especially in Europe, many of them are part of the HARMONIA community (See Table 4.1). For some stations, we have already more than 10 years of AOD retrieved data.

In September 2022 an intercomparison campaign took place at Izaña Atmospheric Research Center (IARC) at Izaña (Tenerife, Spain) involving all these three instruments, and also QASUME, the spectrometer reference system of PMOD/WRC (Gröbner et al. 2017) with pre-calibration in laboratories. The array spectrometers have been validated in irradiance with comparison to QASUME, the AOD products of the array spectroradiometers have been cross-compared, and the AOD for the photometer channels have been compared to GAW-PFR (PFR) and AERONET (Cimel) products. Gröbner et al. 2023 summarises the activities and results of this campaign and is the most actual and most comprehensive reference paper for AOD retrieved from high spectral resolved direct sun normal irradiance (DNI) measurements with array spectroradiometers.

4.2.1 Method to retrieve AOD with BTS

Contributor/Source: Ralf Zuber, Gröbner et al. 2017, Zuber et al. 2018, 2021

The retrieval of atmospheric transmission and AOD from ground-based spectral direct solar irradiance measurements uses the Beer-Bouguer-Lambert law:

$$I_\lambda = I_{0,\lambda} R_{SE} e^{-\tau_\lambda m} \qquad 4.1$$

where I_λ represents the solar irradiance measured at wavelength λ, $I_{0,\lambda}$ the solar irradiance at the top of the atmosphere, RSE the sun–Earth distance normalized to 1 au, τ_λ the total optical depth, and m the air mass. The zero-air-mass extrapolation procedure as described in Gröbner et al. (2017) is used by performing a linear regression of the logarithm of the spectral solar irradiance measurements with respect to air mass to retrieve the spectral solar irradiance value at air mass 0, representing the ToA solar irradiance at wavelength λ. This procedure assumes that during the duration of these measurements, the atmospheric transmission τ_λ remains constant and that any remaining small atmospheric variations are uncorrelated and therefore random from one day to the next (Gröbner et al. 2023).

The spectral optical depth τ_λ is derived by rearranging Eq. 4.1 and expanding the optical depth τ:

$$\tau_a(\lambda) = \log(\frac{I_0(\lambda)}{I(\lambda)} - \sum_{i=1}^{N} \tau_i(\lambda) m_i)/m_a - \tau_R(p,\lambda) \quad 4.2$$

where τ_i represents the optical depths of the atmospheric trace gas i and mi the corresponding air mass and $\tau_R(p,\lambda)$ stands for the Rayleigh scattering term which depends on the atmospheric pressure p, with λ being the corresponding wavelength. The sun–Earth correction factor R_{SE} has been omitted for convenience.

For an accurate AOD retrieval, the influence of trace gas absorptions τ_i needs to be known, so usually, the AOD is retrieved only in the spectral regions where the uncertainty due to their influence is small, either because the absorption is negligible or because it can be corrected for. This is for example the case for atmospheric ozone, which needs to be subtracted in the short ultraviolet below 340 nm or in the Chappuis band between approximately 450 and 750 nm. The ozone absorption can be calculated using the ozone absorption cross sections from Serdyuchenko et al. (2014), the Rayleigh scattering is calculated using the formula by Bodhaine et al. (1999). This detailed description is from Gröbner et al. 2023 where additional details can be found, as for instance an intercomparison between different instruments.

4.2.2 Methods to retrieve AOD with Eko

Contributor/Source: África Baretto Velasco (until 4.2.2.5), Paola Russo Ganón (4.2.2.5), García-Cabrera et al. (until 4.2.2.5), AMT 2020, Russo et al., 2023 (4.2.2.5)

The EKO MS-711 spectroradiometer was factory calibrated by EKO Instruments, by making use of a calibrated transfer standard 1000 W quartz tungsten halogen coiled coil filament lamp that is traceable to the National Institute of Standards and Technology (NIST) standard (Yoon et al., 2000). The instrument's resultant uncertainty is ±17% for the UV range and < 5% for the VIS range. In November 2016, the EKO MS-711 participated in an intercomparison campaign of spectroradiometers at the National Oceanic and Atmospheric Administration (NOAA) Mauna Loa Observatory (MLO), Hawaii, USA (19.54º N, 155.58º W; 3397 m a.s.l.; Pó et al., 2018), where it was calibrated with the Langley method (Ångström, 1970; Shaw et al., 1973). In 2018 the instrument was deployed at the Physikalisch-Meteorologisches Observatorium Davos / World Radiation Center (PMOD/WRC) for its characteristic use of a tunable laser (Sengupta et al., 2019). Recently, between

April and September 2019, the EKO MS-711 was calibrated at the Izaña Atmospheric Observatory by using the Langley method in the 300–1100 nm spectral range. In this study we have used the calibration coefficients with the Langley plot method.

The Langley method used in the IZO Langley calibration is based on the Beer–Bouguer-Lambert law as presented in Eq. 4.3:

$$\mathrm{DNI}(\lambda) = \mathrm{DNI}_0(\lambda)\mathrm{e}^{-\tau(\lambda)\mathrm{m}} \quad 4.3$$

where $\mathrm{DNI}(\lambda)$ is the direct normal irradiance at wavelength (λ) measured by the instrument; DNI_0 is the top-of-atmosphere irradiance corrected for the Sun–Earth distance at wavelength (λ); m is air mass; and $\tau(\lambda)$ is the optical depth. This expression can be written in the UV–VIS range as presented in Eq. 4.4:

$$\tau(\lambda) = \tau_{\mathrm{R}}(\lambda) + \tau_{\mathrm{a}}(\lambda) + \tau_{\mathrm{NO_2}}(\lambda) + \tau_{\mathrm{H_2O}}(\lambda) + \tau_{\mathrm{O_2}}(\lambda) + \tau_{\mathrm{O_3}}(\lambda) \quad 4.4$$

where $\tau_{\mathrm{R}}(\lambda)$ is the Rayleigh optical depth (Hansen and Travis, 1974), due to the molecular scattering that depends on the station pressure and on the optical air mass (m_R) (Bodhaine et al., 1999); $\tau_{\mathrm{a}}(\lambda)$ is the AOD; and the rest of the terms are the absorption by atmospheric gases in the affected wave- lengths (Gueymard, 2001). These are defined in García-Cabrera et al. (2020).

The Langley plot determines $\mathrm{DNI}_0(\lambda)$ (which allows us to derive calibration constant) from a linear extrapolation of $\mathrm{DNI}(\lambda)$ measurements to zero air mass, which is corrected to mean Sun–Earth distance, and plotted on a logarithmic scale versus air mass as presented in Eq. 4.5:

$$\ln \mathrm{DNI}(\lambda) = \ln \mathrm{DNI}_0(\lambda) - [\tau_{\mathrm{R}}(\lambda).\mathrm{m}_{\mathrm{R}} + \tau_{\mathrm{a}}(\lambda).\mathrm{m}_{\mathrm{a}} + \tau_{\mathrm{NO_2}}(\lambda).\mathrm{m}_{\mathrm{NO_2}} + \tau_{\mathrm{H_2O}}(\lambda).\mathrm{m}_{\mathrm{H_2O}} + \tau_{\mathrm{O_2}}(\lambda).\mathrm{m}_{\mathrm{O_2}} + \tau_{\mathrm{O_3}}(\lambda).\mathrm{m}_{\mathrm{O_3}}] \quad 4.5$$

4.2.2.1 AOD-retrieval method

In this work, we have calculated the EKO AOD at the same nominal wavelengths as those of the Cimel sun photometers (340, 380, 440, 500, 675, and 870 nm), by integrating the measured irradiance on the considered bandpass (see Table 4.1) and following the methodology used by AERONET (Holben et al., 2001; Giles et al., 2019, and references therein). For each wavelength, we have taken the spectral corrections shown in Table 4.1 into account. All wavelengths have been corrected by the Rayleigh scattering. Furthermore the 340, 380, 440, and 500 nm are corrected for

nitrogen dioxide (NO_2) absorption, with the optical depth being calculated by using the OMI total column NO_2climatological monthly averages and the NO_2absorption coefficient from Burrows et al. (1999). The 340, 500, and 675 nm channels are corrected for column ozone, by using the ozone values from the Izaña WMO–GAW reference Brewer spectrophotometer.

4.2.2.2 Corrections in AOD under relatively high CSR

The full opening angle and the FOV are normally used indistinctly in the literature, which should not be confused with the viewing angle. Therefore, we use the term FOV for referring to the full opening angle. The WMO has recommended the use of instruments with FOV lower than 2.5º and slope angle of 1º (WMO, 2008) for AOD retrieval. Since the EKO MS-711 was designed for DNI measurements, it has a larger FOV of 5º, which is twice the WMO-recommended value for AOD retrievals. To account for the different geometries, we have applied a correction to the EKO irradiance measurements. In this section, we explain the methodology applied to the measurements and comparisons with Cimel AOD.

Table 4.2. Wavelengths characteristics of Cimel and spectral corrections used in the calculation of AOD

Nominal central wavelength (nm)	Filter bandpass (nm)	Spectral corrections
340	2	Rayleigh, NO_2, O_3
380	4	Rayleigh, NO_2
440	10	Rayleigh, NO_2
500	10	Rayleigh, NO_2, O_3
675	10	Rayleigh, O_3
870	10	Rayleigh

The DNI measurement implies that a certain amount of diffuse radiation is coming from the line of sight of the instrument positioned towards the Sun, and an annular region around it, the so-called circumsolar region, is measured together with the DNI coming from the Sun disc (DNISUN). The source of this diffuse radiation, the circumsolar radiation (CSR), lies in the scattering processes due to the presence of

aerosols and clouds (Blanc et al., 2014) in the atmosphere. This CSR has a high dependence on the particle size (Räisänen and Lindfors, 2019); thus, large particles (such as desert dust) produce a higher scattering on the incident beam than the smaller particles (e.g., rural background aerosols), which leads this contribution to DNI overestimate. Thus, the experimental DNI measured by a collimated instrument may be expressed as the sum of both contributions as presented in Eq. 4.6:

$$\mathrm{DNI} = \mathrm{DNI}_{\mathrm{SUN}} + \mathrm{CSR} \qquad 4.6$$

where $\mathrm{DNI}_{\mathrm{SUN}}$ is the direct normal irradiance coming from the Sun disc and CSR is the diffuse radiation coming from the sky that is seen by the instrument FOV. This FOV is defined by the instrument geometry and determines the amount of CSR reaching the instrument detector. The value of the DNI measured by the instrument also depends on the atmospheric conditions and the specific instrument characteristics.

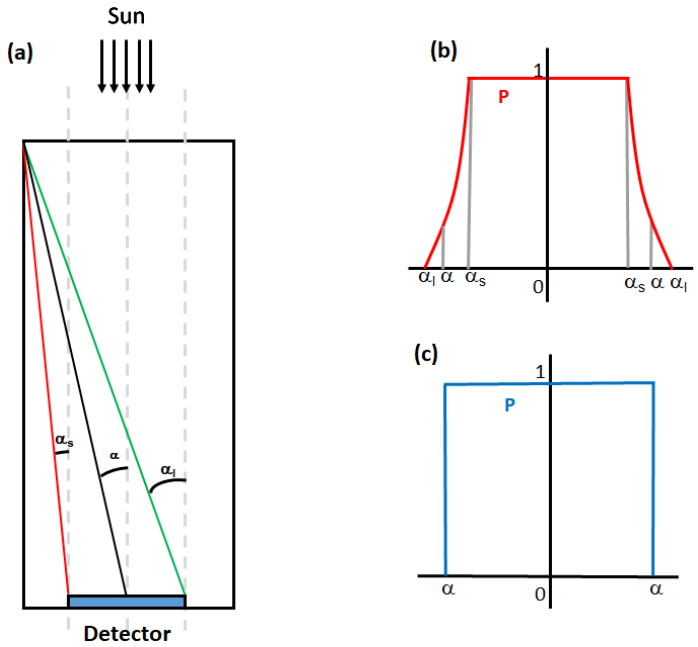

Figure 4.6: (a) Characteristic angles of the instrument: slope angle αs, aperture half-angle α, and limit angle αl. On the right, penumbra functions P (α) when (b) the three angles are known and (c) only if the angle of the half-angle is known. (Figure adapted from Blanc et al., 2014.).

The most important element that defines the amount of CSR captured by the instrument is the penumbra function P (Pastiels, 1959), which defines the fraction of Sun radiation that is captured or not by the collimator, depending on its angle of

vision. This penumbra function can be derived from the geometrical features of the instrument (Major, 1980; Blanc et al., 2014) as follows: the aperture half-angle α, the slope angle αs, and the limit angle αl (Fig. 4.6a). Usually the three angles are known, with the most important being the aperture half-angle α. Thus, the radiation coming from the sky with an angle higher than the αl is outside the collimator and is then not measured by the instrument.

If all the angles are known, then the function P takes the shape of Fig. 4.6b; if αs and αl are unknown, then the penumbra function P can be approximated as the shape on Fig. 4.6c. In this paper, we used the penumbra function P described in Fig. 4.6c because αs and αl are unknown, and we consider that α = FOV/2 = 2.5°.

4.2.2.3 CSR simulation

Since it is not possible to obtain accurate CSR measurements, it has been simulated with the LibRadtran radiative transfer model (Mayer and Kylling, 2005; Emde et al., 2016; more information at http://www.libradtran.org; last access: 7 November 2019), which provides the possibility of simulating the diffuse radiance on sky elements as defined by its azimuthal and polar angles. We briefly describe the method followed to simulate the amount of CSR measured by the EKO MS-711. The first step is to describe the geometry of the problem, as shown in Fig. 4.7.

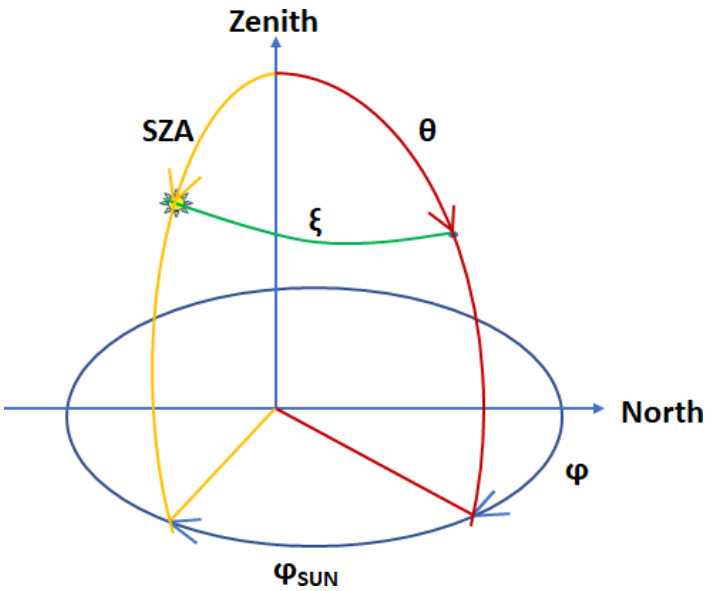

Figure 4.7: Geometry of the problem. The Sun is located at the coordinates (SZA, ϕ_{SUN}) and the sky point is in θ, ϕ. The instrument is located at the origin of the axes.

For a sky point defined by the polar angle θ and azimuthal angle ϕ, the sky radiance on that point is L (θ, ϕ) in Wm−2sr−1. The angular distance between the considered point and the Sun's position (the green arc in Fig. 4.7) is the so-called scattering angle, ξ. To obtain the angle ξ of each point in the sky in terms of the polar and azimuthal angles, the following equation should be used:

$$\cos(\xi) = \cos(\mathrm{SZA}).\cos(\theta) + \sin(\mathrm{SZA}).\sin(\theta).\cos(\phi - \phi_{\mathrm{SUN}}) \qquad 4.7$$

Taking this relation into account, the radiation field L can be expressed in terms of ξ and ϕ following Blanc et al., (2014) using P (ξ, ϕ) as the penumbra function.

If the Sun is in the angular field considered, the obtained irradiance is the DNI of Eq. 4.6; if not, the result will only be the diffuse radiation. Thus, the key is to simulate the radiances L (ξ, ϕ) of the points in the FOV that the instrument is "seeing". Taking into account that the instrument is continuously pointing towards the Sun, the integration is performed for ξ values from an initial α = 0.6º to α = 2.5º, with the aim of simulating the diffuse radiation coming from a circumsolar ring in order to compare AOD from both instruments using the same CSR.

The input parameters used in the simulations are detailed in García-Cabrera et al. (2020). The aerosol contribution has been included in the simulations by using the Optical Properties of Aerosols and Clouds (OPAC software package; Hess et al., 1998). This library provides the optical properties of the aerosol (and clouds) in the range from 250 to 4000 nm. In our case, we focused the interest on the aerosol mixtures due to the fact that the aerosols in the atmosphere are found as a mixture of different particles. In the libRadtran package the aerosol mixtures described in Hess et al. (1998) are included. The following aerosol optical properties stored in the data sets are used: the extinction coefficient, scattering coefficient, absorption coefficient, volume-phase function, single scattering albedo, and asymmetry parameter. Due to the location of the IZO station, we have selected the desert mixtures for the cases of low and high aerosol load.

At this point we should note that the use of 1D simulations with the discrete ordinate method radiative transfer (DISORT; Stamnes et al. (1988)) solver implies that the Sun is supposed to be a Dirac delta function, while the Sun has an angular radius of 96011.12 ± 011.09 (Emilio et al., 2012). However, Stamnes et al. (1988) demonstrated

that the error in DNI_{SUN} simulations, when the Sun is assumed to be a point source, is negligible with respect to the finite sun assumption (Stamnes et al., 2000; Reinhardt, 2013); this showed that the simulations of radiances in the vicinity of the Sun that were performed using the DISORT and OPAC aerosols for cloud- free cases gave the same results as the simulations made with the Monte Carlo RTE solver (MYSTIC) included in libRadtran (Mayer, 2009), by taking the angular extent of the solar disc into account. The differences remain under 1 % and even very close to 0 %. Since we want to simulate cloud-free cases, we can use the 1D DISORT without introducing significant errors into the simulations when compared to the more precise Monte Carlo simulations.

Once we have selected the input parameters, we must also select the correct angular grid in the azimuthal and polar coordinates to cover, at least, the angular region previously defined ($0.6^o \leq \boldsymbol{\alpha} \leq 2.5^o$). By using Eq. 4.7 we can calculate the ranges of polar angles θ and azimuthal angles ϕ needed.

The result of a monochromatic simulation, i.e. L(ξ, ϕ) at 495 nm for the day 26 July 2019 at SZA of ~ 14º, is shown in Fig. 4.8a. In Fig. 4.8b the penumbra function, i.e., P (ξ, ϕ), is shown, and in Fig. 4.8c the result of multiplying P (ξ, ϕ) L (ξ, ϕ) is shown. Note that the angular grid has been selected in steps of 0.1º.

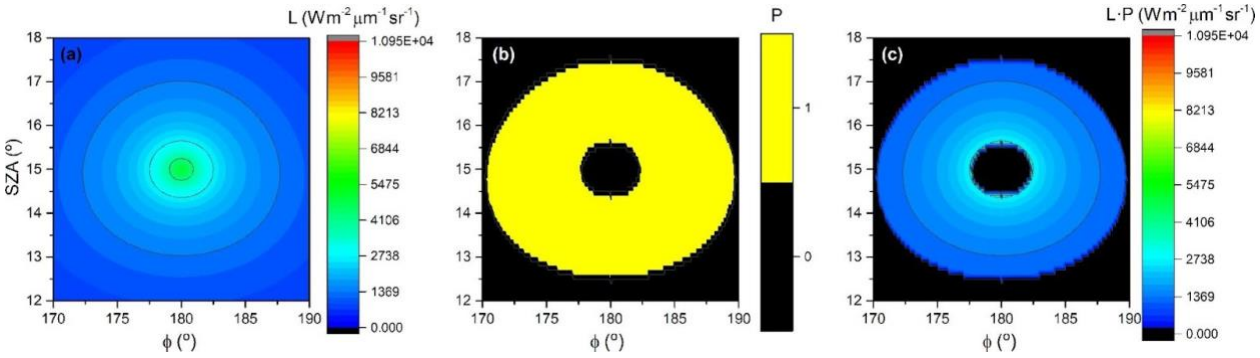

Figure 4.8: Example of the (a) diffuse radiance L (Wm−2 µm−1 sr−1) at 500 nm shown in colours at different SZA ϕ; (b) penumbra function.

The expected CSR will be obtained by integrating the radiation field P (ξ, ϕ) L (ξ, ϕ). The integration is done by using the angles tool (Mayer and Kylling, 2005) that is provided in the libRadtran package, which uses a Monte Carlo integration in 2D to obtain the diffuse radiation in the considered radiation field.

4.2.2.4 AOD retrievals with CSR corrections

Once the CSR has been determined, we apply the correction to the measured DNI by taking the CSR simulations explained before into account. Thus, from Eq. 4.6 the corrected DNI is as follows:

$$\mathrm{DNI}_{\mathrm{CORR}} = \mathrm{DNI} - \mathrm{CSR} \qquad 4.8$$

This correction will lead to a $\mathrm{DNI}_{\mathrm{CORR}} < \mathrm{DNI}$ with which we can retrieve an AOD with a similar expression than in the previous case. But taking into account that DNI_0, calculated with the Langley plot calibration method, should also be calculated by applying the FOV correction using Eq. 4.3 and substituting $\mathrm{DNI}_0$with the corrected $\mathrm{DNI}_{0,\mathrm{CORR}}$. The EKO $\mathrm{AOD}_{\mathrm{CORR}}$ obtained with a $\mathrm{DNI}_{0,\mathrm{CORR}}$ is supposed to be "free" of any CSR contribution, and then it is straight-forward to assume that the $\mathrm{AOD}_{\mathrm{CORR}}$is closer to the real AOD present in the atmosphere.

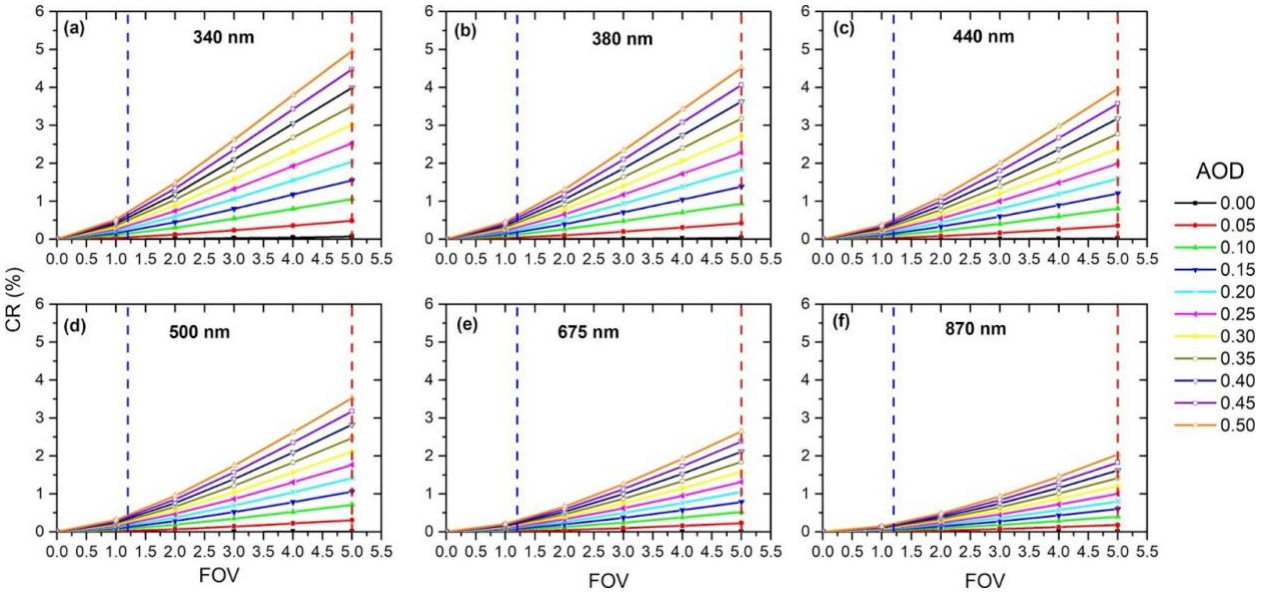

Figure 4.9: Simulations of CR at (a) 340, (b) 380, (c) 440, (d) 500, (e) 675, and (f) 870 nm for AOD between 0.0 and 0.50, and FOV between 0 and 5º at SZA 30º. The dashed blue and red lines represent the Cimel FOV (1.2º) and EKO MS-711 FOV (5º) respectively.

In order to know the impact of the aerosol load and the FOV size in the values of the CSR simulations, we have calculated the ratio of the simulated CSR with respect to the DNI given by Eq. 4.6. This is the so-called circumsolar ratio (CR) under cloud-free conditions. We have performed simulations of $\mathrm{DNI}_{\mathrm{SUN}}$ and CSR to get the previously cited CR, by varying the aerosol load in the range [0–0.50] and the FOV in the range [0–5º]. The rest of the input parameters remain fixed. The results of CR are shown in

percentages (Neumann and Witzke, 1999) for a solar zenith angle of 30º for the six Cimel channels in Fig. 4.9.

$$\mathrm{CR}(\%) = \frac{\mathrm{CSR}}{\mathrm{DNI}_{\mathrm{SUN}}+\mathrm{CSR}} \mathrm{x}100 \qquad 4.9$$

As seen in Fig. 4.9, CR increases for higher FOV and larger AOD, as expected, and for the lower wavelengths. The dashed lines in Fig. 4.9 indicate the FOV of the instruments used in this study with the Cimel (blue line) and EKO (red line) results. In all cases, the CR for the Cimel is lower than 1 % and even 0.5 % for the channels over 440 nm. For EKO, the CR ranges between 2 % in the 870 nm channel and 5 % for the 340 nm channel. Thus, the expected CSR maximum values in Fig. 4.9 should be found under these conditions: FOV of 5º, AOD of 0.50, and wavelength of 340 nm in which a CR of 5 % is found. We have simulated the AOD retrievals as a function of CSR. By combining Eq. 4.8 to 4.9, we can vary CR (the value of CSR, in fact) and calculate the AOD retrieved with the corresponding $\mathrm{DNI}_{0,\mathrm{CORR}}$.

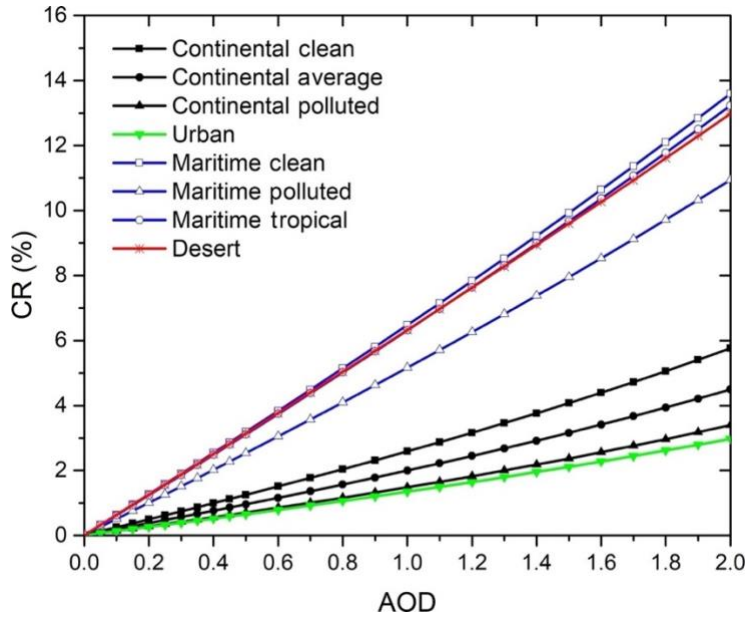

Figure 4.10: Simulations of CR (%) for SZA 30º at sea level for AOD values between 0 and 2, at 500 nm, for different types of aerosols for FOV of 5º.

These results indicate that the CSR impacts significantly on the EKO AOD retrievals under relatively high AOD, which leads to AOD underestimation, with the effect being less important for the Cimel AOD retrievals because of its narrower FOV.

These results have been simulated for different aerosol regimes. Simulations of the effect on the CR of the eight OPAC mixture aerosols available in the libRadtran

model, which include continental (clean, average, and polluted), urban, maritime (clean, polluted, and tropical), and desert aerosols (Hess et al., 1998) for FOV = 5º are shown in Fig. 4.10. For SZA = 30º, with an AOD_{500} nm range between 0 and 2 at sea level, two defined groups are distinguished, namely the continental and urban aerosol mixtures, and the maritime and desert dust mixtures. It should be noted that for stations located in urban or continental (clean and contaminated) environments, which are the majority, the correction that would have to be made to the AOD for a very high aerosol load (e.g., AOD = 1) would be much lower, between 1/3 to 1/6, than the correction that would have been performed in the case of dust aerosol.

4.2.2.5 Langley calibration

Based on the experience of Toledano et al. (2018), we have considered that the Langley calibration is suitable if the standard deviation (σ) of the fit (Eq. 4.3) is lower than 0.006, the correlation coefficient (R) > −0.99, the number of valid points > 33 % of the initial sample, and AOD (500 nm) < 0.025. An example of Langley plots using the UV–VIS near-IR direct Sun measurements on 19 March 2019 at the Izaña Atmospheric Observatory is shown in Fig. 4.11.

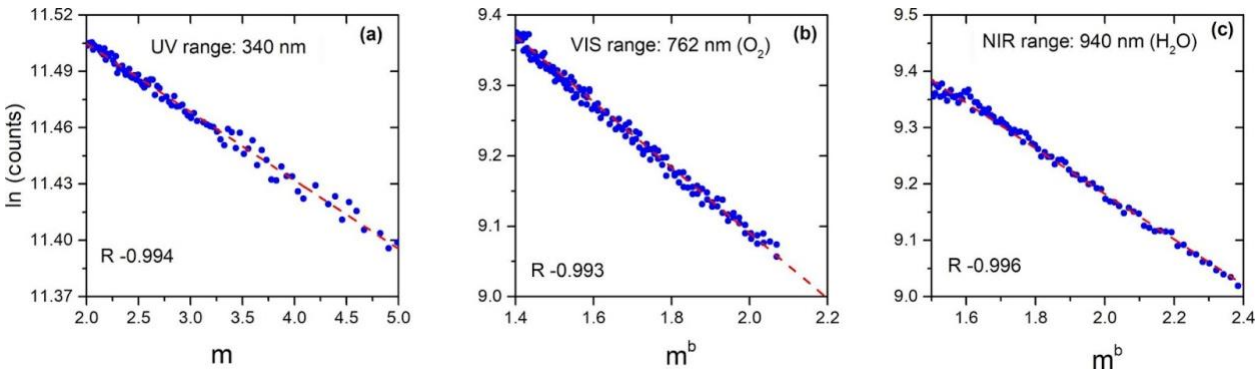

Figure 4.11: Examples of Langley plots using the UV–VIS near-IR direct Sun measurements on 19 March 2019 at the Izaña Atmospheric Observatory at (a) 340 nm, (b) 762 nm (O_2), and (c) 940 nm (H_2O) nm. R: correlation coefficient.

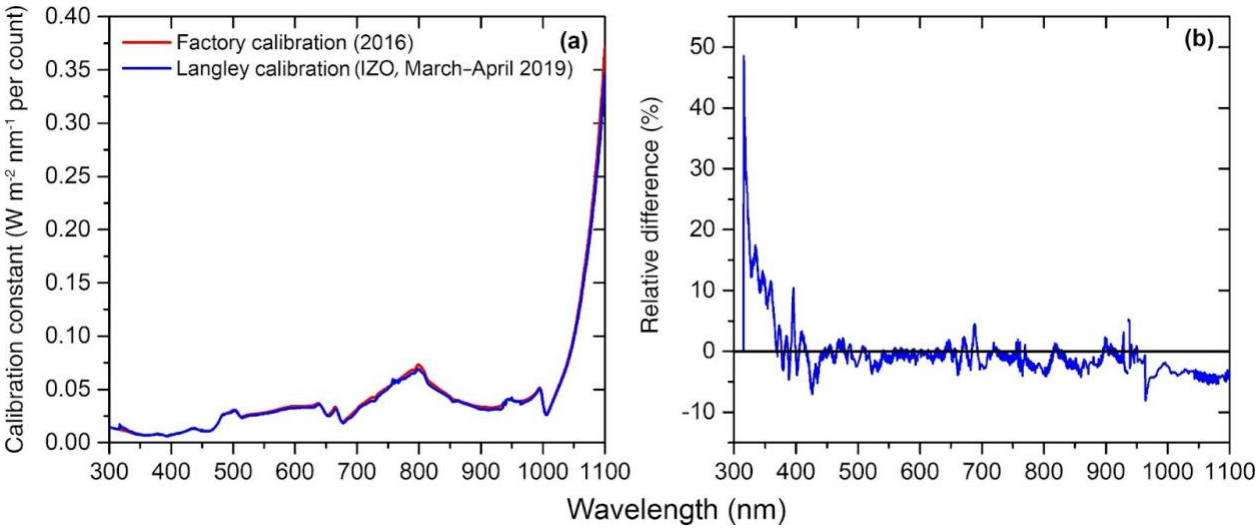

Figure 4.12: (a) Calibration constants (W m^{-2} nm^{-1} per count) of the EKO MS-711 spectroradiometer, and (b) relative differences between factory calibration constants and those obtained from Langley plots at IZO.

The comparison between the factory calibration performed by EKO Instruments in 2016 and the IZO Langley plot calibration (2019) is shown in Fig. 4.12. These results indicate that the stability of the EKO MS-711 in the range of 300–1100 nm during a 3-year period, between the manufacturer's lamp calibration and the Langley calibrations at IZO, is remarkable. The factory calibration and the IZO Langley plot calibration 3 years later present differences ~ 4.8% between 350 and 1100 nm, and even ≤ 2.3% and 3.1% in the VIS and near-IR range respectively. The larger differences below 350 nm are attributed to the low halogen lamp signal, which was experienced in this region during the factory calibration, and the low instrument sensitivity in this region.

4.2.2.6 Applications at IARC, AEMET (Izaña)

The EKO MS-711 has been designed for spectral solar DNI measurements, and therefore it has a relatively high FOV (5º), which is double the FOV recommended by WMO for AOD radiometers and 4 times larger than the AERONET–Cimel FOV. This difference in FOV might lead to a significant difference in near-forward scattering under relatively high aerosol content, which results in a small, but significant, AOD underestimation, especially in the UV range.

However, the AOD retrievals from an EKO MS-711 spectral DNI measurements show a rather good agreement with those from an AERONET reference radiometer. The

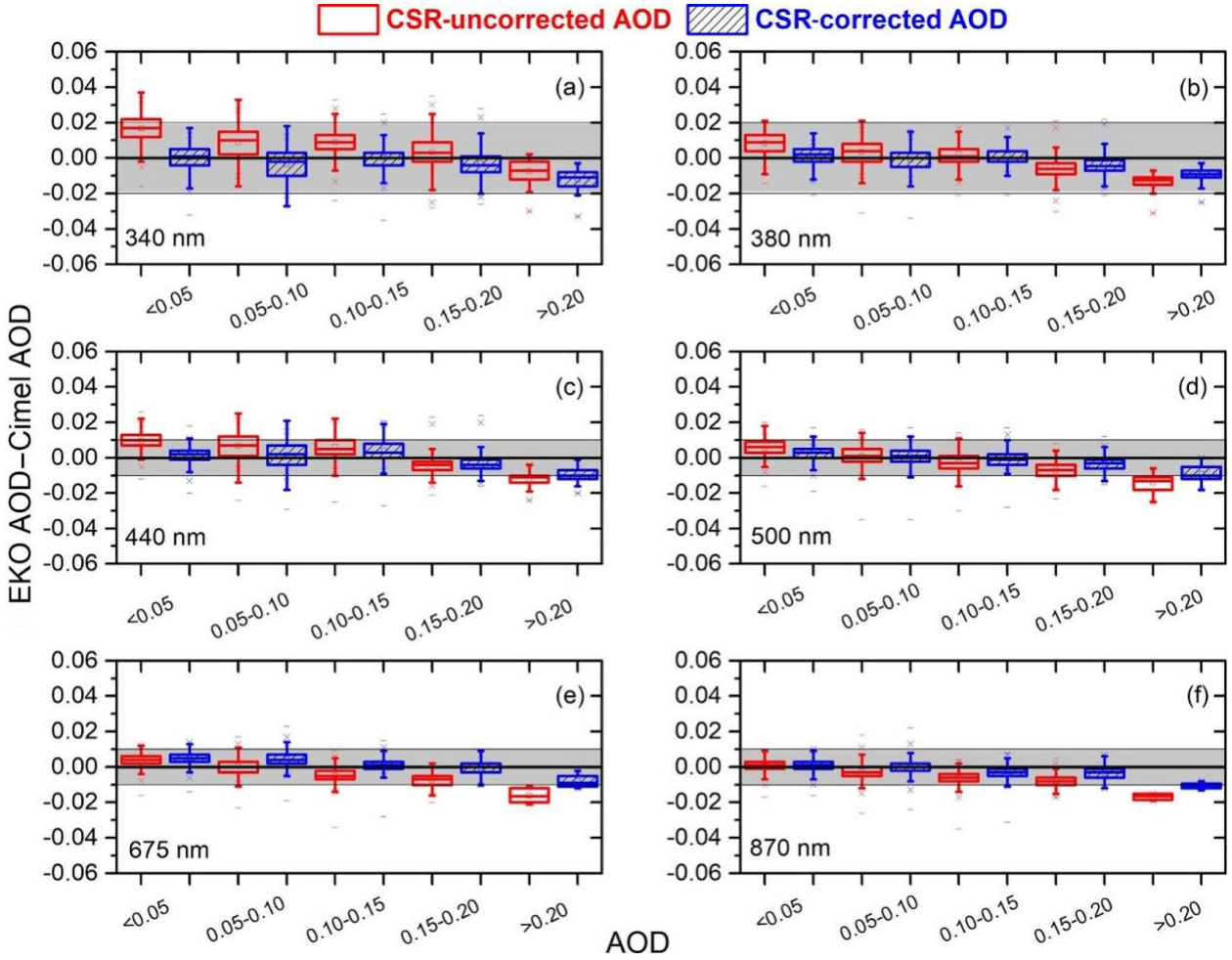

Figure 4.13: Box plot of the differences between the EKO AOD with (no) CSR corrections and Cimel AOD versus AOD for the period April– September 2019 at IZO in blue (red). Lower and upper boundaries for each box are the 25th and 75th percentiles; the solid line is the median value; the crosses indicate values out of the 1.5-fold box area (outliers); and hyphens are the maximum and minimum values. Shadings show the range of uncertainty of Cimel (±0.02 for the UV range and ±0.01 for VIS and near-IR ranges; Eck et al., 1999).

AOD comparison was held at the Izaña Atmospheric Observatory between April and September 2019. Quality assessment of the EKO MS-711 AOD has been performed by comparing it with coincident AOD from AERONET at 340, 380, 440, 500, 675, and 870 nm, by considering measurements from both instruments that are as close as 2 min apart, with a total of 14 706 analyzed data pairs. The skill scores of the AOD comparison are fairly good, with a rms of 0.013 (24.6 %) at 340 and 380 nm, and 0.029 (19.5 %) for longer wavelengths (440, 500, 675, and 870 nm), and with AOD being under- estimated by the EKO radiometer. The MB (EKO AOD– Cimel AOD) is 0.011

(19.7 %) for 340 and 380 nm, and 0.004 (10.6 %) for 440, 500, 675, and 870 nm. These results improve considerably when we take into account the CSR corrections made to EKO AOD because of the higher EKO FOV. The CSR differences between EKO and AERONET–Cimel were obtained by using a libRadtran model. When comparing the EKO AOD-corrected values, the rms is reduced to 0.006 (14.9 %) at 340 and 380 nm and to 0.005 (11.1 %) for longer wavelengths, while MB is reduced to < 0.001 (1.3 %) for 340 and 380 nm, and < 0.001 (0.4 %) for 500, 675, and 870 nm. These values are within the Cimel instrumental uncertainty (±0.01 in the VIS and near-IR, and ±0.02 in the UV ranges). Comparison results are reported in Fig. 4.13.

Following WMO recommendations, we have analysed the percentage of EKO AOD–Cimel AOD differences within the WMO U95 limits defined for finite FOV instruments, and we found that with no CSR corrections ≥ 96 % of the AOD differences fell within the WMO U95 limits at 500, 675, and 870 nm. After applying the CSR corrections, the percentage of AOD differences within the WMO U_{95} limits were > 95 % for 380, 440, 500, 675, and 870 nm, while for 340 nm the percentage of AOD differences within the WMO U95 increased only to a modest 86 %. The known greater AOD uncertainty in the UV range, along with stray-light problems not fully corrected in this instrument, seems to be the reason behind the poorer AOD agreement with AERONET–Cimel at 340 nm.

The EKO MS-711 has proven to be an instrument which, despite having been designed for solar radiation measurements, can provide high-quality AOD measurements in the VIS and near-IR ranges, with excellent results when compared to the AERONET–Cimel reference radiometer, which, in turn, has shown a very good AOD traceability with the WORCC's World AOD reference.

4.2.2.7 Method applied to EKO spectroradiometer of Montevideo, Uruguay

Contributor: Paola Russo Ganón

AOD retrievals at various wavelengths (340, 380, 440, 500, 675 and 870 nm) have been performed in Montevideo Uruguay, using spectral irradiance ground measurements taken with an EKO MS711 DNI spectroradiometer. The AOD estimates have been compared to AOD from AERONET, in the same site (Russo et al., 2023).

Solar spectral irradiance is attenuated exponentially as described by the Beer-Bouguer-Lambert law:

$$I_{\lambda} = I_{0,\lambda} e^{-m\tau_{\lambda}} \quad 4.10$$

Being: I_{λ} the solar beam spectral irradiance measured at ground level, $I_{0,\lambda}$, the spectral irradiance at the top of the atmosphere (TOA), m the relative air mass and τ_{λ} the total optical depth. $I_{0,\lambda}$ is computed as: $I_{s,\lambda} \times F_n$ where $I_{s,\lambda}$ is spectral irradiance that the instrument would measure if it was located at TOA, F_n the orbital correction factor. The main contributions to attenuation are considered to be: Rayleigh Scattering (r), aerosols (a), water vapour (w), absorption by atmospheric gasses (NO_2 and O_3), therefore:

$$\tau_{\lambda} m = \tau_{r\lambda} m_r + \tau_{a\lambda} m_a + \tau_{w\lambda} m_w + \tau_{NO_2\lambda} m_{NO_2} + \tau_{O_3\lambda} m_{O_3} \quad 4.11$$

Combining Eq. 4.10 and 4.11 the AOD at a specific wavelength, $\tau_{a\lambda}$, can be retrieved.

Langley Plot Method

$I_{s,j,\lambda}$ is estimated using the Langley Plot method, Fig. 4.14a shows how the value is obtained as an example: $I_{s,j,\lambda}$ = 500 = 1865.7 W/m^2/μm.

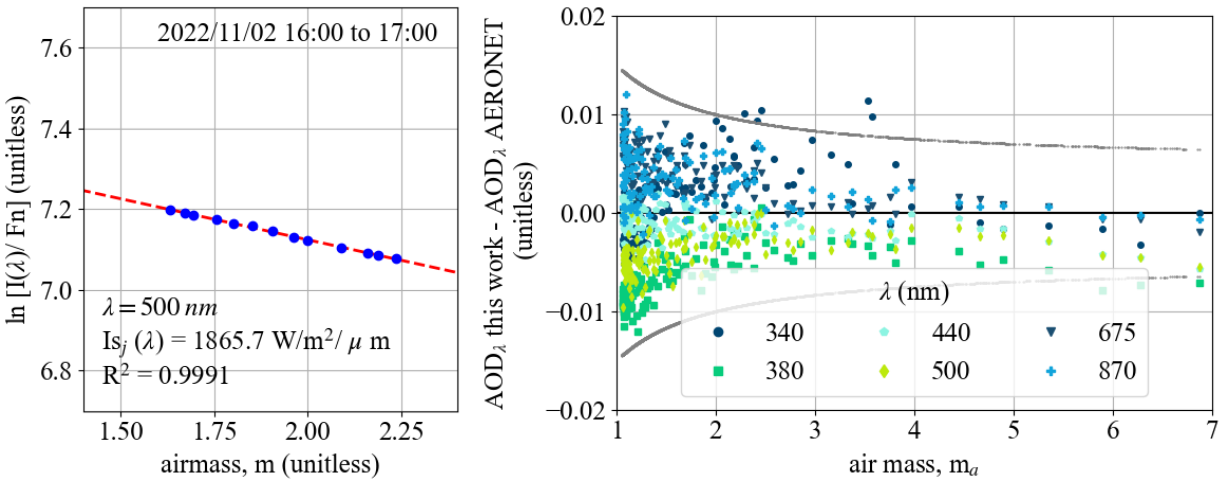

(a) (b)

Figure 4.14: Langley plot method applied to the EKO spectroradiometer in Montevideo. (a): Langley Plot graphic for channel 500 nm. (b): WMO Criteria applied at diverse channels for validation of the method vs. AERONET instrument (Cimel).

For the $I_{s,j,\lambda}$ values to be considered acceptable, the difference between AOD_{λ} retrieved and reference (AERONET) must comply the U_{95} criterion for more than 95%

of the instants used to find $I_{s,\lambda}$ (U_{95}<0.005+0.010/m_a WMO/GAW, 2004). Figure 4.14b shows how the criterion is applied during the calibration day.

Circumsolar correction

A circumsolar correction needs to be applied specifically to the EKO measurements (I_λ), since the instrument's field of view is 5° (when it should be 2.5° for AOD retrievals, WMO/GAW, 2004). $I_{\lambda,corr} = I_{obs}(1 - CR)$. The correction factor CR, which is dependent on AOD_λ, is estimated using a look-up table of CR-AOD created by García-Cabrera et al. (2020).

Results

As an example, results of $AOD_{\lambda=500}$ estimated are shown in Fig. 4.15 compared to AERONET, obtaining an MBD and RMSD of -0.004, 0.004 (unitless) respectively.

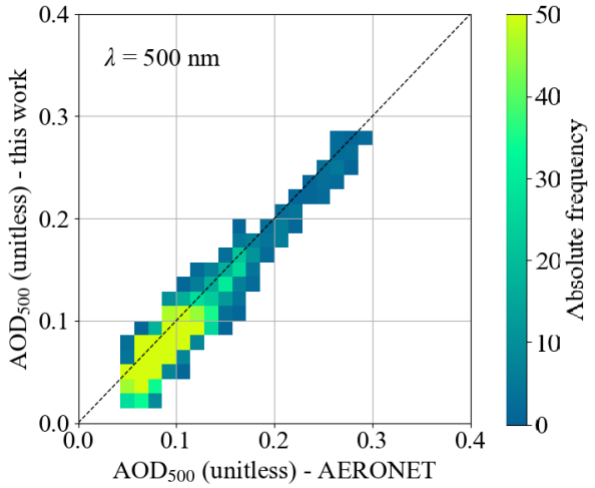

Figure 4.15: Comparison of AOD 500 nm retrieved by EKO in Montevideo vs. AERONET product obtained with the Cimel at the same site. From Russo et al. 2023

4.2.3 Methods to retrieve AOD with PSR

Contributors: Natalia Kouremeti, Julian Gröbner, Dimitra Kouklaki

The Precision Spectroradiometer (PSR) measures spectral direct solar irradiance over a spectral range of 320–1030 nm, with a spectral resolution of 0.7 nm and FWHM ranging from 1.7 nm to 6 nm depending on the configuration of the instrument. The spectral AOD retrieval (Eq. 4.2 of Section 4.2.1) is based on SI-traceable direct solar irradiance measurements and the use of a high resolution ToA solar spectrum provided by satellite and ground-based measurements. Specifically, the

QASUMEFTS (Gröbner et al. 2017) in the range 320 nm to 450 nm and the TSIS-1 HSRS (Coddington et al. 2023) in the range 450 nm to 1030 nm are used.

The calibration is performed using transfer lamp irradiance standards and the stray-light correction is defined in the tunable laser system of PMOD/WRC. The expanded relative uncertainty for spectral solar irradiance measurements in the 350–1000 nm range is between 1.7% and 2.0%, with larger uncertainties below 400 nm which are mainly caused by the low signal levels and the uncertainties due to the straylight correction. A detailed uncertainty budget is presented in Gröbner and Kouremeti (2019). Corrections applied to the measured irradiance are dark correction, stray-light correction, wavelength shift, spectral responsivity adjustment to wavelength scale. The high resolution ToA spectrum, ozone cross section (Serdyuchenko et l. 2014) and Rayleigh scattering (Bodhaine et al. 1999). are convolved with the interpolated line-spread-functions of the PSR excluding the stray-light contribution (Kouremeti, et al., 2022).

The cloud screening is based on the variability of the measurements over 10 min and combined with the high temporal resolution irradiance measurements of a collocated PFR instrument. Currently, only ozone is accounted for, using measurements from a co-located Brewer spectrometer or daily mean value from OMI. The spectral bands contaminated by the rest of the trace gases are deleted based on climatological values and optical depth contribution higher than 1%.

The performance of the PSR instruments in terms of AOD retrievals and direct solar irradiance measurements has been validated against the filter radiometers GAW-PFR-TRIAD, Cimel-AERONET and reference spectroradiometers QASUME and JRC ESTI spectroradiometers (e.g., Gröbner et al. 2023, Gröbner and Kouremeti, 2019, Kazadzis et al. 2023, Pavanello et al. 2021, Kazadzis et al. 2018b, Kazadzis et al. 2016). The agreement in the range 380 nm and 1020 nm is within the WMO recommended limits for traceability when the TSIS-1 HSRS or QASUMEFTS and TSIS-1 HSRS ToA spectra are used.

PSR AOD retrievals in Lindenberg and Berlin

Deutscher Wetterdienst (DWD) is operating two PSRs. One at Lindenberg (Tauche) at the Meteorological Observatory Lindenberg (MOL-RAO, DWD) and one in Berlin

at the site of the Institut für Meteorologie, Freie Universität Berlin (IfM, FUB), and DWD is retrieving the AOD using its own retrieval algorithm.

The AOD retrieval method is similar to the AOD retrieval used for the BTS (Section 4.2.1), for the EKO (Section 4.2.2) and for the PSR (beginning of this section: method of Gröbner and Kouremeti, 2019): We trust the direct sun spectral irradiance measured by the spectroradiometer (so far the calibration is not old: We know the possible uncertainty) and we use the tabulated direct sun solar spectral irradiance that is incoming in the atmosphere.

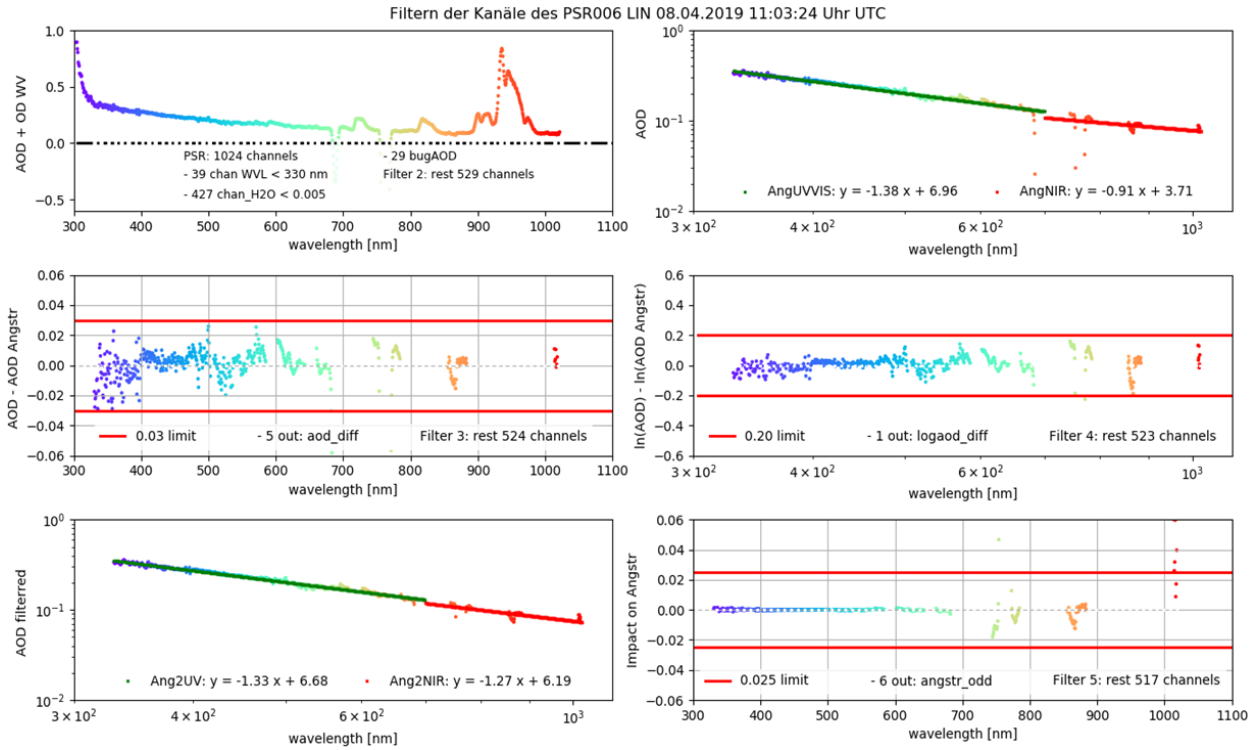

Figure 4.16: Filtering method to eliminate the PSR channels of low quality AOD retrieval in the DWD method. Above-left: Spectrum of AOD+gas absorption optical depth before filtering, middle-left: spectrum of AOD minus AOD from Ångström law before Ångström filters; middle-right: same as middle-left but with log x axis (log AOD vs log(wvl)). Below-right: test "impact on Ångström law" of each channel in order to filter the outliers; Above right: visualisation of AOD retrieved on Ångström law plotted before Ångström filters; Below left: same but after Ångström filters - source: Oehlschlägel 2019.

The method used to retrieve AOD is described in Oehlschlägel (2019). The database used for the solar spectral irradiance at the entrance of the atmosphere is QASUMEFTS (Gröbner et al. 2017) in the range 320 nm to 500 nm and Thuillier et al.

(2003) for the range 500 to 1020 nm (end of the range of the instrument). The particularity of the method of Oehlschlägel (2019) used by DWD is the caution given to select which of the 1024 PSR channels are adapted or not to apply the Beer-Bouguer-Lambert law and retrieve the AOD with the photometry method. Figure 4.16 summarises this filtering: First we eliminate the channels for which the constructor considers the irradiance product as less certain (wavelength < 330 nm: 39 channels are eliminated). Second, we eliminate the channels for which the gas optical depth (mostly water vapour but also O_2 close to 767 nm) if higher than 0.005: 427 channels are eliminated. Then we choose a day with a normal aerosol amount on which we can presume that the aerosols are spherical and following the Ångström law: logarithm of AOD is linear in logarithm of wavelength. We define two linear Ångström bands (UVA+VIS: 330 - 700 nm and NIR: 700-1020 nm), and we eliminate the outliers in AOD obtained with the photometry (Beer-Bouguer-Lambert equation) retrieval method. This last stage eliminates again 29 channels for the PSR #6 of the station Lindenberg. At the end only 529 from 1024 channels of the PSR remains for the retrieval of the AOD, but from better quality, and nonetheless covering well the band UVA-VIS-NIR (330 - 1020 nm).

Another outcome of the DWD method is the importance of calibration: If in the six to twelve months after calibration more than 90% of the compared PSR AOD retrievals suit to Cimel and PFR AOD measurements considering the WMO criteria, after one and a half or two years, when the irradiance calibration of the PSR is requested, this coincidence percentage is only about 70-80 %.

5. Summary

This COST Action HARMONIA deliverable was aimed at presenting an overview on the established techniques and existing tools as well as possibility of homogenisation by reporting on the differences and uncertainties related to standard products provided from already existing analysis algorithms. Another aim of this deliverable is to present the most recent studies regarding retrieval methods of AOD with photometers and spectroradiometers using the photometry retrieval technique (Beer-Bouguer-Lambert equation), especially to report about the studies done in the HARMONIA context or granted by the COST Action HARMONIA.

With these aims, this deliverable presented a brief summary of the cloud screening methodologies followed by different AOD measurement techniques as well as some new techniques related to machine learning and synergism between instrumentations. An overview on the cloud flagging (flagging out of the AOD measurements that may be contaminated by clouds) algorithms existing in the three global AOD networks (AERONET, SKYNET and GAW-PFR) has been presented that follow certain criteria such as AOD triplet variability, air mass, AOD and AE thresholds. Further, a machine learning based algorithm has also been introduced that uses the k-nearest-neighbour algorithm for automated cloud detection with successful application at three locations namely Innsbruck, Izaña and Davos and good agreement with conventional cloud flagging algorithms.

Synergism between different types of instrumentation has also been seen to be useful to some extent for cloud flagging objectives of sun photometers. To this direction, a synergism of camera and broadband measurement was taken into account that showed a good agreement between clear-sun models and the all-sky camera which was higher than for clear-sun models and photometers or photometer–photometer. The possible future developments of this analysis could be to extend data set to include more sun photometers, focusing on mismatches occurring at very low or very high values of Ångström coefficient; analysis with a higher temporal resolution for all-sky camera products (especially cloud flagging) going to every minute or lower.

Another synergistic study was presented with a sun photometer (PFR) and spectroradiometer (Pandora) to assess the performance of already existing stand-alone cloud flagging algorithms of these instrumentations. In general, these two algorithms were found to agree well for a yearly (2023) analysis of the station at Izaña. The PFR cloud flags agreed quite well with Pandora quality flags during dust events. However, during smoke events, Pandora quality flags were observed to degrade for PFR clear sun flags with more data points classified as medium and low quality associated with high atmospheric variability due to smoke plume and not due to the presence of clouds. This analysis highlights the fact that smoke events can be tricky for cloud flagging algorithms due to high atmospheric variability especially if the station is located near the fire source and the AOD values are quite high.

Further, there was an extensive analysis on the comparison between AOD products from the instrumentations belonging or associated to the three global networks namely AERONET, SKYNET and GAW-PFR that deal with the instruments Cimel, Prede and PFR respectively. The station used to lead this study is the Meteorological Observatory Lindenberg of Deutscher Wetterdienst (MOL-RAO, DWD) at Lindenberg (Tauche) in Germany. This station has been chosen since it operates since more than eleven years the three AOD sun photometers in parallel: Cimel, Prede and PFR. Therefore, the "Lindenberg-Dataset" is an adequate dataset for long term cross-comparison of Cimel, Prede and PFR AOD measurements and retrievals (AERONET, SKYNET, GAW-PFR). We conducted two studies in parallel. We note first that the way how we define a pair of measurements for comparison and how we filter the orígínal dataset has an influence on the statistical result of the intercomparison study. The learning is that it is important to document well the way how the comparison points are defined in order to avoid artefacts in the comparison dataset. Despite these differences both studies showed a good agreement for Prede to Cimel comparison, regarding the WMO coincidence criteria. Two different Cimel photometers are operated in Lindenberg and for the years with the higher differences PFR-Cimel it is not the same behaviour depending on which Cimel instrument unit is used. This is the second learning of this study. Temporal variations of the difference from one instrument to another has to be interpreted with the information contained in the station and instruments logbook (calibration dates, hardware issues, interruptions, difficulties, etc.). And for a further study, the dataset should be filtered again regarding the logbook's records. Both studies highlight also, that the differences in AOD measurements between Prede and the other instruments (PFR or Cimel) is consequently higher than the difference between PFR and Cimel. It is not a surprise, since PFR and Cimel of the station Lindenberg have a similar strict calibration method: Travelling of the instrument to a calibration site and calibration transfer at this site from a reference instrument or langley plot calibration on this site. Differently, Prede uses on-site langley plot calibration at the Lindenberg station "improved langley plot", "improved" because Lindenberg is not an appropriate site for Langley Plot method. These calibration issues are not analysed and quantified in this report but in the deliverables of HARMONIA Working Group WG2: D2.2 "List of possible improvements on the quality of solar, lunar and stellar photometry instrumentation" that is published in parallel to this deliverable.

This deliverable also presents an analysis of the influence of NO_2 on the AOD and AE retrievals depending on the NO_2 representation (i.e., satellite climatology vs real NO_2 measurements) in optical depth estimation. This analysis dealt with AERONET AOD measurements that uses OMI satellite based climatological representation of NO_2 for optical depth estimation which was replaced with Pandora NO_2 measurements. It was observed that the NO_2 absorption affects AOD measurements in UV-VIS region of the electromagnetic spectrum and NO_2 absorption based AOD correction affected 380 nm the most followed by 440 nm, 340 nm and 500 nm, respectively. Out of the 33 worldwide stations under consideration, ~half of the stations were found to have overestimation by AERONET AOD when corrected with Pandora NO_2 measurements, while also underestimation in other cases. It was also observed that ~1/3rd of the stations total considered stations had a mean difference in NO_2 (between AERONET OMI satellite based and Pandora measurements) and AOD (original AERONET AOD and Pandora NO_2 based corrected AOD) (at 380 and 440 nm) more than 0.5×10^{-4} mol m^{-2} and 0.002, respectively. The AOD differences can be considered as a systematic contribution to the uncertainties in the AOD measurements that are reported to be of the order of 0.01. Moreover, extreme NO_2 loading scenarios (i.e., 10 % highest differences) at highly urbanised/industrialised locations revealed even higher AOD differences observed that were found to be at the limit of or higher than the reported 0.01 uncertainty in the AOD measurement. The sensitivity study results and values can give some explanation about the small gap at 500 nm between AOD retrieved with AERONET method (Cimel and with NO_2 correction) and with GAW-PFR method (PFR and without NO_2 correction).

In order not to restrict this study to a pure sun photometer review, we presented the night campaign SCILLA (Summer Campaign for Intercomparison of Lunar measurements of Lindenberg's Aerosol) that happened also in Lindenberg and involved 7 lunar photometers (5 Cimels, 1 Prede and 1 PFR) and two-star photometers. SCILLA's dataset has also intercomparison potential and columnar measurements (photometers) can be compared to vertical profile measurements (LIDAR, COBALD balloon carried radiosondes).

The deliverable also presents an overview on high spectral resolved AOD by different types of instruments. First in the ultraviolet (UV) where these measurement techniques are required since the use of photometers is challenging

in the UV-B (280 - 315 nm) spectral band. We presented an overview of the techniques that have been used. First the use of the monochromator UV-B spectrometer Brewers, originally designed for UV monitoring and total ozone column (TOC) retrievals. Then the very efficient use of UV Array spectroradiometers (UV-BTS), a more modern instrument that is also designed for TOC and UV monitoring. We reported from cross comparison studies and operational activities of these two systems retrieving the AOD in the UV. Also, in the casual AOD spectral bands (UVA, VIS, NIR: 300 - 10000 nm) array spectroradiometer are interesting instruments for AOD retrievals, since they allow the retrieval of a high spectral resolved spectrum of the AOD. This is now possible since these instruments reached a high-quality level of measurements of direct solar irradiance spectra, with very low uncertainties and traceable to the SI. Therefore, the spectral irradiance measured (I_λ) can be put in the Beer-Bouguer-Lambert equation as well as the tabulated well known spectral solar irradiance in the entrance of the atmosphere (as $I_{0\lambda}$). Then it is very easy to retrieve the total optical depth and in a second step, knowing the concentration of absorbing gases, the AOD. We presented in this deliverable cross comparison studies and operational activities of AOD retrieval with high spectral resolved measurements of the direct sun irradiance using instruments of three types: BTS, EKO MS -711 and PSR. These new validated challenges offer more possibilities to increase the understanding of the aerosol characteristics (spectral signature and link to the microphysics for instance).

References

1. Ångström, A.: Apparent solar constant variations and their relation to the variability of atmospheric transmission, *Tellus*, 22, 205–218, https://doi.org/10.3402/tellusa.v22i2.10215, 1970.
2. Baibakov, K., O'Neill, N. T., Ivănescu, L., Duck, T. J., Perro, C., Herber, A. B., Schulz, K.-H., Schrems, O.: Synchronous Polar Winter Starphotometry and Lidar Measurements at a High Arctic Station. *Atmospheric Measurement Techniques* 8 (9): 3789–3809. https://doi.org/10.5194/amt-8-3789-2015, 2015.
3. Bais, A. F.: Absolute spectral measurements of the direct solar ultraviolet irradiance with a Brewer spectrophotometer, *Appl. Opt*. 36, 5199–5204, https://doi.org/10.1364/AO.36.005199, 1997.
4. Barreto, A., Román, R., Cuevas, E., Pérez-Ramírez, D., Berjón, A. J., Kouremeti, N., Kazadzis, S., Gröbner, J., Mazzola, M., Toledano, C., Benavent-Oltra, J. A., Doppler, L., Juryšek, J., Almansa, A. F., Victori, S., Maupin, F., Guirado-Fuentes, C., González, R., Vitale, V., Goloub, P., Blarel, L., Alados-Arboledas, L., Woolliams, E., Taylor, S., Antuña, J. C., Yela, M.: Evaluation of night-time aerosols measurements and lunar irradiance models in the frame of the first multi-instrument nocturnal intercomparison campaign, *Atmospheric Environment*, 202, 190-211, https://doi.org/10.1016/j.atmosenv.2019.01.006, 2019.
5. Blanc, P., Espinar, B., Geuder, N., Gueymard, C., Meyer, R., Pitz- Paal, R., Reinhardt, B., Renné, D., Sengupta, M., Wald, L., Wilbert, S.: Direct normal irradiance related definitions and ap- plications: The circumsolar issue, *Sol. Energ*., 110, 561–577, https://doi.org/10.1016/j.solener.2014.10.001, 2014.
6. Bodhaine, B. A., Wood, N. B., Dutton, E. G., Slusser, J. R.: On Rayleigh optical depth calculations, *J. Atmos. Ocean. Tech*., 16, 1854–1861, 1999.
7. Bright et al.: Bright-Sun: A globally applicable 1-min irradiance clear-sky detection model. *Renewable and Sustainable Energy Reviews* 121, 109706. https://doi.org/10.1016/j.rser.2020.109706, 2020.
8. Burrows, J., Richter, A., Dehn, A., Deters, B., Himmelmann, S., Voigt, S., and Orphal, J.: Atmospheric remote-sensing reference data from GOME-2 temperature-dependent absorption cross sections of O_3 in the 231–794 nm range, *J. Quant. Spectrosc. Ra*., 61, 509–517, https://doi.org/10.1016/S0022-4073(98)00037-5, 1999.
9. Byrne, B., Liu, J., Bowman, K. W., Pascolini-Campbell, M., Chatterjee, A., Pandey, S., Miyazaki, K., van der Werf, G. R., Wunch, D., Wennberg, P. O., Roehl, C. M., Sinha, S.: Carbon emissions from the 2023 Canadian wildfires, *Nature*, 633, 835–839, https://doi.org/10.1038/s41586-024-07878-z, 2024.

10. Carlund, T., Kouremeti, N., Kazadzis, S., and Gröbner, J.: Aerosol optical depth determination in the UV using a four-channel precision filter radiometer, *Atmos. Meas. Tech*., 10, 905–923, https://doi.org/10.5194/amt-10-905-2017, 2017.
11. Chew, B. N., Campbell, J. R., Reid, J. S., Giles, D. M., Welton, E. J., Salinas, S. V., Liew, S. C.: Tropical cirrus cloud contamination in sun photometer data, *Atmos. Environ*., 45, 6724–6731, https://doi.org/10.1016/j.atmosenv.2011.08.017, 2011.
12. Cheymol, A., H. De Backer: Retrieval of the aerosol optical depth in the UV-B at Uccle from Brewer ozone measurements over a long time period 1984–2002*, J. Geophys. Res*., 108, 4800, D24, https://doi.org/10.1029/2003JD003758, 2003.
13. Coddington, O. M., Richard, E. C., Harber, D., Pilewskie, P., Woods, T. N., Snow, M., et al.. Version 2 of the TSIS-1 Hybrid Solar Reference Spectrum and Extension to the Full Spectrum. *Earth and Space Science*, 10, e2022EA002637. https://doi.org/10.1029/2022EA002637, 2023.
14. Cuevas, E., Romero-Campos, P. M., Kouremeti, N., Kazadzis, S., Räisänen, P., García, R. D., Barreto, A., Guirado-Fuentes, C., Ramos, R., Toledano, C., Almansa, F., and Gröbner, J.: Aerosol optical depth comparison between GAW-PFR and AERONET-Cimel radiometers from long-term (2005–2015) 1 min synchronous measurements, *Atmos. Meas. Tech*., 12, 4309–4337, https://doi.org/10.5194/amt-12-4309-2019, 2019.
15. De Bock, V., De Backer, H., Mangold, A. and Delcloo, A., Aerosol Optical Depth measurements at 340 nm with a Brewer spectrophotometer and comparison with Cimel sunphotometer observations at Uccle, Belgium, *Atmos. Meas. Tech.*, 3, 1577-1588, https://doi.org/10.5194/amt-3-1577-2010, 2010.
16. De Bock, V., De Backer, H., Van Malderen, R., Mangold, A. and Delcloo, A., Relations between erythemal UV dose, global solar radiation, total ozone column and aerosol optical depth at Uccle, Belgium, *Atmos. Chem. Phys*., 14, 12251-12270, https://doi.org/10.5194/acp-14-12251-2014, 2014.
17. Emde, C., Buras-Schnell, R., Kylling, A., Mayer, B., Gasteiger, J., Hamann, U., Kylling, J., Richter, B., Pause, C., Dowling, T., and Bugliaro, L.: The libRadtran software package for radiative transfer calculations (version 2.0.1), *Geosci. Model Dev*., 9, 1647–1672, https://doi.org/10.5194/gmd-9-1647-2016, 2016.
18. Estellés, V., Campanelli, M., Smyth, T. J., Utrillas, M. P., and Martínez-Lozano, J. A.: Evaluation of the new ESR network software for the retrieval of direct sun products from CIMEL CE318 and PREDE POM01 sun-sky radiometers, *Atmos. Chem. Phys*., 12, 11619–11630, https://doi.org/10.5194/acp-12-11619-2012, 2012.
19. Fountoulakis, I.; Natsis, A.; Siomos, N.; Drosoglou, T.; Bais, A.F. Deriving Aerosol Absorption Properties from Solar Ultraviolet Radiation Spectral Measurements at Thessaloniki, Greece. *Remote Sens.*, 11, 2179. https://doi.org/10.3390/rs11182179, 2019.

20. Fuertes, D.; Toledano, C.; González, R.; Berjón, A.; Torres, B.; Cachorro, V.E.; de Frutos, A.M.: CÆLIS: Software for assimilation, management and processing data of an atmospheric measurement network. *Geosci. Instrum. Methods Data Syst*., 7, 67–81, https://doi.org/10.5194/gi-7-67-2018, 2018.
21. García-Cabrera, R. D., Agullo, E., Barreto, A., Cachorro, V. E., Pó, M., Ramos, R., Hoogendijk, K.: Aerosol retrievals from the EKO MS-711 spectral direct irradiance measurements and corrections of the circumsolar radiation. *Atmospheric Measurement Techniques*, 13(5), 2601–2621. https://amt.copernicus.org/articles/13/2601/2020/, 2020.
22. Giles, D.M.; Sinyuk, A.; Sorokin, M.G.; Schafer, J.S.; Smirnov, A.; Slutsker, I.; Eck, T.F.; Holben, B.N.; Lewis, J.R.; Campbell, J.R.; et al. Advancements in the Aerosol Robotic Network (AERONET) Version 3 database—Automated near-real-time quality control algorithm with improved cloud screening for Sun photometer aerosol optical depth (AOD) measurements. *Atmos. Meas. Tech.*, 12, 169–209., https://doi.org/10.5194/amt-12-169-2019, 2019.
23. Gobbi, G. P., Kaufman, Y. J., Koren, I., and Eck, T. F.: Classification of aerosol properties derived from AERONET direct sun data, *Atmos. Chem. Phys*., 7, 453–458, https://doi.org/10.5194/acp-7-453-2007, 2007.
24. González, R., Toledano, C., Román, R., Fuertes, D., Berjón, A., Mateos, D., Guirado-Fuentes, C., Velasco-Merino, C., Antuña-Sánchez, J. C., Calle, A., Cachorro, V. E., and de Frutos, Á. M.: Daytime and nighttime aerosol optical depth implementation in CÆLIS, *Geosci. Instrum. Method. Data Syst*., 9, 417–433, https://doi.org/10.5194/gi-9-417-2020, 2020.
25. Gröbner J., Kerr, J. B.: Ground-based determination of the spectral ultraviolet extraterrestrial solar irradiance: pro viding a link between space-based and ground-based solar UV measurements, *J. Geophys. Res.* 106D, 7211–7217, https://doi.org/10.1029/2000JD900756, 2001.
26. Groebner, J. and Meleti, C.: Aerosol optical depth in the UVB and visible wavelength range from Brewer spectrophotometer direct irradiance measurements: 1991–2002, *J. Geophys. Res.*, 25(109), D09202, https://doi.org/10.1029/2003JD004409, 2004.
27. Gröbner, J., Kröger, I., Egli, L., Hülsen, G., Riechelmann, S., and Sperfeld, P., "The high-resolution extraterrestrial solar spectrum (QASUMEFTS) determined from ground-based solar irradiance measurements", *Atmos. Meas. Tech*., 10, 3375–3383, https://doi.org/10.5194/amt-10-3375-2017, 2017.
28. Gröbner, J., Kouremeti, N.: The Precision Solar Spectroradiometer (PSR) for direct solar irradiance measurements. *Solar Energy* 185: 199-210., https://doi.org/10.1016/j.solener.2019.04.060, 2019.

29. Gröbner, J., Kouremeti, N., Hülsen, G., Zuber, R., Ribnitzky, M., Nevas, S., Sperfeld, P., Schwind, K., Schneider, P., Gueymard, C. A.: Parameterized transmittance model for direct beam and circumsolar spectral irradiance, *Sol. Energ*., 71, 325–346, https://doi.org/10.1016/S0038-092X(01)00054-8, 2001.
30. Gröbner, J., Kouremeti, N., Hülsen, G., Zuber, R., Ribnitzky, M., Nevas, S., Sperfeld, P., Schwind, K., Schneider, P., Kazadzis, S., Barreto, Á., Gardiner, T., Mottungan, K., Medland, D., and Coleman, M.: Spectral aerosol optical depth from SI-traceable spectral solar irradiance measurements, *Atmos. Meas. Tech*., 16, 4667–4680, https://doi.org/10.5194/amt-16-4667-2023, 2023.
31. Hansen, J. E., Travis, L. D.: Light scattering in planetary atmospheres, *Space Sci. Rev*., 16, 527–610, https://doi.org/10.1007/BF00168069, 1974.
32. Harrison, L., Joseph M.: Objective algorithms for the retrieval of optical depths from ground-based measurements. *Appl. Opt.* 33, 5126-5132, https://doi.org/10.1364/AO.33.005126, 1994.
33. Hess, M., Koepke, P., and Schult, I.: Optical properties of aerosols and clouds: The software package OPAC, *B. Am. Meteorol. Soc*., 79, 831–844, https://doi.org/10.1175/1520-0477(1998)079<0831:OPOAAC>2.0.CO;2, 1998.
34. Holben, B. N., Tanré, D., Smirnov, A., Eck, T. F., Slutsker, I.,Abuhassan, N., Newcomb, W. W., Schafer, J. S., Chatenet, B., Lavenu, F., Kaufman, Y. J., Vande Castle, J., Setzer, A., Markham, B., Clark, D., Frouin, R., Halthore, R., Karneli, A., O'neill, N. T., Pietras, C., Pinker, C., Voss, K., and Zibordi, G.: An emerging ground-based aerosol climatology: Aerosol optical depth from AERONET, *J. Geophys. Res.-Atmos*., 106, 12067– 12097, https://doi.org/10.1029/2001JD900014, 2001 (data available at: https://aeronet.gsfc.nasa.gov/cgi-bin/data_display_aod_v3?site=Izana&nachal=2&level=3&place_code=10, last access: 14 November 2019).
35. Hrabčák, P.: Comparison of the optical depth of total ozone and atmospheric aerosols in Poprad-Gánovce, Slovakia, Atmos. Chem. Phys., 18, 7739–7755, https://doi.org/10.5194/acp-18-7739-2018, 2018.
36. Hrabčák, P.: 30 years of total ozone and AOD measurements using the Brewer spectrophotometer in Poprad-Gánovce, Slovakia; The Quadrennial Ozone Symposium, 15–19 July 2024, University of Colorado, Boulder, Colorado, USA, available online, 2024.
37. IPCC 2023, CLIMATE CHANGE 2023 Synthesis Report: Summary for Policymaker, Intergovernmental Panel on Climate Change, 2023. https://www.ipcc.ch/report/ar6/syr/downloads/report/IPCC_AR6_SYR_SPM.pdf (last accessed: 05 November 2024)

38. Irie, H., Hoque, H. M. S., Damiani, A., Okamoto, H., Fatmi, A. M., Khatri, P., Takamura, T., Jarupongsakul, T.: Simultaneous observations by sky radiometer and MAX-DOAS for characterization of biomass burning plumes in central Thailand in January–April 2016, *Atmos. Meas. Tech*., 12, 599–606, https://doi.org/10.5194/amt-12-599-2019, 2019.
39. Ivănescu, L., Baibakov, K., O'Neill, N. T., Blanchet, J.-P., Schulz, K.-H.: Accuracy in Starphotometry. *Atmos. Meas. Tech*. 14 (10): 6561–99. https://doi.org/10.5194/amt-14-6561-2021, 2021.
40. Jain, P., Barber, Q.E., Taylor, S.W. et al. Drivers and Impacts of the Record-Breaking 2023 Wildfire Season in Canada. *Nat Commun* 15, 6764. https://doi.org/10.1038/s41467-024-51154-7, 2024.
41. Kaufman, Y. J., Gobbi, G. P., and Koren, I.: Aerosol climatology using a tunable spectral variability, cloud screening of AERONET data, *Geophys. Res. Lett*., 33, L07817, https://doi.org/10.1029/2005GL025478, 2006.
42. Kazadzis, S., Bais, A., Kouremeti, N., Gerasopoulos, E., Garane, K., Blumthaler, M., Schallhart, B., Cede, A.: Direct spectral measurements with a Brewer spectroradiometer: absolute calibration and aerosol optical depth retrieval, *Applied Optics*, 44 (9), 1681-1690, https://doi.org/10.1364/AO.44.001681, 2005.
43. Kazadzis., S., Bais, A., Amiridis, V., Balis, D., Meleti, C., Kouremeti, N., Zerefos, C. S., Rapsomanikis, S., Petrakakis, M., Kelesis, A., Tzoumaka, P., Kelektsoglou, K.: Nine years of UV aerosol optical depth measurements at Thessaloniki, Greece, *Atmospheric Chemistry and Physic*s, 7, 2091-2101, https://doi.org/10.5194/acp-7-2091-2007, 2007.
44. Kazadzis, S., Raptis, P., Kouremeti, N., Amiridis, V., Arola, A., Gerasopoulos, E., and Schuster, G. L.: Aerosol absorption retrieval at ultraviolet wavelengths in a complex environment, *Atmos. Meas. Tech*., 9, 5997–6011, https://doi.org/10.5194/amt-9-5997-2016, 2016.
45. Kazadzis, S., Kouremeti, N., Gröbner, J.: Fourth WMO Filter Radiometer Comparison (FRC-IV), GAW Report No. 231. https://library.wmo.int/records/item/55417-fourth-wmo-filter-radiometer-comparison-frc-iv?offset=1, 2016.
46. Kazadzis, S., Kouremeti, N., Nyeki, S., Gröbner, J., and Wehrli, C.: The World Optical Depth Research and Calibration Center (WORCC) quality assurance and quality control of GAW-PFR AOD measurements, *Geosci. Instrum. Method. Data Syst*., 7, 39–53, https://doi.org/10.5194/gi-7-39-2018, 2018a.
47. Kazadzis, S., Kouremeti, N., Diémoz, H., Gröbner, J., Forgan, B. W., Campanelli, M., Estellés, V., Lantz, K., Michalsky, J., Carlund, T., Cuevas, E., Toledano, C., Becker, R., Nyeki, S., Kosmopoulos, P. G., Tatsiankou, V., Vuilleumier, L., Denn, F. M., Ohkawara, N., Ijima, O., Goloub, P., Raptis, P. I., Milner, M., Behrens, K., Barreto, A., Martucci, G., Hall, E., Wendell, J., Fabbri, B. E., and Wehrli, C.: Results from the Fourth WMO Filter Radiometer

Comparison for aerosol optical depth measurements, *Atmos. Chem. Phys*., 18, 3185–3201, https://doi.org/10.5194/acp-18-3185-2018, 2018b.

48. Kazadzis, S. and Barreto, Á.: Spectral Aerosol Optical Depth from Traceable Spectral Solar Irradiance Measurements to the SI., *Atmos. Meas. Tech*., 16, 4667–4680, https://doi.org/10.5194/amt-16-4667-2023, 2023.
49. Kazadzis, S., Kouremeti, N., and Gröbner, J.: Fifth WMO Filter Radiometer Comparison (FRC-V) 27 September to 25 October 2021, Davos, Switzerland, WMO, GAW report 280, https://library.wmo.int/records/item/66263-fifth-wmo-filter-radiometer-comparison-frc-v?offset=5, 2023.
50. Khatri, P. and Takamura, T.: An algorithm to screen cloud-affected data for sky radiometer data anlaysis*, J. Meteorol Soc. Jpn*., 87, 189–204, 2009.
51. Kieffer, H. H. and Stone, T. C.: The spectral irradiance of the moon, *The Astron. J.,* 129, 2887–2901, https://doi.org/10.1086/430185, 2005.
52. Kouremeti, N., Gröbner, J., & Nevas, S.: Stray-Light Correction Methodology for the Precision Solar Spectroradiometer. *Journal of Physics: Conference Series*, 2149, 012002. https://iopscience.iop.org/article/10.1088/1742-6596/2149/1/012002, 2022.
53. López-Solano, J., Redondas, A., Carlund, T., Rodriguez-Franco, J. J., Diémoz, H., León-Luis, S. F., Hernández-Cruz, B., Guirado-Fuentes, C., Kouremeti, N., Gröbner, J., Kazadzis, S., Carreño, V., Berjón, A., Santana-Díaz, D., Rodríguez-Valido, M., De Bock, V., Moreta, J. R., Rimmer, J., Smedley, A. R. D., Boulkelia, L., Jepsen, N., Eriksen, P., Bais, A. F., Shirotov, V., Vilaplana, J. M., Wilson, K. M., Karppinen, T.: Aerosol optical depth in the European Brewer Network. *Atmospheric Chemistry and Physics*, 18(6), 3885-3902, https://doi.org/10.5194/acp-18-3885-2018, 2018.
54. Lorenz, S., F. Heinzl, S. Bauer, M. Janßen, V. De Bock, A. Mangold, P. Scholz-Kreisel, D. Weiskopf, Increasing Solar UV Radiation in Dortmund, Germany – Data and Trend Analyses and Comparison to Uccle, Belgium, submitted to Photochemical & Photobiological Sciences, Accepted for publication. https://iupb-mepsa-2024.m.asnevents.com.au/schedule/session/23372/abstract/104789 (last accessed: 07 November 2024)
55. MacCarthy, J., Tyukavina, A., Weisse, MJ., Harris, N., & Glen, E.. Extreme wildfires in Canada and their contribution to global loss in tree cover and carbon emissions in 2023. *Global Change Biology*, 30, e17392. https://doi.org/10.1111/gcb.17392, 2024.
56. Masoom, A., Kouremeti, N., Kazadzis, S., Killian, M., Kreuter, A., and Raptis, I.-P.: Performance analysis and synergistic use of cloud flagging algorithms of ground-based remote sensing instrumentations, *EMS Annual Meeting 2024*, Barcelona, Spain, 1–6 Sep 2024, EMS2024-365, https://doi.org/10.5194/ems2024-365, 2024a.

57. Masoom, A., Kazadzis, S., Valeri, M., Raptis, I.-P., Brizzi, G., Papachristopoulou, K., Barnaba, F., Casadio, S., Kreuter, A., and Niro, F.: Assessment of the impact of NO_2 contribution on aerosol-optical-depth measurements at several sites worldwide, *Atmos. Meas. Tech.*, 17, 5525–5549, https://doi.org/10.5194/amt-17-5525-2024, 2024b.
58. Mayer, B. and Kylling, A.: Technical note: The libRadtran soft- ware package for radiative transfer calculations - description and examples of use, *Atmos. Chem. Phys.*, 5, 1855–1877, https://doi.org/10.5194/acp-5-1855-2005, 2005.
59. Mayer, B.: Radiative transfer in the cloudy atmosphere, in: *EPJ Web of Conferences*, vol. 1, 75–99, EDP Sciences, https://doi.org/10.1140/epjconf/e2009-00912-1, 2009.
60. Meleti, C., and F. Cappellani: Measurements of aerosol optical depth at Ispra: Analysis of the correlation with UV-B, UV-A, and total solar irradiance, *J. Geophys. Res.*, 105(D4), 4971–4978, https://doi.org/10.1029/1999JD900459, 2000.
61. Meleti C., Bais A.F., Kazadzis S., Kouremeti N., Garane K., Zerefos C.: Factors affecting solar UV irradiance, measured since 1990 at Thessaloniki, Greece, *Int. Journal of Remote Sensing*, 30:15, 4167, 4179, https://doi.org/10.1080/01431160902822864, 2009.
62. Nakajima, T., Campanelli, M., Che, H., Estellés, V., Irie, H., Kim, S.-W., Kim, J., Liu, D., Nishizawa, T., Pandithurai, G., Soni, V. K., Thana, B., Tugjsurn, N.-U., Aoki, K., Go, S., Hashimoto, M., Higurashi, A., Kazadzis, S., Khatri, P., Kouremeti, N., Kudo, R., Marenco, F., Momoi, M., Ningombam, S. S., Ryder, C. L., Uchiyama, A., and Yamazaki, A.: An overview of and issues with sky radiometer technology and SKYNET, *Atmos. Meas. Tech*., 13, 4195–4218, https://doi.org/10.5194/amt-13-4195-2020, 2020.
63. Neumann, A. and Witzke, A.: The influence of sunshape on the DLR solar furnace beam, *Sol. Energ*., 66, 447–457, https://doi.org/10.1016/S0038-092X(99)00048-1, 1999.
64. O'Neill, N. T., Baibakov, K., Hesaraki, S., Ivănescu, L., Martin, R. V., Perro, C., Chaubey, J. P., Herber, A. B., Duck, T. J.: Temporal and Spectral Cloud Screening of Polar Winter Aerosol Optical Depth (AOD): Impact of Homogeneous and Inhomogeneous Clouds and Crystal Layers on Climatological-Scale AODs. *Atmospheric Chemistry and Physics* 16 (19): 12753–65. https://doi.org/10.5194/acp-16-12753-2016, 2016.
65. O'Neill, N. T., Eck, T. F., Smirnov, A. V., Holben, B. N., Thulasiraman, S.: Spectral Discrimination of Coarse and Fine Mode Optical Depth. *Journal of Geophysical Research* 108 (D17): 4559. https://doi.org/10.1029/2002JD002975, 2003
66. Oehlschlägel, Lisa: Analyse und Interpretation der spektralen Strahlung an den Messstationen Berlin und Lindenberg, *Master Thesis of Technical University Dresden*, 2019
67. Pastiels, R.: Contribution à l'étude du problème des méthodes actinométriques, Publ. A11, Institut Royal Météorologique de Belgique, Uccle, Belgium, 1959. https://search.arch.be/en/?option=com_rab_findingaids&view=findingaid&format=pdf&eadid=BE-A0510_722900_806473_FRE, (last accessed: 21 October 2024).

68. Pavanello, D., Galleano, R., Zaaiman, W., Ankit, M., Kouremeti, N., Gröbner, J., K. Hoogendijk, M. Po, E.F. Lisbona, W. Alius, D. Dosenovicova, I. Kroeger, D. Friedrich, E. Haverkamp, A. Minuto, E. Celi, M. Pravettoni, G. Bellenda, R. Fucci.: Results of the IX International Spectroradiometer Intercomparison and impact on precise measurements of new photovoltaic technologies. *Progress in Photovoltaics: Research and Applications*, 29(1), 109-123. https://onlinelibrary.wiley.com/doi/abs/10.1002/pip.3347, 2021.
69. Pérez-Ramírez, Daniel, H. Lyamani, F. J. Olmo, D. N. Whiteman, F. Navas-Guzmán, and L. Alados-Arboledas: Cloud Screening and Quality Control Algorithm for Star Photometer Data: Assessment with Lidar Measurements and with All-Sky Images. *Atmospheric Measurement Techniques* 5 (7): 1585–99. https://doi.org/10.5194/amt-5-1585-2012, 2012
70. Pó, M., Hoogendijk, K., Beuttell, W., Kazunori, S., and Takeuchi, E.: Direct Spectral Irradiance Measurements from Rotating Shadowband EKO Grating Spectroradiometer, in: 2018 *IEEE 7th World Conference on Photovoltaic Energy Conversion* (WCPEC) (A Joint Conference of 45th IEEE PVSC, 28th PVSEC & 34th EU PVSEC), 2337–2340, IEEE, https://doi.org/10.1109/PVSC.2018.8547445, 2018.
71. Räisänen, P. and Lindfors, A. V.: On the Computation of Apparent Direct Solar Radiation, *J. Atmos. Sci.*, 76, 2761–2780, https://doi.org/10.1175/JAS-D-19-0030.1, 2019.
72. Riihimaki et al. (2019): Radiative Flux Analysis (RADFLUXANAL) Value-Added Product: Retrieval of Clear-Sky Broadband Radiative Fluxes and Other Derived Values (No. DOE/SC-ARM-TR-228, 1569477), https://doi.org/10.2172/1569477, (last accessed: 21 October 2024).
73. Rimmer, J. S., Redondas, A., & Karppinen, T. (2018). EuBrewNet–A European brewer network (COST Action ES1207), an overview. *Atmospheric Chemistry and Physics*, 18(14), 10347-10353. https://doi.org/10.5194/acp-18-10347-2018, 2018.
74. Román, R., González, R., Toledano, C., Barreto, Á., Pérez-Ramírez, D., Benavent-Oltra, J. A., Olmo, F. J., Cachorro, V. E., Alados-Arboledas, L., de Frutos, Á. M.: Correction of a lunar-irradiance model for aerosol optical depth retrieval and comparison with a star photometer, *Atmos. Meas. Tech*., 13, 6293–6310, https://doi.org/10.5194/amt-13-6293-2020, 2020.
75. Russo, P., Laguarda, A., Abal, G., and Doppler, L.: Aerosol optical depth from spectral direct normal irradiance measurements in Montevideo, Uruguay, Int. Arch. Photogramm. *Remote Sens*. Spatial Inf. Sci., XLVIII-M-1-2023, 565–572, https://doi.org/10.5194/isprs-archives-XLVIII-M-1-2023-565-2023, 2023.
76. Savastiouk, V., Procedure of observations of the total ozone content, aerosol optical depth and the effective temperature of the ozone layer at the network of stations equipped with the Brewer spectrophotometers, in Atmospheric Ozone, Proceedings of

the Conference of Young Researchers, Moscow, Russian Academy of Sciences, p. 5-11, 1995.

77. Savastiouk, V., On the real-time measurements of the aerosol optical depth in UV with the Brewer spectrophotometers, a report for Meteorological Service of Canada, 2004
78. Savastiouk, V., C.T. McElroy, The ozone and molecular air mass factor calculations for the ground base spectrophotometers, Proceedings of the Quadrennial Ozone Symposium, Ed. C. Zerefos, 498-499, 2004. (2004 a) https://www.researchgate.net/profile/Vladimir-Savastiouk/publication/265595692_Calculating_air_mass_factors_for_Ozone_and_Rayleigh_air_mass_factor_calculations_for_ground-based_spectrophotometers/links/5413a0400cf2788c4b359b13/Calculating-air-mass-factors-for-Ozone-and-Rayleigh-air-mass-factor-calculations-for-ground-based-spectrophotometers.pdf, last accessed: October 21, 2024.
79. Savastiouk, V., C.T. McElroy, An algorithm for real-time calculations of the aerosol optical depth with the Brewer Spectrophotometer, Proceedings of the Quadrennial Ozone Symposium, Ed. C. Zerefos, 500-501, 2004 (2004 b). https://www.researchgate.net/publication/265595693_An_algorithm_for_real-time_calculations_of_the_aerosol_optical_depth_with_the?channel=doi&linkId=5413a0c50cf2bb7347db25eb&showFulltext=true, last accessed: October 21, 2024.
80. Savastiouk, V., C.T. McElroy, Brewer Spectrophotometer Total Ozone Measurements Made During the 1998 Middle Atmospheric Nitrogen Trend Assessment (MANTRA) Campaign, Atmos-Ocean, 43 (4), 315–324, 2005, https://doi.org/10.3137/ao.430403
81. Savastiouk, V.: Improvements to the direct-sun ozone observations taken with the Brewer spectrophotometer, PhD Thesis, York University, Canada, https://www.researchgate.net/publication/326066052_Improvements_to_the_direct-sun_ozone_observations_taken_with_the_Brewer_spectrophotometer (last access: 11 October 2024), 2006.
82. Schenzinger, V. and Kreuter, A.: Reducing cloud contamination in aerosol optical depth (AOD) measurements, *Atmos. Meas. Tech*., 14, 2787–2798, https://doi.org/10.5194/amt-14-2787-2021, 2021.
83. Schenzinger, V., Kazadzis, S., Kouremeti, N., Masoom, A., COST short term scientific mission report, 2023. https://harmonia-cost.eu/wp-content/uploads/2023/06/STSM-report-Verena-Schenzinger.pdf (last accessed: October 07, 2024).
84. Sengupta, M., Habte, A. M., Xie, Y., Lopez, A. J., Dooraghi, M., Kutchenreiter, M. C., Andreas, A. M., Reda, I. M., Maclaurin, G. J., Foster, M. J., and Gueymard, C.: Solar Resource Calibra- tion, Measurement, and Dissemination: Final Report FY 2016- FY 2018, Tech. rep., National Renewable Energy Lab. (NREL), Golden, CO, USA, https://doi.org/10.2172/1513198, 2019. (last accessed: 21 October 2024)

85. Serdyuchenko, A., Gorshelev, V., Weber, M., Chehade, W., and Burrows, J. P.: High spectral resolution ozone absorption cross-sections – Part 2: Temperature dependence, *Atmos. Meas. Tech.*, 7, 625–636, https://doi.org/10.5194/amt-7-625-2014, 2014
86. Shaw, G. E., Reagan, J. A., and Herman, B. M.: Investigations of atmospheric extinction using direct solar radiation measurements made with a multiple wavelength radiometer, *J. Appl. Meteorol.*, 12, 374–380, https://doi.org/10.1175/1520-0450(1973)012<0374:IOAEUD>2.0.CO;2, 1973.
87. Sinyuk, A., Holben, B. N., Smirnov, A. V., Eck, T. F., Slutsker, I., Schafer, J. S., Giles, D. M., Sorokin M.: Assessment of Error in Aerosol Optical Depth Measured by AERONET Due to Aerosol Forward Scattering. *Geophysical Research Letters* 39 (23). https://doi.org/10.1029/2012GL053894, 2012.
88. Smirnov, A.; Holben, B.; Eck, T.; Dubovik, O.; Slutsker, I. Cloud-screening and quality control algorithms for the AERONET database. *Remote sensing of environment*, 73, 337–349. https://doi.org/10.1016/S0034-4257(00)00109-7, 2000.
89. Smirnov, A. V., Zhuravleva, T. B., Segal-Rosenheimer, M., Holben, B. N.: Limitations of AERONET SDA Product in Presence of Cirrus Clouds. *Journal of Quantitative Spectroscopy and Radiative Transfer* 206 (February): 338–41. https://doi.org/10.1016/J.JQSRT.2017.12.007, 2018.
90. Song, H. J., Sohn, B. J., Chun, H. W., Chun, Y., and Lee, S. S.: Improved cloud screening method for the analysis of sky radiometer measurements and application to Asian dust detection, *J. Meteorol. Soc. Jpn.*, 92A, 167–183, 2014.
91. Thuillier, G., Hersé, M., Labs, D. et al.: The Solar Spectral Irradiance from 200 to 2400 nm as Measured by the SOLSPEC Spectrometer from the Atlas and Eureca Missions. *Solar Physics* 214, 1–22. https://doi.org/10.1023/A:1024048429145, 2003.
92. Toledano, C., González, R., Fuertes, D., Cuevas, E., Eck, T. F., Kazadzis, S., Kouremeti, N., Gröbner, J., Goloub, P., Blarel, L., Román, R., Barreto, Á., Berjón, A., Holben, B. N., and Cachorro, V. E.: Assessment of Sun photometer Langley calibration at the high-elevation sites Mauna Loa and Izaña, *Atmos. Chem. Phys.*, 18, 14555–14567, https://doi.org/10.5194/acp-18-14555-2018, 2018.
93. Wang, Z., Wang, Z., Zou, Z. et al. Severe Global Environmental Issues Caused by Canada's Record-Breaking Wildfires in 2023. *Adv. Atmos. Sci.* 41, 565–571. https://doi.org/10.1007/s00376-023-3241-0, 2024.
94. WMO/GAW (2004). Experts workshop on a global surface-based network for long term observations of column aerosol optical properties. Technical Report 162, WMO/GAW.
95. WMO: Fourth WMO Workshop on the Impact of Various Observing Systems on Numerical Weather Prediction WMO/TD No. 1450, World Weather Watch, available

at: https://www.wmo.int/pages/prog/www/OSY/Meetings/NWP-4-Geneva2008/Abridged_Version.pdf (last access: 14 November 2019), 2008.

96. Wuttke, S., Kreuter, A., and Blumthaler, M.: Aerosol climatology in an Alpine valley, *J. Geophys. Res.-Atmos.*, 117, D20202, https://doi.org/10.1029/2012JD017854, 2012.
97. Yoon, H. W., Sperfeld, P., Yousef, S. G., and Metzdorf, J.: NIST- PTB measurements of the radiometric temperatures of a high- temperature black body using filter radiometers, *Metrologia*, 37, 377, https://doi.org/10.1088/0026-1394/37/5/7, 2000.
98. Zuber, R., Sperfeld, P., Riechelmann, S., Nevas, S., Sildoja, M., and Seckmeyer, G.: Adaption of an array spectroradiometer for total ozone column retrieval using direct solar irradiance measurements in the UV spectral range, *Atmos. Meas. Tech.*, 11, 2477–2484, https://doi.org/10.5194/amt-11-2477-2018, 2018.
99. Zuber, R., Köhler, U., Egli, L., Ribnitzky, M., Steinbrecht, W., and Gröbner, J.: Total ozone column intercomparison of Brewers, Dobsons, and BTS-Solar at Hohenpeißenberg and Davos in 2019/2020, *Atmos. Meas. Tech.*, 14, 4915–4928, https://doi.org/10.5194/amt-14-4915-2021, 2021.

List of Figures

List of Tables

APPENDIX: Tables and Figures

Appendix Table T1: Acronyms description

AE	Ångström Exponents (α, β): characterize AOD spectral variation
AEMET	Agencia Estatal de Meteorología (Spain meteorological service)
AERONET	AErosol RObotic NETwork: AOD and aerosol properties measurements network using Cimel CE-318 photometer
AOD	Aerosol Optical Depth (also known as AOT: Aerosol Optical Thickness): Main parameter used to characterize aerosol amount and aerosol impact on radiation in the atmosphere. AOD is also the main parameter measured with photometers.
AWI	Alfred-Wegener-Institut (German Polar Institute)
AWIPEV	AWI and IPEV joint station at Ny-Ålesund, Spitsbergen (Svalbard)
BTS	BiTec Sensor Spektralradiometer: Array spectroradiometer manufactured by GHO
CNR	Consiglio Nazionale delle Ricerche (Italian national research council)
COBALD	Compact Optical Backscatter AerosoL Detector: Radiosounding (balloon carried) sensor for measuring in-situ the aerosol extinction profile.
DWD	Deutscher Wetterdienst (German meteorological service)
EUBREWNET	European Brewer Network
GAW	Global Atmosphere Watch: WMO Programm of trends monitoring of the atmosphere
GAW-PFR	Global Atmosphere Watch - Precision Filter Radiometer network: AOD measurement network of WMO/GAW Programm
GHO	Gigahertz-Optik, instrument manufacturer based in Türkenfeld, Germany
GOA	Grupo de Óptica Atmosférica, UVa (Valladolid, Spain)
HARMONIA	International network for harmonisation of atmospheric aerosol retrievals from ground-based photometers: Name of the COST action
IOS	International Ozone Service Inc., Brewer expert company based in Toronto, CA: https://www.io3.ca/
IPCC	Intergovernmental Panel on Climate Change
ITC	Inclusive Target Countries: Category of countries of COSt association
LIDAR	LIght Detection And Ranging

MOL-RAO	Meteorological Observatory Lindenberg - Richard Aßmann Observatory: DWD observatory of Lindenberg (Tauche, Germany)
PFR	Precision FilterRadiometer: Photometer manufactured by PMOD/WRC
PMOD/WRC	Physikalisch-Meteorologisches Observatorium Davos / World Radiation Center
POM	Precise design Of Meteorological and scientific instrument: Photometer manufactured by Prede and used in the network SKYNET.
PSR	Precision Solar SpectroRadiometer: Spectroradiometer manufactured by PMOD/WRC
RIMO	ROLO Implementation for Moon photometry Observation: open lunar reflectance model developed by GOA and AEMET/IARC
RMSE	Root Mean Square Error
ROLO	Robotic Lunar Observatory: lunar reflectance model of USGS
SCILLA	Summer Campaign for Intercomparison of Lunar measurements of Lindenberg's Aerosol: Campaign at DWD/MOL-RAO in Lindenberg (Tauche, Germany), August/September 2020
SHMÚ	Slovenský hydrometeorologický ústav (Slovak Hydrometeorological Institute)
SKYNET	SKY Measurements NETwork: AOD and aerosol properties measurements network using Prede-POM instrument
SSA	Single Scattering Albedo
STSM	Short Term Scientific Mission: Grant possibility of a COST Action (including a visit to another institute)
ToA	top of the atmosphere
TOC	Total Ozone Column: Columnar integrated amount of Ozone in DU (Dobson Unit)
UVa	University of Valladolid, Valladolid, Spain
WG	Working Group
WMO	World Meteorological Organisation

Appendix Table T2: Description of abbreviations used in Fig. 3.13

S. No.	Station Code	Station location
1	ALD	Aldine, USA
2	ATH	Athens, Greece
3	ATL	Atlanta, USA
4	BEI	Beijing, China
5	BRW	Brunswick, USA
6	BRU	Brussels, Belgium
7	DHK	Dhaka, Bangladesh
8	EGB	Egbert, Canada
9	GRN	Granada, Spain
10	HAM	Hampton, USA
11	HEL	Helsinki, Finland
12	HOU	Houston, USA
13	JYC	Jülich/Joyce, Germany
14	LPT	La Porte, USA
15	MNH	Manhattan, USA
16	MXC	Mexico City, Mexico
17	NHV	New Haven, USA
18	ROM	Rome, Italy
19	SPR	Sapporo, Japan
20	SOL	Seoul, South Korea
21	TEL	Tel Aviv, Israel
22	TOR	Toronto, Canada
23	TSU	Tsukuba, Japan

24	ULS	Ulsan, South Korea
25	BOU	Boulder, USA
26	COM	Comodoro, Argentina
27	DLG	Dalanzadgad, Mongolia
28	DAV	Davos, Switzerland
29	INN	Innsbruck, Austria
30	IZA	Izaña, Spain
31	LDB	Lindenberg, Germany
32	NYA	Ny-Ålesund, Norway
33	WAL	Wallops, USA

APPENDIX Figure of Section 3:

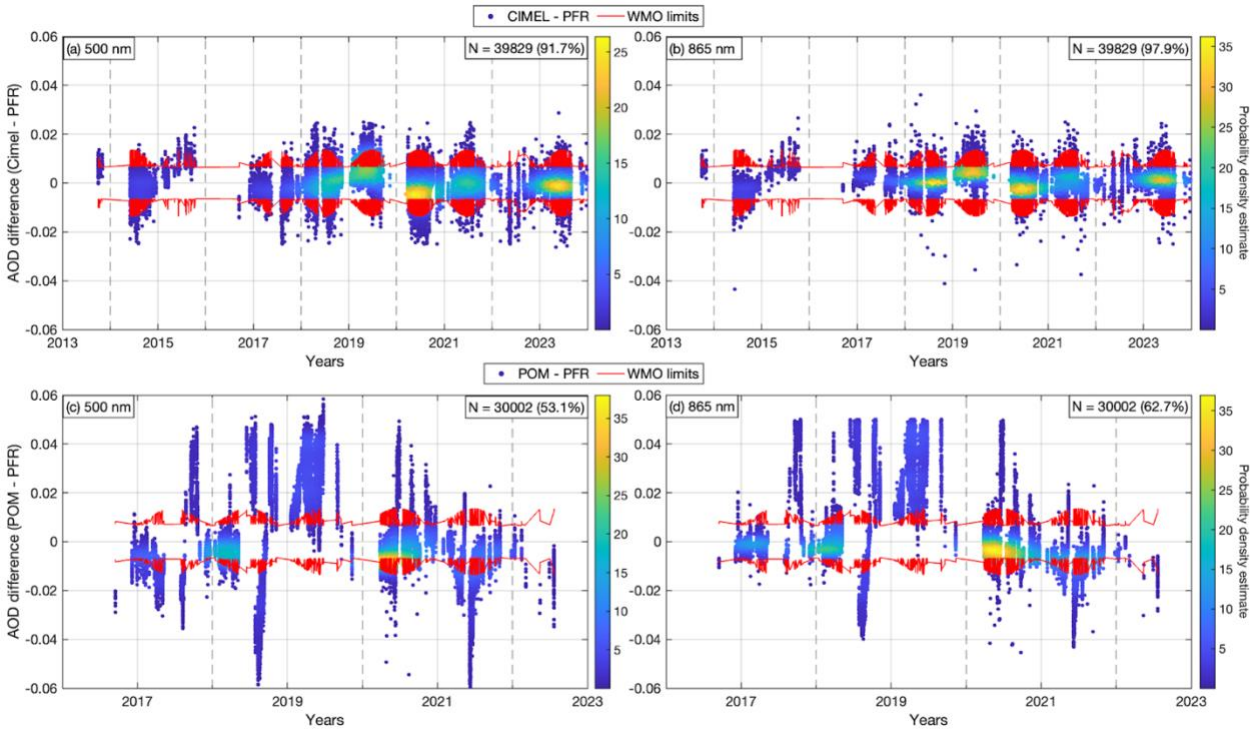

Figure AP-3.1: Time series of AOD differences for (AERONET – GAW-PFR) and (SKYNET – GAW-PFR) at (a, c) 500 nm and (b, d) 865 nm, respectively from Study K on Lindenberg-Dataset. N represents the total number points and in the parenthesis is the percentage of points within the WMO limits.

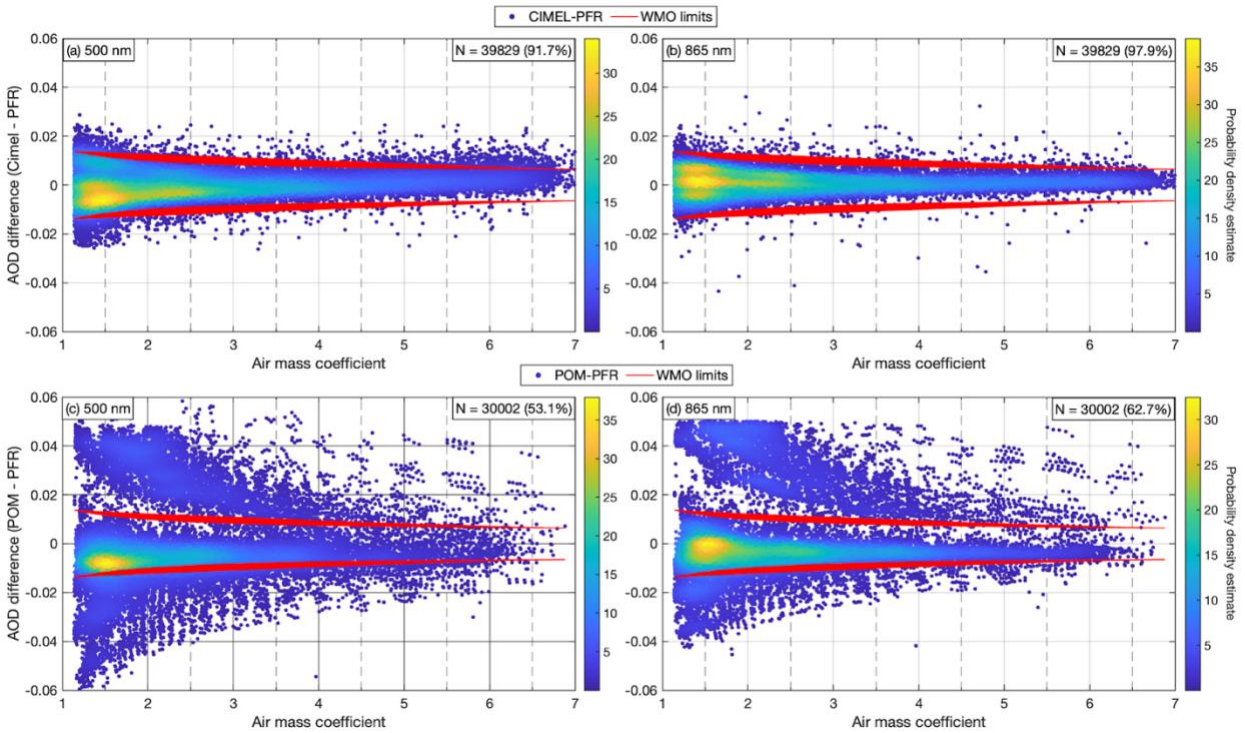

Figure AP-3.2: AOD differences for (AERONET – GAW-PFR) and (SKYNET – GAW-PFR) as a function of airmass at (a, c) 500 nm and (b, d) 865 nm, respectively from Study K on Lindenberg-Dataset. N represents the total number points and in the parenthesis is the percentage of points within the WMO limits.

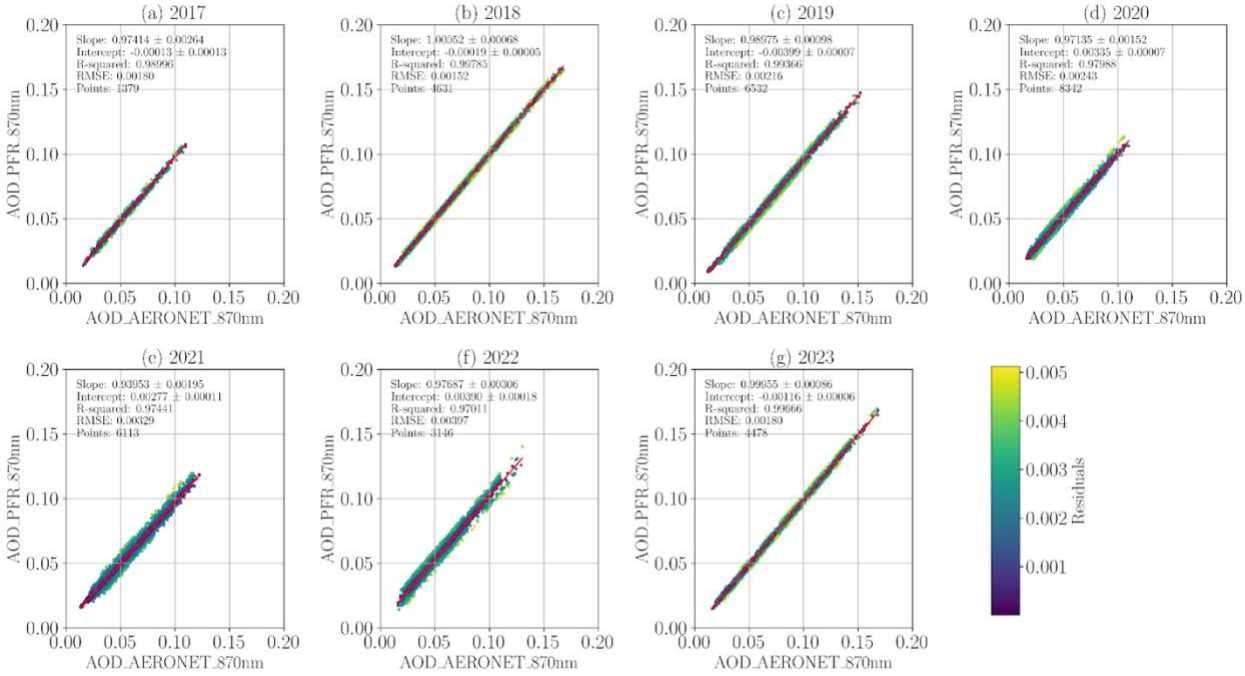

Figure AP-3.3: (a-g) Yearly linear fit of PFR AOD vs AERONET Cimel AOD by Year for the 865 nm channels from study G from 2017-2023.

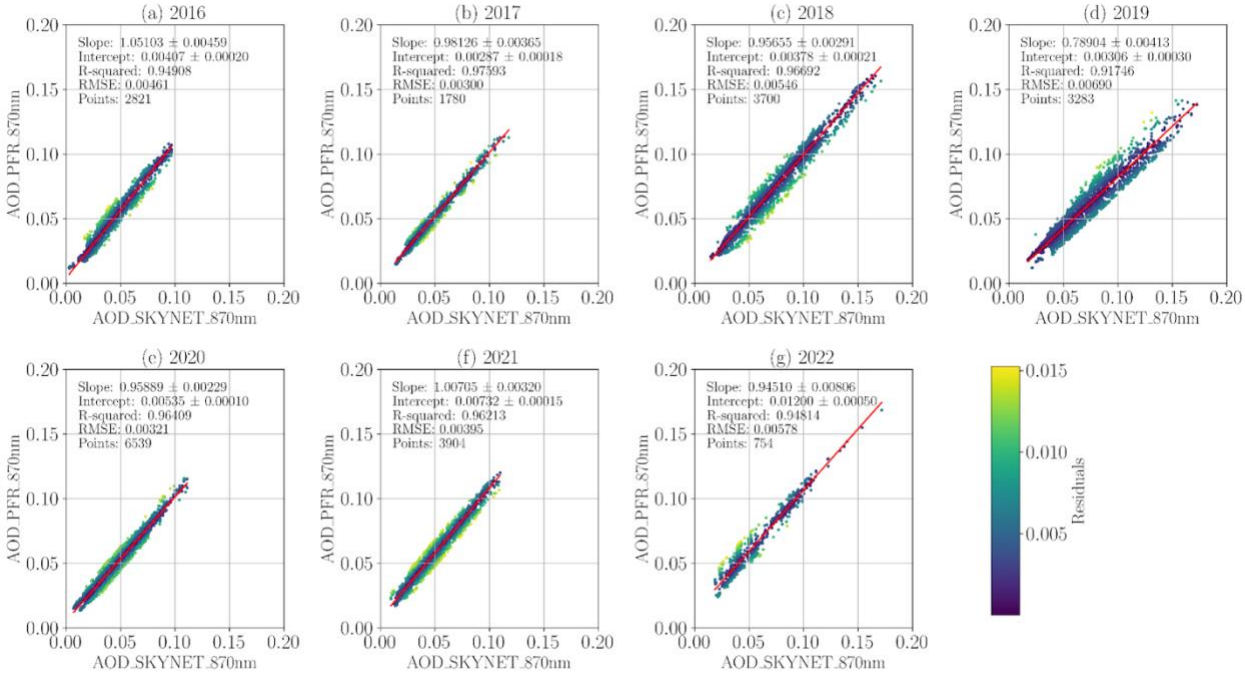

Figure AP-3.4: (a-g) Yearly linear fit of PFR AOD vs SKYNET Prede AOD by Year for the 870 nm channels from study G from 2016-2022.

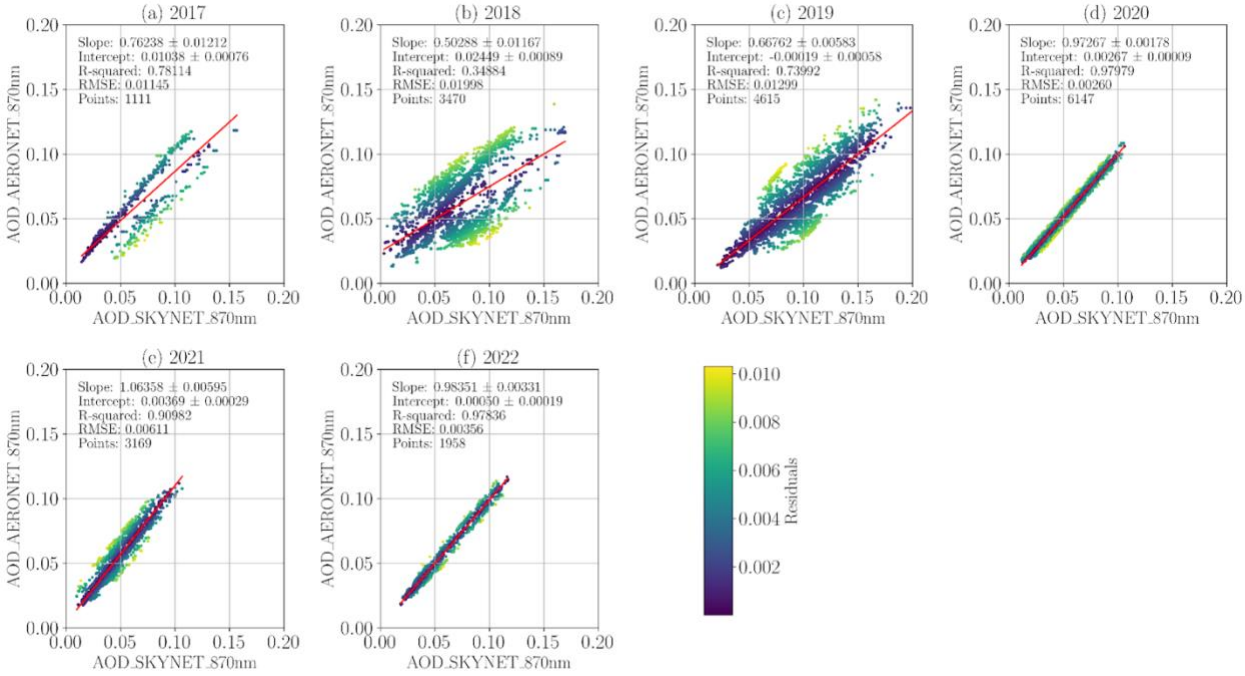

Figure AP-3.5: (a-f) Yearly linear fit of AERONET Cimel AOD vs SKYNET Prede AOD by Year for the 865 nm channel from study G from 2017-2023.